TỰ ĐỘNG HÓA NGÀY NAY
AUTOMATION TODAY
HỘI TỰ ĐỘNG HÓA VIỆT NAM
ISSN 1859-0551

ĐO LƯỜNG, ĐIỀU KHIỂN VÀ TỰ ĐỘNG HÓA

SPECIAL ISSUE ON MEASUREMENT, CONTROL AND AUTOMATION

QUYỂN 28 SỐ 1 | THÁNG 4 2024

HỘI NGHỊ VÀ TRIỂN LÃM QUỐC TẾ LẦN THỨ 7 VỀ ĐIỀU KHIỂN VÀ TỰ ĐỘNG HOÁ

The 7th Vietnam International Conference and Exhibition on Control and Automation

10-11/5/2024 Tp. Hải Phòng

VCCA2024

CALL FOR PAPERS

http://www.vcca.engineer/vcca2024/vi/

Hội Tự động hóa Việt Nam định kỳ 2 năm một lần tổ chức *Hội nghị - Triển lãm quốc tế về Điều khiển và Tự động hóa* với tên tiếng Anh là *Vietnam International Conference and Exhibition on Control and Automation (VCCA)* nhằm thúc đẩy phát triển Điều khiển học và Công nghệ Tự động hóa phục vụ cho sự nghiệp xây dựng và phát triển đất nước. **VCCA-2024** là Hội nghị VCCA lần thứ 7 được Hội Tự động hóa Việt Nam tổ chức, Trường Đại học Hàng hải Việt Nam là đơn vị đăng cai, thời gian dự kiến trong hai ngày 10-11/5/2024 tại Hải Phòng.

VCCA - 2024 gồm 2 phần: Hội nghị khoa học và Triển lãm quốc tế & Diễn đàn doanh nghiệp

Tiêu chí Hội nghị:

Tự động hoá và Chuyển đổi số thúc đẩy phát triển kinh tế xanh

Các chủ đề chính của Hội nghị:

1. Tự động hóa: Cảm biến và cơ cấu chấp hành, I/O thông minh; Hệ thống tự động hóa tích hợp toàn diện; Các hệ SCADA/HMI, DCS, CAD/CAM/CIM/CNC; Hệ thống nhúng, công nghệ PLC, PXI, IPC; Mô hình hóa và mô phỏng quá trình sản xuất; Điều khiển quá trình công nghệ; Tự động hóa phòng thí nghiệm; Hệ thống đo lường thông minh; Mạng đo và điều khiển; Phần mềm tự động hóa; Vi xử lý, SOC, DSP, FPGA, ASIC trong điều khiển; Điện tử công suất; Internet of things; Big data; Sensor networks; Trí tuệ nhân tạo.

2. Điều khiển học: Lý thuyết hệ thống; Lý thuyết điều khiển; Hệ phi tuyến; Các hệ rời rạc, hệ lai; Mô hình hoá và mô phỏng; Điều khiển tối ưu; Nhận dạng hệ thống; Lọc và ước lượng trạng thái; Điều khiển thích nghi và các hệ học; Điều khiển bền vững; Điều khiển thông minh, hệ mờ, hệ chuyên gia, mạng nơ ron, thuật toán gien; Điều khiển chuyển động; Điều khiển điện tử công suất; Mô hình hóa và điều khiển rô bốt công nghiệp; Điều khiển xe tự hành, rô bốt di động; Điều khiển các hệ sinh học; Điều khiển trên cơ sở thông tin hình ảnh; Điều khiển trên cơ sở ngôn ngữ tự nhiên, tư thế và hành vi; Các hệ điều khiển kích cỡ micro và nano; Điều khiển các loại máy điện, truyền động và hệ thống năng lượng.

3. Ứng dụng: Các giải pháp chuyển đổi số: Chính quyền số, kinh tế số và xã hội số; Thành phố thông minh; Hệ thống điều khiển giao thông thông minh; Điều khiển quá trình trong nhà máy; Tự động hóa trong công nghiệp tàu thủy; Tự động hóa trong nông nghiệp, lâm nghiệp và thủy sản; Tự động hóa trong nước cấp và nước thải; Tự động hóa cao ốc, nhà thông minh; Tự động hóa trong hầm mỏ, khai thác khoáng sản và luyện kim; Tự động hóa trong chế tạo máy; Tự động hóa trong ngành dệt may và da giầy; Tự động hóa trong lĩnh vực năng lượng, điện năng và năng lượng tái tạo; Ứng dụng điều khiển trong lĩnh vực hàng không vũ trụ; Ứng dụng trong an ninh, quốc phòng; Ứng dụng trong giáo dục và đào tạo; Ứng dụng trong y tế và chăm sóc sức khoẻ cộng đồng; Ứng dụng trong phòng chống thiên tai và xử lý ô nhiễm môi trường; Điều khiển-giám sát cho hệ thống chống ngập thành phố; Các ứng dụng khác…

Quy cách nộp bài:

Bài báo phải là công trình công bố các kết quả nghiên cứu và ứng dụng mới, được viết bằng tiếng Việt hoặc tiếng Anh theo định dạng của Hội nghị VCCA-2021. Quy cách viết bài xin tham khảo ở trang web Hội nghị http://vcca.engineer/vcca2024/vi/ và nộp trực tuyến trang **https://easychair.org/conferences/?conf=vcca2024** trước ngày **15/01/2024.** Khi bài báo được chấp nhận, tác giả phải đăng ký tham dự và trình bày tại Hội nghị. Các báo cáo không đăng ký trình bày sẽ không được đưa vào USB kỷ yếu Hội nghị.

Đề xuất phiên báo cáo chuyên đề:

Hội nghị VCCA-2024 khuyến khích các đề xuất mở phiên báo cáo theo các chuyên đề riêng tại Hội nghị của các tổ chức hay cá nhân nghiên cứu và đào tạo liên quan đến lĩnh vực Điều khiển và Tự động hóa. Các đề nghị này xin gửi trực tiếp tới Trưởng ban Chương trình theo địa chỉ email: tqvinh@ioit.ac.vn

Quảng cáo và triển lãm:

Các đơn vị, cá nhân có nhu cầu quảng cáo, triển lãm giới thiệu sản phẩm, dịch vụ tại Hội nghị và trong các ấn phẩm của Hội nghị xin liên hệ trực tiếp tới Ban Tổ chức của Hội nghị.

Tài trợ cho Hội nghị:

Ban tổ chức Hội nghị đánh giá cao và kêu gọi các đơn vị và cá nhân tài trợ, ủng hộ bằng hiện vật, dịch vụ hay ngân khoản để Hội nghị VCCA-2024 thành công tốt đẹp. Mọi tài trợ bằng hiện vật hay dịch vụ xin liên hệ với Ban Tổ chức Hội nghị. Mọi tài trợ cho Hội nghị đều được ghi danh và công bố ở Hội nghị.

Các thông tin chi tiết xin liên hệ với Ban Tổ chức Hội nghị:

P. 413, số 24 Lý Thường Kiệt, Hà Nội; Tel: (+84) 24 32669648; 0983094278; Email: tudonghoavp@gmail.com

Các mốc thời gian:

Nộp toàn văn báo cáo:	**31/5/2023 – 31/12/2023**
Thông báo chấp nhận bài:	**31/01/2024 – 15/3/2024**
Nộp bài đã hoàn thiện:	**16/3/2024 – 15/4/2024**
Đăng ký tham dự Hội nghị:	**16/4/2024 – 05/5/2024**
Hội nghị:	**10-11/5/2024**

Cơ quan tổ chức

Hội Tự động hóa Việt Nam

Cơ quan phối hợp

Trường ĐH Hàng Hải Việt Nam
Sở KHCN Hải Phòng
Công ty cổ phần VIETFAIR

Cơ quan bảo trợ

Bộ Khoa học và Công nghệ (MOST)
Bộ Công thương (MOIT)
Liên hiệp các Hội Khoa học và Kỹ thuật Việt Nam (VUSTA)
Phòng Thương mại và Công nghiệp Việt Nam (VCCI)
Viện Hàn lâm Khoa học và Công nghệ Việt Nam (VAST)

Chủ tịch Hội nghị

TS. Nguyễn Quân	Chủ tịch Hội TĐH Việt Nam

Hội đồng Cố vấn

GS.TSKH. Nguyễn Xuân Quỳnh	Nguyên CT HĐ CDGSNN
TS. Nghiêm Vũ Khải	Nguyên Phó CT VUSTA
TS Đoàn Duy Khương	Nguyên Phó CT VCCI
Ông Phạm Việt Tiến	Nguyên Phó TGĐ Đài THVN
TS Lê Xuân Rao	Chủ tịch Liên hiệp Hội HN

Trưởng Ban Tổ chức

TS. Dương Nguyên Bình	Phó CT Hội TĐH Việt Nam

Phó Trưởng Ban Tổ chức

PGS.TS. Phạm Xuân Dương	HT Trường ĐH Hàng Hải VN
PGS. TS. Bùi Quốc Khánh	Phó CT Hội TĐH Việt Nam
PGS. TS. Lê Hoài Quốc	Chủ tịch Hội TĐH TP HCM
TS. Bùi Thanh Tùng	Chủ tịch Hội TĐH TP HP

Trưởng Ban Doanh nghiệp

Ông Nguyễn Cẩm Tú	Phó CT Hội TĐH Việt Nam

Phó Trưởng Ban Doanh nghiệp

Ông Nguyễn Đoàn Thăng	Cty CP BĐ PN Rạng Đông
Ông Đinh Văn Hiến	Công ty DKNEC
Ông Nguyễn Viết Toàn	Công ty ETEC
Bà Lê Thị Hồng Loan	Công ty Hàn Mỹ Việt
Ông Nguyễn Văn Ngân	Công ty Vietfair

Trưởng Ban Chương trình

PGS.TS. Thái Quang Vinh	Viện CNTT, VHLKHCNVN

Phó Trưởng Ban Chương trình

GS.TSKH. Hồ Đắc Lộc	ĐH Công nghệ TP HCM
GS.TSKH. Nguyễn Công Định	Học viện KTQS
GS.TSKH. Nguyễn Phùng Quang	ĐHBK Hà Nội
GS.TS. Hồ Phạm Huy Ánh	ĐH BK, ĐHQG TP HCM
PGS.TS. Nguyễn Quang Địch	ĐHBK Hà Nội
PGS.TS. Lê Hoài Quốc	Hội TĐH TP HCM
PGS.TS. Nguyễn Chí Ngôn	Trường ĐH Cần Thơ
PGS.TS. Nguyễn Hữu Công	ĐH Thái Nguyên
PGS.TS. Nguyễn Thanh Sơn	ĐH Hàng Hải VN

Ủy viên Ban Chương trình

PGS.TS. Trần Sinh Biên	ĐH Hàng hải VN
PGS.TS Phan Thị Thanh Bình	ĐHBK Tp. HCM
PGS.TS. Nguyễn Quốc Chí	ĐHBK Tp. HCM
TS. Đỗ Mạnh Cường	ĐHBK Hà Nội
TS. Nguyễn Mạnh Cường	Học viện KTQS
PGS.TS. Nguyễn Tăng Cường	Học viện KTQS
PGS.TS. Trần Anh Dũng	ĐH HàngHải VN
PGS.TS. Lê Tiến Dũng	ĐHBK, ĐH Đà Nẵng
PGS.TS. Lê Bá Dũng	Viện CNTT, VHLKHCNVN
PGS.TS. Phạm Trung Dũng	Học viện KTQS
PGS.TS. Đỗ Trung Hải	ĐH KTCN, ĐHThái Nguyên
PGS.TS. Nguyễn Thanh Hải	ĐH GTVT Hà Nội
GS.TS. Đào Văn Hiệp	Học viện KTQS
PGS.TS. Nguyễn Quang Hoan	Học viện CN BCVT
PGS.TS. Huỳnh Đức Hoàn	ĐH Quy Nhơn
GS.TSKH. Thân Ngọc Hoàn	ĐH Dân lập Hải Phòng
PGS.TS. Huỳnh Thái Hoàng	ĐHBK, ĐHQGTP HCM
PGS. TS. Nguyễn Như Hiển	ĐH KTCN, ĐHThái Nguyên
TS. Phan Văn Hiền	ĐHBK, ĐH Đà Nẵng
TS. Trần Thanh Hùng	ĐH Cần Thơ
PGS.TS. Nguyễn Đức Khoát	ĐH Mỏ-Địa chất Hà Nội
TS. Nguyễn Ngọc Khoát	ĐH Điện lực
TS. Trương Đăng Khoa	Học viện KTQS
PGS.TS. Nguyễn Ngọc Lâm	PV VIETLINA, TP.HCM
GS.TS. Lê Hùng Lân	ĐH GTVT Hà Nội
PGS.TS. Nguyễn Văn Liễn	ĐHBK Hà Nội
PGS.TSKH. Trần Hoài Linh	ĐHBK Hà Nội
PGS.TS. Nguyễn Tùng Lâm	ĐHBK Hà Nội
PGS.TS. Nguyễn Tấn Lũy	ĐH Công nghiệp Tp.HCM
TS. Mai Thăng Long	ĐH Công nghiệp Tp.HCM
TS. Nguyễn Hoàng Mai	ĐHBK, ĐH Đà Nẵng
PGS.TS. Tạ Cao Minh	ĐHBK Hà Nội
PGS.TS. Trần Trọng Minh	ĐHBK Hà Nội
GS.TS. Phan Xuân Minh	ĐHBK Hà Nội
TS. Phạm Ngọc Minh	Viện CNTT, VHLKHCNVN
TS. Trần Thế Nam	ĐH Hàng Hải VN
PGS.TS. Nguyễn Văn Nhờ	ĐH BK Tp HCM
PGS.TS. Dương Hoài Nghĩa	ĐH BK Tp HCM
GS. TS. Nguyễn Doãn Phước	ĐH BK Hà Nội
PGS.TS. Nguyễn Chí Sáng	Viện NC Cơ khí
TS Lê Đình Phong	ĐH Hoa Sen
PGS.TS. Nguyễn Vũ Quỳnh	ĐH Lạc Hồng
TS. Nguyễn Ngọc Tân	ĐH Bình Dương
PGS.TS. Trần Đức Thuận	Viện KH và CN Quân sự
PGS.TS. Vũ Hòa Tiến	Học viện KTQS
PGS.TS. Nguyễn Tân Tiến	ĐH BK, ĐHQG TP HCM
TS. Nguyễn Mạnh Tiến	Viện Vật lý, VHLKHCNVN
TS. Nguyễn Thế Truyện	Viện ĐT-TH-TĐH (VIELINA)
PGS.TS. Đinh Anh Tuấn	ĐH Hàng Hải VN
TS. Phạm Minh Tuấn	Viện CNVT, VHLKHCNVN
TS. Ngô Duy Tân	Viện CNVT, VHLKHCNVN
PGS.TS. Trần Đức Tân	ĐH Phenika
TS. Đào Văn Tuyết	ĐH Bình Dương
PGS.TS. Bùi Đăng Thành	ĐHBK Hà Nội
PGS.TS. Nguyễn Trọng Thắng	ĐH Thủy lợi
PGS.TS. Nguyễn Văn Tiềm	ĐH GTVT Hà Nội
GS.TS. Phạm Thị Ngọc Yến	ĐHBK Hà Nội
PGS.TS. Đào Hoa Việt	Học viện KTQS

MỤC LỤC

CÔNG TRÌNH KHOA HỌC

Tháng 4/2024

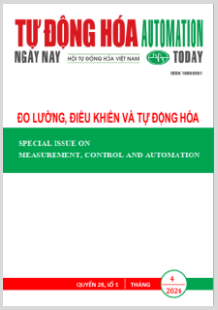

LIÊN HỆ PHÁT HÀNH
Tòa soạn tạp chí
P.406 - Tòa nhà Công nghệ cao
ĐH Bách khoa Hà Nội, số 1 Đại Cồ Việt
Quận Hai Bà Trưng, Hà Nội
Tel.: +84-24-35665327 / 35665328
Fax: +84-24-35665327
Email: tapchitudonghoa@gmail.com

Văn phòng đại diện phía Nam
Lầu 8, số 224 Điện Biên Phủ,
phường Võ Thị Sáu, quận 3, Tp.HCM
Tel: 0908855888

Tạp chí điện tử:
Website: www.vnautomate.net

Giấy phép xuất bản số:
276/GP-BTTTT ngày 05/09/2014
của Bộ Thông tin và Truyền thông

In tại Công ty TNHH MTV In quân đội 1
Giá: 80.000 - VNĐ

CONTENT

SCIENTIFIC PAPERS

April 2024

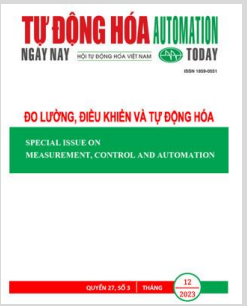

DISTRIBUTION
Journal office
P.406 - HighTech Building
Hanoi Uni. of Science and Technology
No. 1, Dai Co Viet Str.
District Hai Ba Trung, Hanoi
Tel.: +84-24-35665327 / 35665328
Fax: +84-24-35665327
Email: tapchitudonghoa@gmail.com

Southern represenative office
8th floor, No. 224, Dien Bien Phu,
Vo Thi Sau ward, District 3, HCM City
Tel: 0908855888

Online at:
Website: www.vnautomate.net

Publication license
276/GP-BTTTT 5th September 2014

Printed by MTV In quan doi 1 Ltd. Co.
Price: 80.000 - VND

Vol 5 (1) (2024)

Measurement, Control, and Automation

Website: https:// mca-journal.org

ISSN 1859-0551

Combination of Analytical Model and Finite Element Method for Designing High Voltage Shunt Reactors

Dung Dang Chi[1,*], Nam Phan Hoai[2], Hung Bui Duc[1], Tu Pham Minh[1], Hieu Dinh Thi Trung[3] and Vuong Dang Quoc[1]

[1]*Department of Electrical Engineering, School of Electrical and Electronic Engineering, Hanoi University of Science and Technology*
[2]*Faculty of Electrical Engineering, University of Economic and Technical Industries*
[3]*Faculty of technology and Engineering, University of Hai Duong*
[*]*Corresponding author: dung.dangchi@hust.edu.vn*

Abstract

Presently, shunt reactors (SRs) play a crucial role in addressing power quality issues. These SRs are designed to mitigate the reactive power in the system, manage high voltages, suppress power frequency fluctuations, regulate over-voltage, eliminate excitation in generators and dynamically compensate for transmission line power charges. The application of the finite element method (FEM) in the design of SRs has been recently presented by many researchers, particularly in both no-load and full-load conditions. However, its utilization in the manufacturing of electrical SRs remains relatively limited. In this study, it is split into two main steps. First, an analytical design is proposed to define the desired parameters with affects of different flux air gaps. Then, a finite element approach is introduced to simulate magnetic field quantities (such as inductance, fringing flux, magnetic flux density, electromagnetic force, current, voltage) of the SRs. The development of the methods is validated on the practical SR of 16 MVar, and a voltage of 500/√3.

***Keywords**: Shunt reactors, fringing flux, leakage flux, flux air gap, analytic model, finite element method*

1. Overview

To prevent overvoltage phenomena and maintain stable voltage at the end of transmission lines with a voltage rating of 110kV or higher during light or no-load system operation, shunt reactors (SRs) are employed to absorb and balance reactive power. Recently, many researchers have conducted numerous studies on shunt reactors, as follows:

In reference [1], a research group utilized the finite element method (FEM) to compute and analyze the reactance of SRs to establish the relationship between the total reactance and the leakage reactance between core blocks. In reference [2], an analytical method was developed to calculate the geometric parameters of the core and winding of SRs. The obtained results were compared to the FEM. In reference [3], [4], the authors applied the FEM to provide a solution for reducing losses caused by eddy currents in the winding of SR by optimizing the air gap along the winding. This paper also investigated the fringing and leakage fluxes around the air gaps. In reference [5], the authors presented a method for calculating the air gap impedance in the magnetic circuit of the shunt reactor through the "Schwarz-Christoffel" transformation.

Despite many researchers have applied the FEM for computation, analysis, and modeling of the electrical parameters of SRs, assessing the impact of electromagnetic forces on the core block, however it still remains a significant challenge for researchers and reactor manufacturers when considering the flux air gaps on the output parameters of SRs.

In this study, it is split into two main steps. First, an analytical design is proposed to define the desired parameters with affects of different flux air gaps. Then, a finite element approach is developed to simulate inductances, leakage and fringing fluxes, magnetic flux density and electromagnetic force with different flux air gaps. The development of the methods is validated on the practical SR of 16 MVar, and a voltage of 500/√3.

In the first section, the problem statement is introduced, as previously described. The second section shows the modeling of a SR with one flux air gap. The third section presents the analtyical approach to defined the required parameters of the SR. The fourth section develops the FEM with magnetic vector potential formulations to calcualte electromagnetic parameters. The fifth section gives a practical test of SR to validate the theory developed by the two proposed methods. The final section summarizes the obtained results.

2. Model of a single phase SR

The model of single-phase SR used in the transmission grid system is depicted in Figure 1 [3]. To reduce the fringing and leakage fluxes appearing in the vicinity of core blocks and also avoid saturation of the SR, the core blocks usually divide into several flux air gaps with significant lengths as already presented in [4]. However, the extensive length of these air gaps results in the presence of significant leakage flux and stray magnetic flux around the air gaps, causing the the main magnetic flux to decrease. Therefore, to mitigate this leakage flux component, instead of using a single flux air gap with a

Received: 4 December 2023; Accepted: 29 December 2023.

large thickness, it is necessary to divide the air gap into smaller flux air gaps with maintaining the total length of the gaps constant as shown in Figure 1. This approach increases the reluctance around the air gap region and reduces the leakage and fringing fluxes. However, dividing a large flux air gap into smaller flux air gaps implies segmenting a long core block into smaller sections, which in turn impacts the structural integrity of the magnetic circuit SR. The flux air gaps along the core blocks depend on the key parameters of the reactor, such as reactive power, magnetic flux density, inductance, energy stored in the winding space and the flux air gaps. These air gaps can be determined using an analytical model

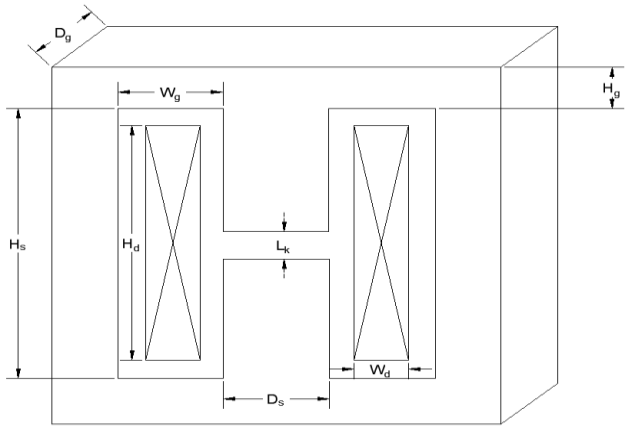

Figure 1. Model of a single phase SR [3].

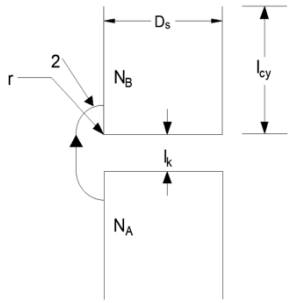

Figure 2. Fringing flux for an air gap along the core block [4].

3. Analytical approach

3.1. Computation of fringing flux of the SR

In this part, the main parameters of the single phase SR are defined via an analytica approach. Based on Figure 2, for a single flux air gap along the core block is considered. The magnetomotive force (MMF) is defined via the Ampere law, i.e., [2]-[5]:

$$F = \oint H.\,dl = H.\,(l_k + \pi.\,r) \tag{1}$$

where H is magnetic field intensity, l_k is the flux air gap thickness of the core block and r is the radius of fringing/leakage flux. The magnetic flux density (B) can be computed as:

$$B = \frac{\mu_o.\,F}{(l_k + \pi.\,r)} \tag{2}$$

The fringing flux (ϕ_{fring*}) around the single flux air gap of core block is then defined:

$$\phi_{fring*} = \frac{\int BdS}{F} = \int_0^{\frac{l_{cy}}{2}} \frac{\mu_o}{(l_k + \pi.\,r)} d_c d_r = \frac{\mu_o.D_s}{\pi} \ln\left(1 + \frac{\pi.\frac{l_{cy}}{2}}{l_k}\right) \tag{3}$$

It should be noted that the shape of core is the cylinder, for that it gets $d_c = \pi D_s$. For that, the equation (3) becomes as

$$\phi_{fring*} = \mu_o.\,D_s.\ln\left(1 + \frac{\pi.\,l_{cy}}{2.\,l_k}\right) \tag{4}$$

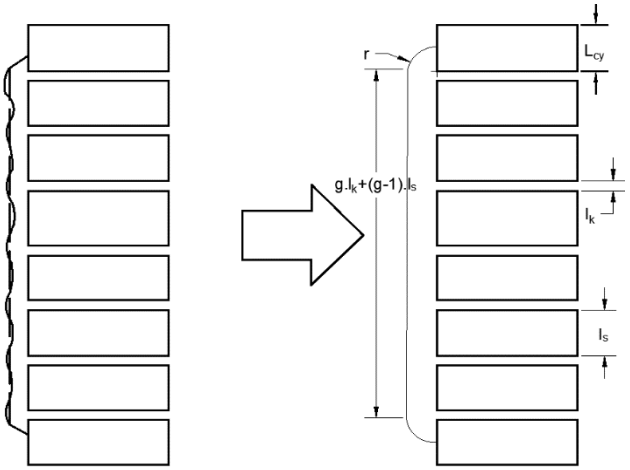

Figure 3. Model of several flux air gaps along the core blocks.

For the several flux air gaps as pointed out in Figure 3, the MMF is now defined as [6]-[10]:

$$F = \oint H.\,dl = H.\,((g-1)l_s + gl_k + \pi.\,r), \tag{5}$$

where l_s is the thickness of core block and g is the lenght of fringing flux and l_k is the thickness of flux air gap. In the same way, the term B can be calculated:

$$B = \frac{\mu_o.\,F}{((g-1)l_s + gl_k + \pi.\,r)} \tag{6}$$

The fringing flux ($\phi_{fring**}$) around the several flux air gaps is then defined:

$$\phi_{fring**} = \frac{\int BdS}{F} = \int_0^{l_{cy}} \frac{\mu_o}{((g-1)l_s + gl_k + \pi.\,r)} \pi D_s d_r = \frac{\mu_o.\,D_c}{\pi}.\ln\left(1 + \frac{\pi.\,l_{cy}}{(g-1)l_s + gl_k}\right) \tag{7}$$

3.2. Determination of main dimensions of the SR

In this part, the single phase SR of 16 MVar, the voltage (U) of $500/\sqrt{3}$, frequency of 50 Hz, is considered. The model of this SR is already given in Figure 1. The electromagnetic force (EMF) and the electric current can be defined as [3], [6]-[12]:

$$E = \left(\frac{2\pi}{\sqrt{2}}\right).f.N.\phi_m = \left(\frac{2\pi}{\sqrt{2}}\right).f.N.B_m.A_k \tag{8}$$

$$I = \frac{.R_g}{N} = \left(\frac{1}{\sqrt{2}}\right)\frac{B_m.l_g}{\mu_0.N}, \tag{9}$$

where:
- ϕ_m is the maximum magnetic flux,
- B_m is the maximum flux density,
- A_k is the area of the air gap,
- l_g is the length of the air gap,

- R_g air gap reluctance and air permeability.
- μ_0 is the permeability an N is the turn number.

Based on the equations (8) and (9), the volume (V_k) of the flux air gap is determined as:

$$V_k = A_k . l_k = \frac{Q}{\frac{\pi}{\mu_0} . f . B_m^2}. \quad (10)$$

The dimension of core block can be defined via the area of the flux air gap, that is

$$D_c = \sqrt{\frac{4 . A_k}{\pi}} \quad (11)$$

From the equation (11), the deep yoke (D_y) and the high yoke (H_y) of core block can be then defined as:

$$D_y = D_c, \; H_y = \frac{A_k}{2 . D_y}. \quad (12\ a\text{-}b)$$

The inductance of winding can be calculate via the expression [3]-[5]:

$$L = N^2 . \mu_0 . \left(\frac{A_k}{l_k}\right) = \left(\sqrt{\frac{L}{\mu_0 . (\frac{A_k}{l_k})}}\right)^2 . \phi_g \quad (13)$$

The magnetic conducting taken the fringing flux into account is expressed as

$$\phi_{g_f} = \frac{\phi_g + \phi_{fring*} + g\phi_{fring**}}{g} \quad (14)$$

The turn number is finally written via the term, i.e

$$N = \sqrt{\frac{L}{\phi_c + \phi_{g_f}}} \quad (15)$$

Based on the analytic theory developed as above, the analytic results of the proposed SR of 16 MVar are given in Table 1:

Table 1. Analytical results

Parameters	Symbol	Value
Reactive power	Q (MVAr)	16
Rated voltage	U (kV)	$500/\sqrt{3}$
Rated current	I (A)	55.25
Total inductance	L_{total} (H)	16.6
Fringing inductance	$L_{fringing}$ (H)	5.15
Gap inductance	L_{gap} (H)	10.27
Core dimension	D_s (mm)	572
Height of core	Hs (mm)	1534
Total air gap	l_k (mm)	256
Turn number	N (turn)	2853
Width of winding	Wd (mm)	211
Height of winding	Hd (mm)	1264
Gaps	g	5

4. Finite element method

4.1. Maxwell's equation

In this contex, the FEM is proposed to simulate and compute the inducances, magnetic field density and electromagnetic forces with the different flux air gaps in the proposed SR. The general set of Maxwell's equations defined in a studied domain Ω and its boundary ($\partial\Omega \equiv \Gamma$) are given as [13]-[18]:

$$\text{curl}\, \boldsymbol{e} = -\partial_t \boldsymbol{b} \quad \text{in} \quad \Omega, \quad (16)$$
$$\text{curl}\, \boldsymbol{h} = \boldsymbol{j}_s \quad \text{in} \quad \Omega_s, \quad (17)$$
$$\text{div}\, \boldsymbol{b} = 0 \quad \text{in} \quad \Omega, \quad (18)$$

where fields of $\boldsymbol{e}$, $\boldsymbol{b}$, $\boldsymbol{h}$, $\boldsymbol{j}_s$ are respectively the electric field (V/m), magnetic flux density (Wb), magnetic field intensity (A/m) and electric current density (A/mm^2). These fields satify function spaces defined inthe Tonti's diagram [11], that is, $\boldsymbol{e} \in \boldsymbol{H}_e(\text{curl}; \Omega)$, $\mathbf{j} \in \mathbf{H}(\text{div}; \Omega)$, $\boldsymbol{h} \in \boldsymbol{H}_h(\text{curl}; \Omega)$, $\boldsymbol{b} \in \boldsymbol{H}_e(\text{div}; \Omega)$. It should be noted that $\Omega = \Omega_c \cup \Omega_c^C$, where Ω_c is the conductive domain and Ω_c^C is the non conductive domain.

The equations from (16) to (18) are solved with the behavior laws and the boundary conditions (BCs), i.e.,

$$\boldsymbol{b} = \mu \boldsymbol{h}, \; \boldsymbol{j} = \sigma \boldsymbol{e}. \quad (19\ a\text{-}b)$$
$$\boldsymbol{n} \cdot \boldsymbol{B}|_{\Gamma_e} = 0, \; \boldsymbol{n} \times \boldsymbol{H}|_{\Gamma_h} = 0, \quad (20\ a\text{-}b)$$

where parameters μ and σ are respectively the permeability and electric conductivity, and $\boldsymbol{n}$ is the normal unit.

The magnetic flux density $\boldsymbol{b}$ is presented via the magnetic vector potential ($\boldsymbol{a}$), i.e, $\boldsymbol{b} = \text{curl}\, \boldsymbol{a}$. Thus, the equation (16) is presented via the electric scalar potential (υ)

$$\boldsymbol{e} = -j\omega \boldsymbol{A} - \text{grad}\upsilon. \quad (21)$$

But, in Ω_c, the υ is fixed to be zero [18].

4.2. Weak finite element formulations

The weak formulations for magnetic vector potential ($\boldsymbol{a}$) is written based on the Maxwell's equations from (16) –(17), behavior laws (19 a-b), BCs (20a-b) and equation (22) [18]:

$$\int_\Omega \mu^{-1} \text{curl}\, \mathbf{a} \cdot \text{curl}\, \mathbf{w}' d\Omega + \text{j} \int_{\Omega_c} (2\pi f \sigma \mathbf{a} \cdot \mathbf{w}') d\Omega_c + \int_{\Omega_c} (\sigma \text{grad}\upsilon \cdot \mathbf{w}') d\Omega_c + \int_{\Gamma_h} (\boldsymbol{n} \times \mathbf{H}) \cdot \mathbf{w}' d\Gamma_h = \int_{\Omega_s} (\mathbf{j_s} \cdot \mathbf{w}') d\Omega_s, \mathbf{w}' \in \boldsymbol{H}_e^0(\text{curl}; \Omega), \quad (22)$$

where $\boldsymbol{w}'$ is the test function given in a function space $\boldsymbol{H}_e^0(\text{curl}; \Omega)$.

The trace of magnetic field is achievable, especially under conditions such as a homogeneous Neumann BC. This is exemplified by imposing a symmetry condition like "zero crossing current" or considering a perfect magnetic wall with infinite magnetic permeability. When the applied voltage is considered as global quantities, the υ can be defined as:

$$\upsilon = \sum_i V_i v_{s,i} \quad (23)$$

where $v_{s,i}$ is a basic function υ and V_i is the voltage drop on the electrodes [18].

By substituting (23) into (22), the equation (22) becomes:

$$\int_\Omega \mu^{-1} \text{curl}\, \mathbf{a} \cdot \text{curl}\, \mathbf{w}' d\Omega + \text{j} \int_{\Omega_c} (2\pi f \sigma \mathbf{a} \cdot \mathbf{w}') d\Omega_c$$

$$+\int_{\Omega_c}\left(\sigma\text{grad}\sum_i V_i v_{s,i}\cdot\mathbf{w}'\right)d\Omega_c+\int_{\Gamma_h}(\boldsymbol{n}\times\mathbf{H})\cdot\mathbf{w}'d\Gamma_h = \int_{\Omega_s}(\mathbf{j_s}\cdot\mathbf{w}')d\Omega_s,\ \mathbf{w}'\in\boldsymbol{H}_e^0(\text{curl};\Omega),\quad(24)$$

4.3. *Discretization of fields*

The fields $\boldsymbol{a}$ and υ in the equation (24) are discreted via the edge and node elements, i.e., [13].

$$\mathbf{a}=\sum_{e\in E(\Omega_c)}\mathrm{a_e}s_e+\sum_{e\in E(\Omega_c^C)\setminus E(\partial\Omega_c)}\mathrm{a_e}s_e,\quad(25)$$

$$\upsilon_s=\sum_{n\in N(\Gamma_h)}\upsilon_n,\quad(26)$$

where $E(\Omega_c)$ and $E(\Omega_c^C)$ are the set of element edges of Ω, s_e is the basic function linked to edge e, and $\mathrm{a_e}$ is the circulation of **a** along edge e in Ω. The $N(\Gamma_h)$ is the set of nodes defined in the BCs.

The associtation of equations (24), (25) and (26), the discreted equation is written as:

$$\int_\Omega\mu^{-1}\left(\text{curl}\sum_{e\in E(\Omega_c)}\mathrm{a_e}s_e\cdot\text{curl}\,\mathbf{w}'\right)d\Omega+\int_\Omega\left(\mu^{-1}\sum_{e\in E(\Omega_c^C)\setminus E(\partial\Omega_c)}\mathrm{a_e}s_e\cdot\text{curl}\,\mathbf{w}'\right)d\Omega+\int_{\Omega_c}\sigma\sum_{e\in E(\Omega_c)}\mathrm{a_e}s_e\cdot\mathbf{w}'d\Omega_c+\int_{\Omega_c}\left(\sigma\sum_{e\in E(\Omega_c^C)\setminus E(\partial\Omega_c)}\mathrm{a_e}s_e\cdot\mathbf{w}'\right)d\Omega_c+j\int_{\Omega_c}\left(2\pi f\sigma\,\text{grad}\sum_{n\in N(\Gamma_h)}\upsilon_n\cdot\text{grad}\sum_i V_i v_{s,i}\right)d\Omega_c=\int_\Omega(\mathbf{j_s}\cdot\mathbf{w}')d\Omega_s\quad(27)$$

5. Numerical test

In this part, a test problem is a single-phase SR of 16 MVar and a voltage of 500/√3 and freqency of 50 Hz. The electromagnetic parameters are now computed via the FEM, where the required results from the analytical approach are already given in Table 1. The geometry of a single phase SR is presented in Figure 4.

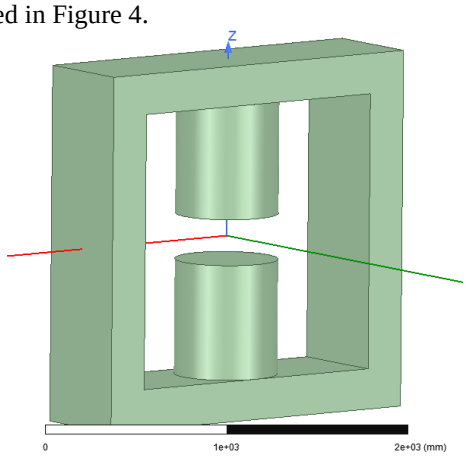

Figure 4. 3D model of a single phase high voltage SR.

The 3-D coarse mesh with edge and node elements is pointed out in Figure 5. The waveform of phase electric current distribution in the winding is shown in Figure 6. The distribution of magnetic vector potential due to the current flowing in the winding is presented in Figure 7. It can be seen that if the large air gap is divided into smaller air gaps, the fringing flux is evenly distributed in the flux air gaps along the core blocks and height of the winding without focussing on a single flux air gap. The maximum value reaches 1.226x10^{-7} (Wb/m).

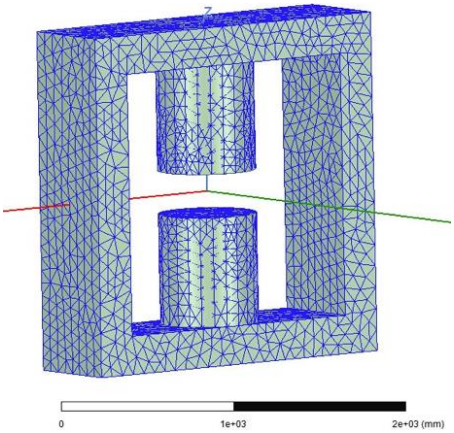

Figure 5. 3D mesh of a single phase high voltage SR.

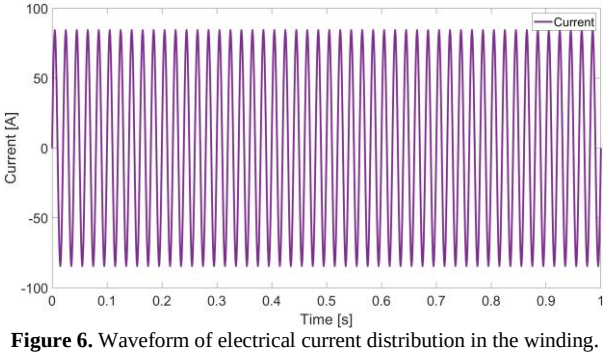

Figure 6. Waveform of electrical current distribution in the winding.

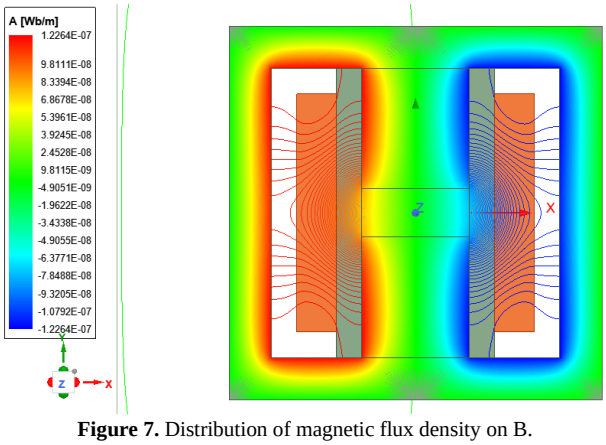

Figure 7. Distribution of magnetic flux density on B.

The distribution of fringing, air gap and total inductances is illustrated in Figure 8. The obtained results indicated that when the material used for the winding has a high permeability, and the air gap is sufficiently small, the flux density is mostly distributed in the core block without appearing the leakage or fringing flux. However, if the SR is designed with

one flux air gap intentionally at the core center with a large thickness, the magnetic flux leakage will be significant, resulting in a high reactive impedance and adversely affecting the performance of the magnetic core inductance [7]. Therefore, a large flux air gap divided into multiple smaller gaps will reduce the fringing and leakage flux along the core blocks. In order to overcome this difficulty as mentioned in [7], in this paper, instead of using a large flux air gap at the core center, it will be divided into five flux air gaps as shown in Figure 9.

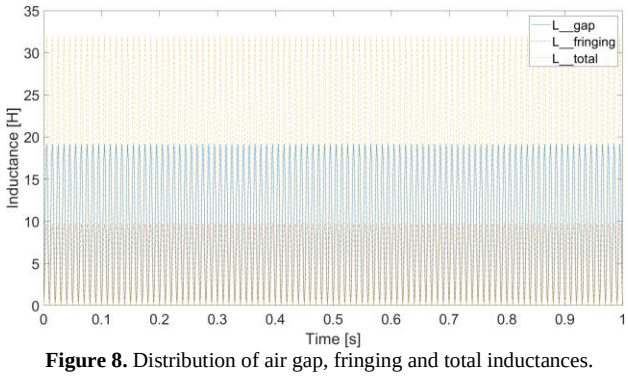

Figure 8. Distribution of air gap, fringing and total inductances.

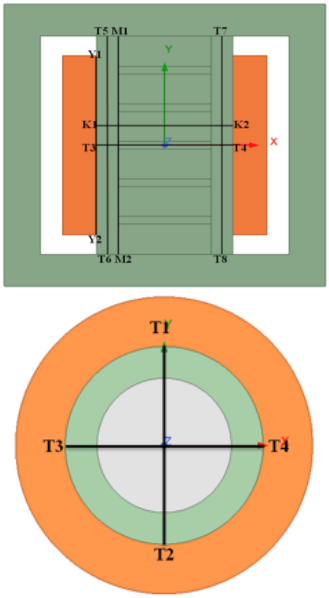

Figure 9. Model of the SR with five flux air gaps.

Figure 10 illustrates the distribution of magnetic flux density with five flux air gaps for the different positions along the winding and core blocks: T1T2, T3T4, T5T6, and T7T8. The magnetic flux density on the cut T5T6 decreases by 0.48 T compared to the case with a single air gap [7]. However, after five flux air gaps, this value mostly does not change.

Figure 11 presents the distribution of magnetic flux density along the segment Y1Y2 and M1M2. This result has indicated a variation in the percentage of leakage flux compared to the total flux value for the case of four flux air gaps (14 times). If the number of flux air gaps is increased to 5, the magnetic flux density along the segment Y1Y2 tends to be relatively uniform, and the leakage flux density through the air gaps significantly decreases.

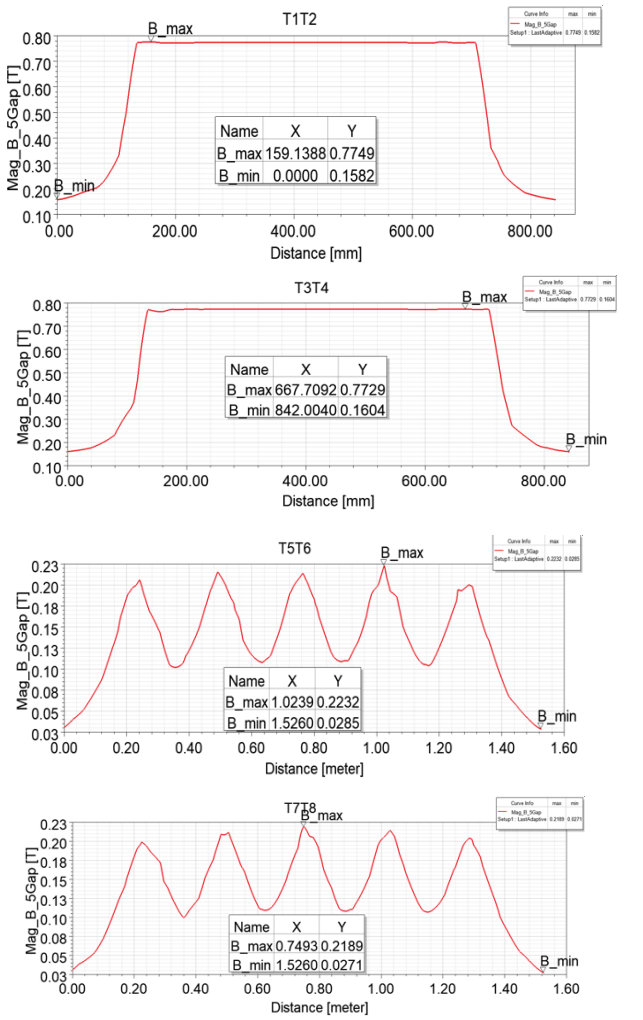

Figure 10. Distribution of magnetic flux density in air gaps along and across core blocks at the different positions T1T2, T3T4, T5T6 and T7T8 (see Figure 9).

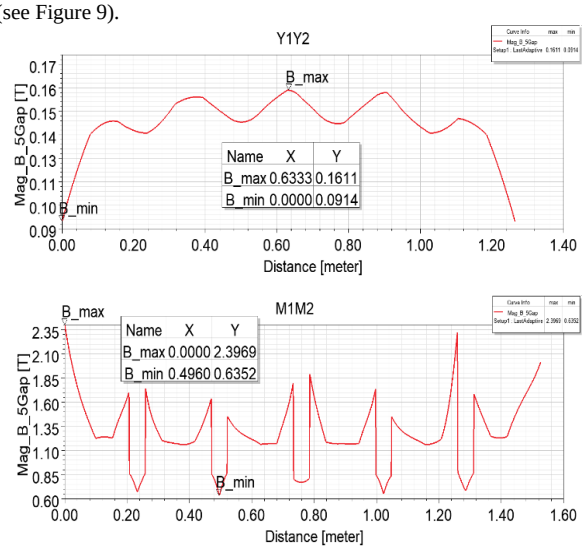

Figure 11. Distribution of magnetic flux density in air gaps and across core blocks at the different positions Y1Y2 and M1M2 (see Figure 9).

The distribution of electromagnetic force on the core blocks (K1K2) with five flux air gaps is pointed out in Figure 12. The value decreases by 1.03 times compared to the scenario with four flux air gaps, and this value remains relatively stable compared to the case with 4 air gaps (1.07 times).

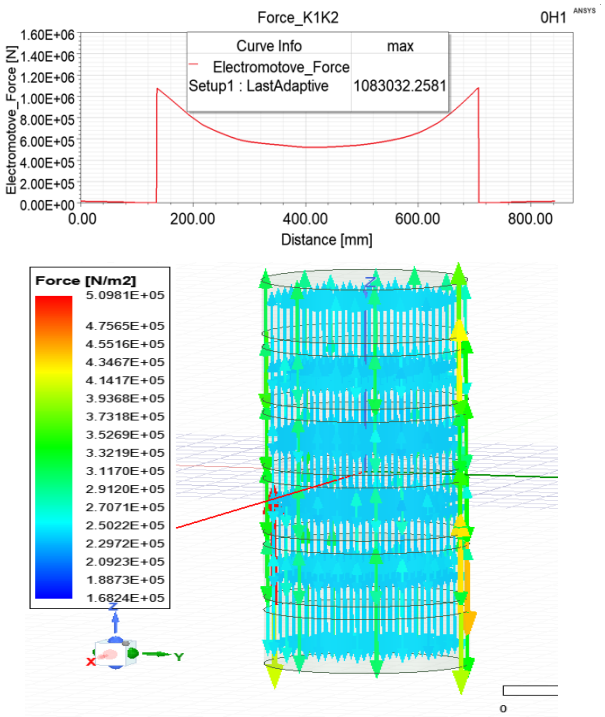

Figure 12. Distribution of electromagnetic force on the core block (K1K2) with five flux air gaps.

6. Conclusion

In this article, the combination of the two methods (analytical method and FEM) has been successfully developed for the single phase high voltage SR. The paper has investigated the distribution of magnetic vector potential in a single flux air gap, the magnetic flux density in five flux air gaps along and across the core blocks of the SR, and the electromagnetic forces acting on the core blocks as well. Via the simulated results, the division of the large flux air gap into the smaller air gaps has reduced the leakage and fringing flux in the flux air gaps. In particular, it can be shown that the electromagnetic forces acting on the upper and lower surfaces of the core blocks are in the same direction but opposite in magnitude, and approximately equal. Based on the obtained results, it will serve as reference data to assist designers and manufacturers to enhance and reinforce the structure of the partition plates between core blocks before production. Specifically, it has provided an appropriate choice of density for the steel core to reduce the electromagnetic forces acting on the surface of the core blocks and the surfaces of the partition plates between the core blocks. This will aid in optimizing the design and operation of SR to ensure the stability and performance of the electrical system.

Acknowledgment

This research is funded by Hanoi University of Science and Technology (HUST) under project number T2023-PC-042.

References

[1] Gagari Deb *"Ferranti Effect in Transmission Line"* International Journal of Electrical and Computer Engineering (IJECE) Vol.2, No.4, August 2012, pp. 447~451 ISSN: 2088-8708.

[2] A. Divya Swarna Sri *"Depiction and Compensation of Ferranti Effect in Transmission Line"* International Journal for Research in Applied Science & Engineering Technology (IJRASET) ISSN: 2321-9653; Volume 6 Issue III, March 2018.

[3] Tu Pham Minh, Hung Bui Duc and Vuong Dang Quoc. Analysis of Leakage Inductances in Shunt Reactors-Application to High Voltage Transmission Lines. Engineering, Technology & Applied Science Research (eISSN 1792-8036; pISSN 2241-4487), Vol. 12, no. 3, pp. 8488-8491 year 2022.

[4] Tu P. Minh, Hung B. Duc, Tuan P. Anh and Vuong D. Quoc**.** A Novel Approach for the Modeling of Electromagnetic Forces in Air-Gap Shunt Reactors. Engineering, Technology & Applied Science Research (eISSN 1792-8036; pISSN 2241-4487), Vol. 12, no. 1, pp. 8223-8227.

[5] Pham Minh Tu, Dang Quoc Vuong, and Bui Duc Hung. "Study of Number and Size of Air-Gaps in Core of Shunt Reactors in Tranmission Lines of High and Supper High Voltages". Journal of Military Science and Technology, no. 80, June 2022, pp. 23-30, doi:10.54939/1859-1043.j.mst.80.2022.23-30.

[6] T. P. Minh, H. B. Duc, and V. D. Quoc, "*Analysis of Leakage Inductances in Shunt Reactors: Application to High Voltage Transmission Lines*", *Eng. Technol. Appl. Sci. Res.*, vol. 12, no. 3, pp. 8488–8491, Jun. 2022.

[7] Hung Bui Duc, Dung Dang Chi, Dang, Q.-V., & Anh Hoang. (2023). Computation of Electromagnetic Parameters of Shunt Reactors Taken Corner Chamfers of Core Block into Account. *Measurement, Control, and Automation*, *4*(2), 42-46. Retrieved from https://mca-journal.org/index.php/mca/article/view/186

[8] A. Balakrishnan, W.T. Joines, T.G. Wilson, *"Air-gap reluctance and inductance calculations for magnetic circuits using a Schwarz-Christoffel transformation"* IEEE Transactions on Power Electronics 12 (July (4)) (1997) 654–663

[9] Lü, Fangcheng & Guo, Jiayi & Niu, Leilei & Geng, Jianghai & Pan, Yirui *"A New 3D Method for Reactor Core Vibration Based on Silicon Steel Lamination Rules and Application in UHV Shunt Reactors"* Mathematical Problems in Engineering. 2019. 1-11. 10.1155/2019/7290536.

[10] H. Amreiz, A. Janbey and M. Darwish, *"Emulation of Series and Shunt Reactor Compensation"* 2020 55th International Universities Power Engineering Conference (UPEC), 2020, pp. 1-6, doi: 10.1109/UPEC49904.2020 .9209786.

[11] D. I. Zaikin, S. Jonasen and S. L. Mikkelsen, *"An Air-Gap Shape Optimization for Fringing Field Eddy Current Loss Reductions in Power Magnetics"* in IEEE Transactions on Power Electronics, vol. 34, no. 5, pp. 4079-4086, May 2019, doi: 10.1109/TPEL.2018.28682 89.

[12] S.V. Kulkarni, S.A. Khaparde "*Transformer Engineering: Design, Technology, and Diagnostics*" Second Edition, ISBN 9781439853771, Published October 10, 2012 by CRC Press.

[13] Kamran Dawood "*Modeling of Distribution Transformer for Analysis of Core Losses of Different Core Materials Using FEM*" 2019 8th International Conference on Modeling Simulation and Applied Optimization (ICMSAO)

[14] F. Yuan et al., "Thermal Optimization for Dry Type Air Core Reactor Base on FEM," 2018 21st International Conference on Electrical Machines and Systems (ICEMS), 2018, pp. 1726-1730, doi: 10.23919/ICEMS.2018.8549257.

[15] S. Magdaleno-Adame, R. Escarela-Perez, J. C. Olivares-Galvan, E. Campero-Littlewood and R. Ocon-Valdez, "*Temperature Reduction in the Clamping Bolt Zone of Shunt Reactors: Design Enhancements*," in IEEE Transactions on Power Delivery, vol. 29, no. 6, pp. 2648-2655, Dec. 2014, doi: 10.1109/TPWRD.2014.2322994.

[16] Najafi, A., Iskender, I. "*Comparison of core loss and magnetic flux distribution in amorphous and silicon steel core transformers.* " Electr Eng 100, 1125–1131 (2018). doi:10.1007/s00202-017-0574-7

[17] K. Dawood, G. Komurgoz and F. Isik, *"Modeling of Distribution Transformer for Analysis of Core Losses of Different Core Materials Using FEM,"* 2019 8th International Conference on Modeling Simulation and Applied Optimization (ICMSAO), 2019, pp. 1-5, doi: 10.1109/ICMSAO.2019.8880392.

S. Koruglu, P. Sergeant, R.V. Sabarieqo, Vuong. Q. Dang, M. De Wulf "*Influence of contact resistance on shielding efficiency of shielding gutters for high-voltage cables*," IET Electric Power Applications, Vol.5, No.9, (2011), pp. 715-720.

Vol 5 (1) (2024)

Measurement, Control, and Automation

Website: https:// mca-journal.org

ISSN 1859-0551

Start-up Procedure for the Three-Phase Four-Leg Inverter in an AC Battery application

Tuan Anh Do[1,2], Quang Nghia Le[1], Thang Long Nguyen[1], Quang Dich Nguyen[1], Phuong Vu[1,]*

[1] *School of Electrical and Electronic Engineering, Hanoi University of Science and Technology, Hanoi, 100000, Vietnam.*
[2] *Institute for Control Engineering and Automation, Hanoi University of Science and Technology, Hanoi, 100000, Viet Nam.*
[*] *Corresponding author E-mail: phuong.vuhoang@hust.edu.vn*

Abstract

Three-Phase Four-Leg Inverter is getting so much attention due to its ability to deal with unbalanced AC voltage sources that can be caused by grid/load faults. Recently, the flexibility of this converter to connect both the 1-phase and 3-phase grid systems in a home battery application has further concern. A vast amount of literature that deals with this topology is exclusively focused on various modulation methods and control structures aimed at optimizing different aspects of its steady-state and/or transient performance. However, no literature is available on its start-up procedure in grid-tied mode which is an indispensable part of the control design of any practical circuit. To fill this gap, in this paper, a three-step start-up procedure for a three-phase four-leg Inverter in an AC Battery is proposed. The primary goal is to ensure that the inrush currents stay below a specific level while the output voltage increases to its reference value with a small overshoot. The proposed start-up procedure is illustrated via Hardware-in-the-loop (HIL) simulation results, which improves the feasibility of future experiments.

Keywords: *AC Battery, Hardware-in-the-loop, Three-Phase Four-Leg Inverter, Start-up Procedure*

Symbols

V_{dc_ref}	V	Reference DC Voltage
V_{ref}	V	Reference for modulation module

Abbreviations

PFC	Power Factor Correction
PV	Photovoltaic
AC	Alternating current
DC	Direct current
HIL	Hardware in the loop
DSP	Digital signal processing
OCP	Over current protection

1. Introduction

In recent years, the home battery has gained great interest thanks to its economic viability of capacity sharing [1] and increasing energy self-consumption [2-4]. This residential application is a combination of photovoltaic (PV) systems and an energy storage system using battery. There are two solutions for this application: AC-Coupled and DC-Coupled. This paper focuses on the AC-Coupled one because it can be easily retrofitted with the domestically installed PV system, its flexibility with extended modules, and isolation for the battery system. Furthermore, some companies have introduced a product named AC Battery that integrates both the battery and the power converter inside. A requirement of an AC Battery is the ability to connect to both 1-phase and 3-phase grid cords as well as operate properly in multiple conditions. To achieve that goal, this paper has selected the two-stage topology for the power energy conversion, and the three-phase four-leg (3P4L) structure is chosen for the Power Factor Correction (PFC) stage. This converter can be flexibly transformed into the 1-phase structure with two interleaved H-bridges [5]. In addition, the 3P4L has the capability of handling unbalanced loads in energy storage applications [6]. Literature on this subject mainly focuses on different control structures and modulation algorithms to deal with specific problems [8-11]. The start-up procedure is another important issue for operating the power converters [12]. However, the start-up control methods in the grid-connected mode of the three-phase four-leg inverter have not been a concern in the previous literature. Some research about this topic is only for the Three-Phase Three-Leg Inverter and different topologies of boost PFC converters [13-16]. One reason for this lack of academic community interest in start-up control issues might be the perception

Received: 20 September 2023; Accepted: 09 November 2023.

that the start-up control can be done easily with the traditional reference voltage ramp method. However, this is not entirely true. For some control structure that uses a modulation method with a low modulation index, using the conventional approach can be very challenging since there will not be enough DC voltage in the bulk capacitor after charging by the diode rectifier to perform the modulation.

In this paper, a detailed three-step start-up procedure for the three-phase four-leg inverter in the AC Battery is proposed. In the first step, the DC-link capacitor is charged by the three-phase bridge diode rectifier via precharge resistors, which are used to limit the charging currents. In the next step, the precharge resistors are shorted using in-rush current relays. Finally, the DC-link voltage is controlled by the DSP-controlled system to increase the reference value with a neglectable overshoot. Two different approaches to control the DC-link voltage in this final step, namely the Reference Voltage Ramp (The traditional method) and Constant Duty Cycle Ramp will be discussed. The reference voltage ramp start-up method will be mentioned first to show the props and cons of the traditional approach, while the constant duty ramp method will be introduced later to provide a solution to the problem that arises with the previous one. Matlab/Simulink simulation and Typhoon HIL + DSP experiment are also carried out on two different modulation methods, one with a high modulation index (Conventional Three-Dimensional Space Vector Modulation) and one with a low modulation index (Remote State Pulse Width Modulation) to verify the proposed start-up procedure in different situations.

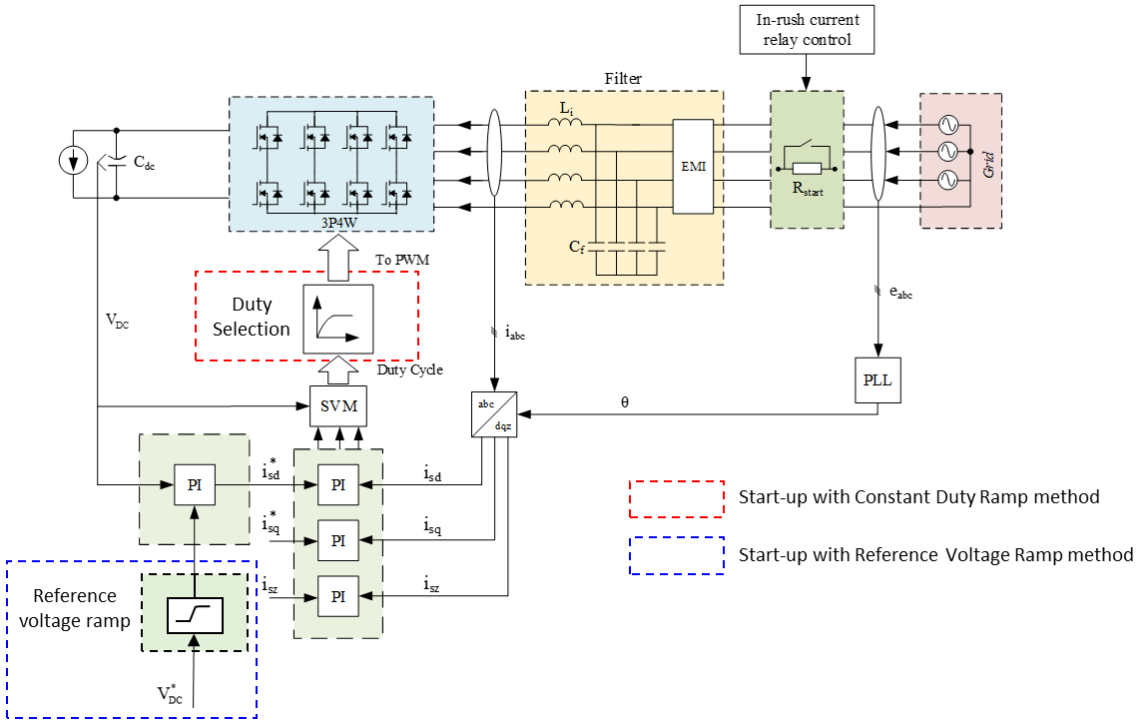

Figure 1: Control structure of the Three-Phase Four-Leg inverter

2. Main research

2.1. Power circuit and control of the system

The power circuit and control structure of a three-phase four-leg inverter is shown in Figure. 1. In this design, a basic Voltage-Oriented Control (VOC) control topology with two control loops is used to achieve PFC performance and ensures the output DC-link voltage increases to its reference value. Two modulation methods, one with high modulation index (Conventional Three-Dimensional Space Vector Modulation [8]) and one with low modulation index (Remote-State Pulse Width Modulation [9]), are discussed to point out the advantages and disadvantages of different start-up methods. A start-up module is added after the SVM module to avoid significant DC voltage overshoot and limit the inrush currents. The control structure is implemented with a digital signal processor (DSP) TMS320F28379D from Texas Instrument (TI) [17]. The phase currents and the grid voltages are sensed and converted to digital signals using the 12-bit Analog-to-Digital Converter (ADC) of the DSP. These digital signals are then used as input for the control program written in the Control Law Accelerator (CLA) of the DSP. The calculated duty cycles from the CLA will be fed into the enhanced Pulse Width Modulation (ePWM) to determine the gate signals for the upper and the lower switches of the Three-phase Four-leg power circuit.

2.2. Start-up procedure

This start-up procedure is presented in Figure 2, the DC-link capacitor charges from 0V to the reference value in three steps. Firstly, when all the switches are turned off, the DC-link capacitor charges slightly below the peak value of the line grid voltage using the bridge diodes of the switches and the start-up resistor. This resistor is used to limit the inrush current through the DC-link capacitor below the Over-Current Protection level and its value can be chosen in the worst case, i.e., when the grid voltage stays at its maximum value.

Secondly, the inrush current relays are turned on to comment the start-up resistors out of the system, hence the output voltage increases to the peak value of the phase-phase grid voltage. A short delay is applied after the relays are turned on to ensure enough time for the current transients to settle. Finally, the DC-link capacitor charges to its reference value by enabling the operation of the control loop. Two approaches to control the switches so that the PFC input currents and the DC output voltage do not experience abrupt changes, namely reference DC voltage ramp (the traditional method) and constant duty ramp (Set Duty) will be discussed respectively in the next subsection.

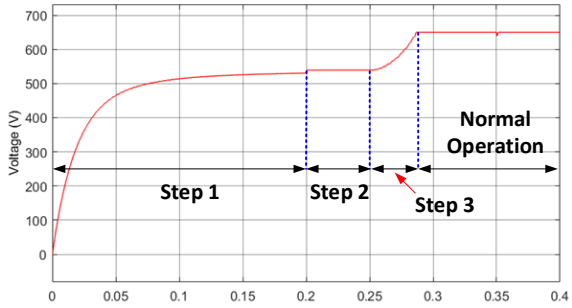

Figure 2: DC Output voltage during the start-up procedure

2.3. *Reference DC voltage (V_{dc_ref}) ramp*

This method has been widely used in most PFC structures that need to charge the DC capacitor to the reference value. The idea of this method is to ramp the output voltage by ramping up its reference value from the last value at the end of the second step to the desired value. Without the ramp process, the DC voltage response may experience a large overshoot as shown in Figure 3 and the inductor currents will exceed the Over-Current Protection (OCP) level due to the step reference. The big difference between the reference value and the present DC voltage value results in a large DC voltage controller output, which makes the control loop overreact to the drastic change and causes a big voltage overshoot and current spikes.

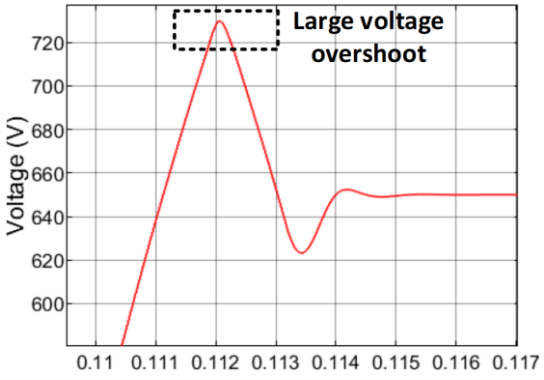

Figure 3: DC voltage response when a step reference is applied.

As can be seen from Figure 4, by adding the ramp block to gradually increase the reference voltage to the desired value, the unwanted overshoot voltage current spikes are almost canceled out. It is very clear that the strength of this approach comes from the simplicity of this method since it requires only a ramp module to achieve the desired start-up performance. Note that these are simulation results for a Three-Phase Four-Leg Inverter using a Three-Dimensional Space Vector Modulation (SVM-3D) modulation strategy.

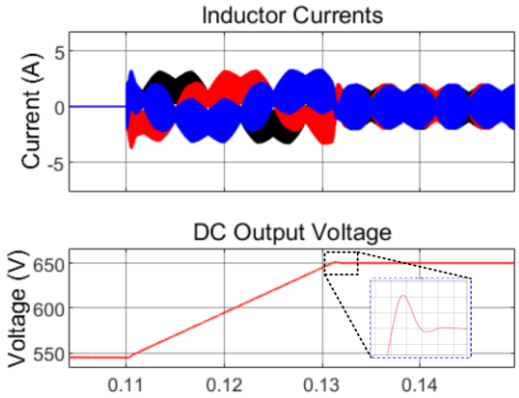

Figure 4: Matlab/Simulink simulation results of DC voltage, and inductor currents when the reference DC voltage ramp process is added

Although this method can reduce the charging current and make the output voltage increase steadily, it utilizes the duty cycles calculated from the SVM module and some modulation methods with low modulation index can raise difficulties for the system to remain in the stable region. For example, a known modulation method that is used to limit the leakage current in the Three-Phase Four-Leg PFC Inverter (RSPWM) [9] has the modulation index m within the range [0;1], with the modulation index defined as in (1):

$$m = \frac{2V_{ref}}{V_{DC}} \quad (1)$$

Where: V_{ref} is the reference voltage that is applied to the SVM module and V_{DC} is the DC voltage value.

This means that if the RSPWM modulation strategy is used, it requires at least double the reference voltage of the DC voltage to operate in the linear region. For the 380V phase-to-phase grid voltage system, the DC-link voltage after the second step can be calculated in (2):

$$V_{DC} = \sqrt{2}.V_{AC(L\text{-}L)} = \sqrt{2}.380 = 537(V) \quad (2)$$

Where: $V_{AC(L-L)}$ is the root-mean-square (RMS) phase to phase grid voltage.

The reference voltage that is applied to the SVM module can be determined from the phase-to-phase grid voltage in (3):

$$V_{ref} = \frac{\sqrt{2}.V_{AC(L\text{-}L)}}{\sqrt{3}} = \frac{\sqrt{2}.380}{\sqrt{3}} = 311(V) \quad (3)$$

Where: V_{ref} is the reference voltage that is applied to the SVM module.

It can be clearly seen that the DC-link voltage after the second step is lower than double the reference voltage, which is out of the linear modulation range of the RSPWM method. Stability problems may arise, and the controller will need to implement an anti-windup structure to adapt to this situation. Figure 5 shows the stability problem with the traditional approach when a low modulation index modulation strategy is used (RSPWM) and the effect of the anti-windup on the DC-link voltage response. Although this anti-windup structure can

help stabilize the system when the RSPWM modulation is working out of its linear modulation range, the voltage response fluctuates heavily around its reference value. A new ramp method must be proposed to overcome this problem and will be discussed in the next subsection.

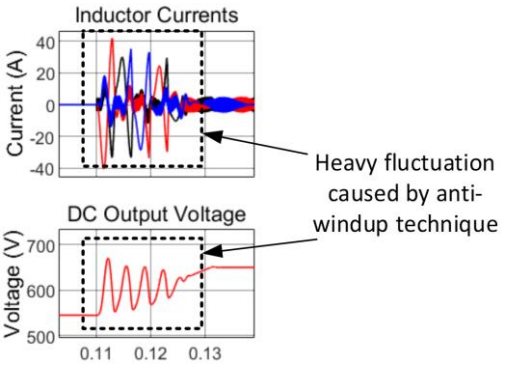

Figure 5: System response in the start-up procedure with RSPWM modulation method using Reference voltage ramp with anti-windup implementation.

2.4. Constant Duty Ramp

This method was developed from the duty cycle soft start method proposed in [13] but for the Three-Phase Three-Leg PFC. The same idea can be applied to a Three-Phase Four-Leg Inverter and achieve good start-up performance. However, the soft start duty cycle control also utilizes the calculated duty cycles from the control loop and for the same reason as the Reference Voltage Ramp, this method can't be used with a low modulation index modulation strategy. Note that the simulation results from Figure 6 are also taken from the test using the Conventional Three-Dimensional Space Vector PWM (SVM-3D) modulation technique.

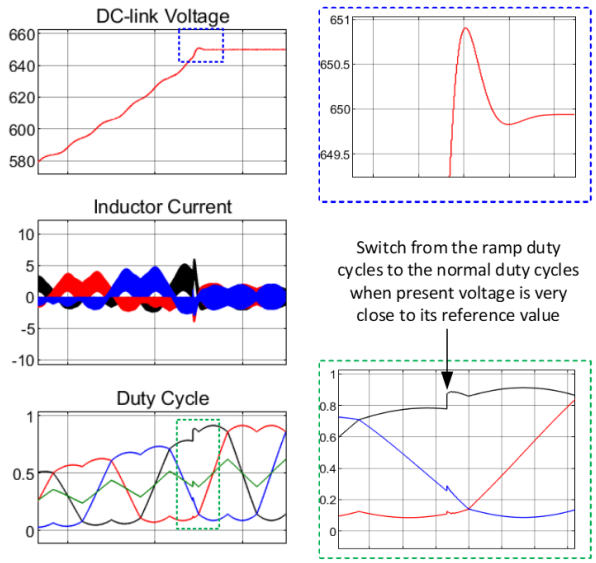

Figure 6: Matlab/Simulink simulation results with SVM-3D modulation strategy using the duty cycle soft start method.

The main difference between this Constant Duty Ramp method and the traditional Reference Voltage Ramp method comes in the use of the switching devices used in the start-up process. Instead of utilizing both the upper and lower switches in the start-up procedure, the Constant Duty Ramp method uses only the lower switches to charge the DC-link capacitor. All the lower switches are turned on with the same small duty while the upper ones are kept off until the end of the process. By applying this rule, when the lower switches are off, the inverter voltage v_{inva}, $v_{invb,}$ and v_{invc} in this interval are equal to the grid phase voltage v_{ga},$v_{gb,}$ and v_{gc}, respectively and there is no current through the filter inductors.

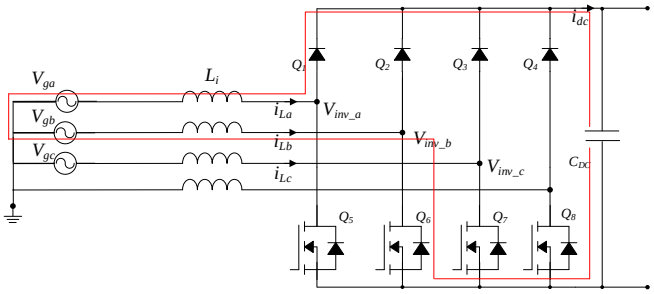

Figure 7: Current path for charging DC capacitor with the Constant Duty Ramp method.

When all the lower switches are turned on, as shown in Figure 8, the inverter voltages are clamped to zero, then the inductor current is generated which increases or decreases depending on the sign of each phase voltage at that moment. For example, in the analyzed interval in Fig. 8, v_{ga} is positive while v_{gb} and v_{gc} are negative, hence i_{La} is increasing while i_{Lb} and i_{Lc} are decreasing. However, at this moment, there is still no current through the body diode of switch Q_1 to charge the DC capacitor because this diode is in the reverse-biased state. After that, when the lower switches are turned off again, the diode of Q_1 is forward biased and the DC capacitor is charged slightly with the small charging current i_{dc} being equal to i_{La} as in Figure 8 and the current path being shown in Figure 7. When the inductor current i_{La} decreases to zero, the DC voltage stops increasing until the next turn-on signal for the lower switches.

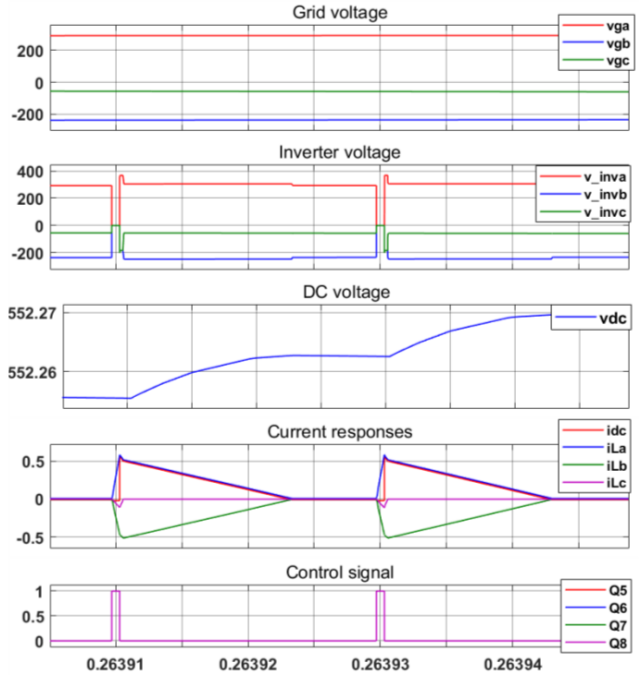

Figure 8: Key diagrams of the Constant Duty Ramp method

This method can be done only by applying constant duty cycles to the PWM so that the DC-link voltage will increase

gradually until the difference between it and the reference value is very small (just 1V for example). At this point, the lower switches will be enabled and the output voltage will be controlled to the reference value by applying the calculated duty cycles from the control loop.

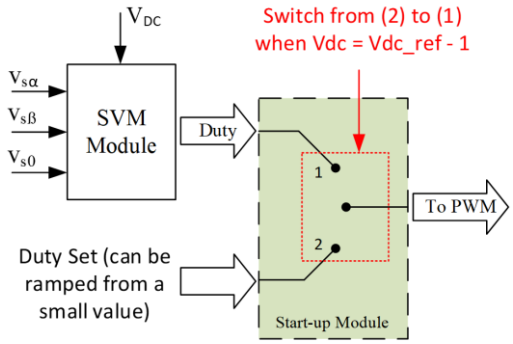

Figure 9: Constant duty ramp method block diagram

Since this method does not utilize the output duty cycles determined by the SVM module, the DC output voltage can increase to its reference value regardless of the modulation index of the modulation method used in the control structure. And thus it can overcome the problem that arises with the traditional reference DC voltage ramp approach. The constant duty ramp method is described via a block diagram in Figure 5. The constant duty cycles can be selected from a very small value to limit the inductor current at the start of step 3 (0.01 for example). However, too small a value can slow the process down and too large a value can result in big current spikes at the start of this stage. In order to both limit the PFC currents and enhance ramping procedure time, the duty cycles can be gradually increased from a small value to a large value instead of applying constant values as described in Figure 10.

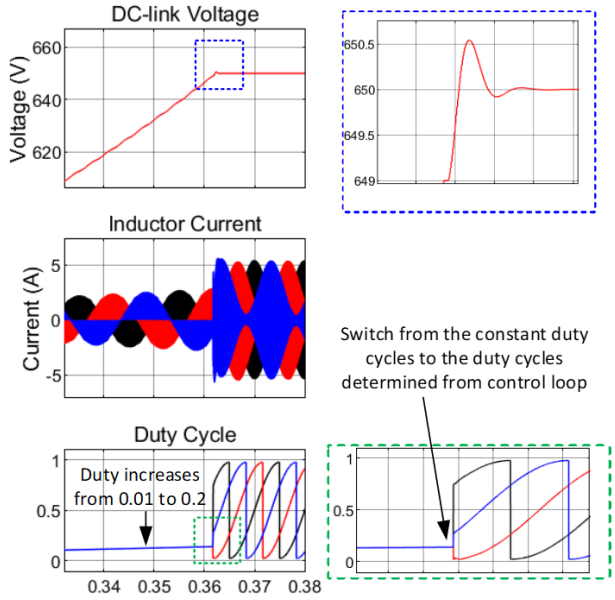

Figure 10: Simulation results of DC voltage, inductor currents, and duty cycles with the constant duty ramp method using the RSPWM modulation

Because of the ability to charge the DC capacitor without the need to concern about the modulation strategy used in the control loop, this method can be further used for different modulation strategies and/or different PFC topologies that require charging the bulk capacitor. A comparison between different start-up methods will be performed in the next section to show their strengths and weaknesses.

2.5. *Comparison of different start-up methods*

Simulations for different start-up methods with different PWM methods are carried out. The dynamic performances of voltage overshoot and current peak during the start-up procedure are compared and synthesized in Table 1. It can be clearly seen that while the RS-PWM method can not be started up with the Reference DC Voltage Ramp, the Constant Duty Ramp method is more viable than the other two methods due to its ability to charge the DC-link capacitor regardless of the modulation technique used in the control loop. Besides, this method introduces a similar current peak (5.2A and 4A) to the Reference Voltage Ramp method (3.6A). Furthermore, all three start-up methods can achieve neglectable voltage overshoot (around 0.5V – 1V), which ensures stability for the system to be ready for the next stage without faulting in the start-up process due to voltage and current clippings.

Table 1: Comparison between different start-up methods

	Reference DC Votlage Ramp		Constant Duty Ramp	
PWM method	SVM-3D	RS-PWM	SVM-3D	RS-PWM
Voltage Overshoot	1V	x	0.5V	0.5V
Peak current	3.6A	X	5.2A	4A

2.6. Hardware-in-the-loop Experimental

The proposed start-up procedure has been applied to a system with a rated voltage of 380 V_rms (line-line), rated power of 11kW, and DC output voltage of 650V. The Over-current protection level (OCP) in this research is selected at 20A, which is higher than the nominal phase current of 16.67A. The Over-Voltage Protection (OVP) level is selected at 700V for practical purposes.

Table 2: Main design parameters

Parameters	Value	Unit
Nominal Power	11	kW
Grid voltage (L-L)	380	V
Grid frequency	50	Hz
DC Output Voltage	650	V
Switching frequency	50	kHz
L filter	350	µH
DC-link capacitor	1000	µF
Precharge resistor	50	Ω
Over-Voltage Protection (OVP)	700	V
Over-Current Protection (OCP)	20	A

In order to illustrate the proposed start-up procedure, a Hardware-in-the-loop experiment is carried out using Typhoon HIL 402. Typhoon HIL is the real-time Hardware-in-the-loop platform for the design, testing, and validation of power electronics systems, which helps reduce the cost of testing and improve quality and reliability. This is used as a power circuit simulator which shows the system response when being controlled by digital controllers. The control loop is done via DSP C2000 TMS320F28379D from Texas Instrument (TI). The two devices are connected using a board connector that wired every PWM output pin from the TMS320F28379D development kit to the Digital Inputs (DI) of the Typhoon HIL and every ADCIN input pin from TMS320F28379D to the Analog Outputs (AO) of the Typhoon HIL. The pin configuration of

the DSP controller and the Typhoon HIL are shown in Figure 9 to describe how the experiment is carried out.

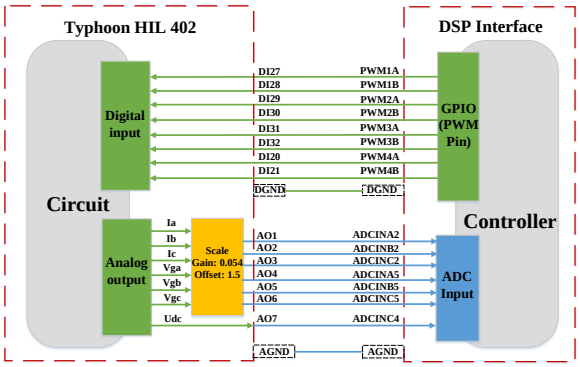

Figure 11: Pin configuration in the experiment setup

To better understand the pros and cons of each start-up method, four independent experiments are performed. Two of them are implemented with the reference voltage ramp start-up method using a high modulation index modulation strategy (SVM-3D) and a low modulation index modulation technique (RSPWM). The rest two cases are tested with the constant duty ramp method using the same modulation techniques as the first two cases. The results of all test scenarios are shown in Figure 12 and Figure 13. As can be seen from Figure 12a and Figure 12b, the case with the SVM-3D method shows great results: Low DC output voltage overshoot is less than 1V which meets the OCV standard, and low start-up currents (around 4A) that is under the OCP level during the start-up procedure.

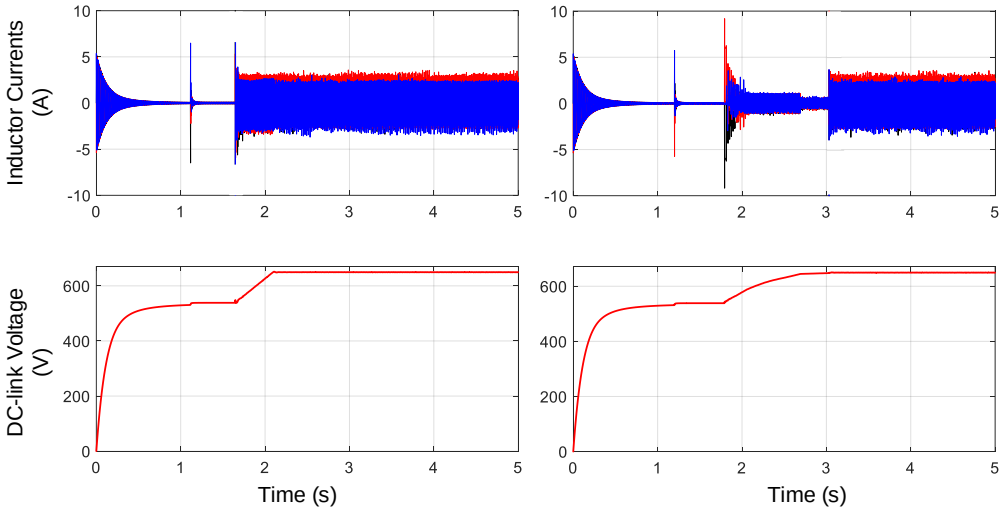

Figure 12: Experimental results. a) Reference voltage ramp with SVM-3D, b) Constant duty ramp with SVM-3D

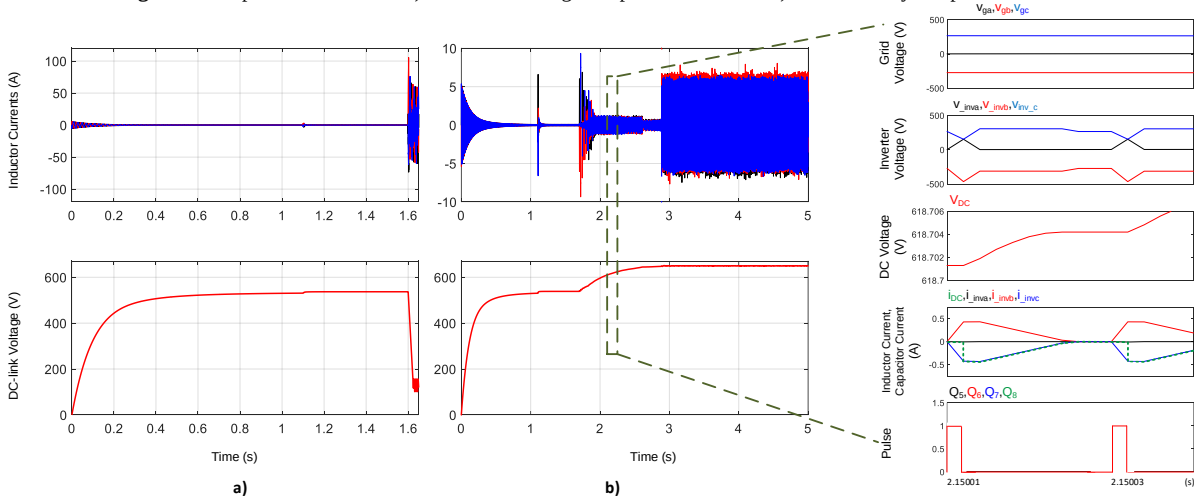

Figure 13: Experimental results. a) Reference voltage ramp with RSPWM; b) Constant duty ramp with RSPWM

However, the case with the RSPWM method shows the opposite. It is very clear from Figure 13a that the system is unstable with a peak current of around 100A and a sudden decrease of the DC voltage. This problem occurs because the DC-link voltage after the second step is not enough for the RSPWM method operating in the linear modulation range with the detailed equation presented in section 2.3. The controller then works unstably and the output of the DC voltage controller is quickly saturated, leading to high spikes and fluctuation in the output currents, which shows good agreement with the Matlab/Simulink simulation results.

Figure 12b and Figure 13b illustrate that the constant duty ramp start-up method is well adapted to both modulation techniques. The key diagram of this method with the RS-PWM method is similar to the theoretical analysis in section 3.2. This method utilizes constant duty cycles to ramp up the DC-

link voltage until it almost reaches the reference value, which ensures the RSPWM method performs within its linear modulation range. Although this method solved the problem with the traditional start-up approach, it introduced unwanted current peaks (around 6A) in the switching stage from the constant duty cycles to the duty cycles calculated from the control loop. It comes to the conclusion that if a high modulation index modulation strategy is used in the control loop, the reference voltage ramp method should be used due to its better current dynamic responses but if a low modulation index modulation method is used, the constant duty ramp should be prioritized due to its ability to ensure enough DC voltage for the system to operate normally.

3. Conclusion

In this paper, a three-step start-up procedure for a three-phase four-leg inverter in grid-connected mode is proposed. This procedure ensures that the inrush currents stay below the Over Current Protection (OCP) level and the output voltage increases to the reference value with a small overshoot. The reference voltage ramp method is introduced first to show the traditional approach to control the DC voltage to its reference value. However, this method has difficulty to apply for low modulation index modulation strategies such as RSPWM. The proposed start-up method, constant ramp duty, ensures enough DC voltage for the modulation to perform in its linear modulation range and helps stabilize the system without any complicated changes in the control loop. Hardware-in-the-loop experimental results using Typhoon HIL 402 and DSP TMS320F28379D also show good agreement with the theoretical analysis and the Matlab/Simulink simulation results, which improves the feasibility of future experiments.

Acknowledgment

Tuan Anh Do was funded by the Master, PhD Scholarship Programme of Vingroup Innovation Foundation (VINIF), code VINIF.2022.TS002.

References

[1] R. Dzikowski and B. Olek, "Capacity sharing — Economic analysis of home battery systems," 2017 14th International Conference on the European Energy Market (EEM), Dresden, Germany, 2017, pp. 1-5, doi: 10.1109/EEM.2017.7981991.

[2] E. Chatterji and M. D. Bazilian, "Battery Storage for Resilient Homes," in IEEE Access, vol. 8, pp. 184497-184511, 2020, doi: 10.1109/ACCESS.2020.3029989.

[3] T. Tungjittrong and N. Teerakawanich, "Design and Sizing of Home PV/Battery System with Energy Cost Constraint using Web Application," 2021 9th International Electrical Engineering Congress (iEECON), Pattaya, Thailand, 2021, pp. 129-132, doi: 10.1109/iEECON51072.2021.9440066.

[4] D. Farinet, M. Maurer, L. Vacca, S. V. Spataru and D. -I. Stroe, "Battery Lifetime Analysis for Residential PV-Battery System used to Optimize the Self Consumption - A Danish Scenario," 2019 IEEE Energy Conversion Congress and Exposition (ECCE), Baltimore, MD, USA, 2019, pp. 6693-6698, doi: 10.1109/ECCE.2019.8912280.

[5] Hedayati, Mohammad & John, Vinod. (2017). EMI and Ground Leakage Current Reduction in Single-Phase Grid-Connected Power Converter. IET Power Electronics. 10. 10.1049/iet-pel.2016.0568.

[6] P. Yang et al., "SiC-Based Improved Neutral Legs With Reduced Capacitors for Three-Phase Four-Wire EV Chargers," in IEEE Transactions on Transportation Electrification, vol. 8, no. 2, pp. 2565-2582, June 2022, doi: 10.1109/TTE.2021.3138333.

[7] P. Yang et al., "SiC-Based Improved Neutral Legs With Reduced Capacitors for Three-Phase Four-Wire EV Chargers," in IEEE Transactions on Transportation Electrification, vol. 8, no. 2, pp. 2565-2582, June 2022, doi: 10.1109/TTE.2021.3138333.

[8] P. K. Padhmakumar, M. P. Flower Queen and P. B. Aurtherson, "Three Dimensional Space Vector Modulation for Three Phase Four Leg Inverters - A Review," 2018 International Conference on Emerging Trends and Innovations In Engineering And Technological Research (ICETIETR), Ernakulam, India, 2018, pp. 1-8, doi: 10.1109/ICETIETR.2018.8529087.

[9] Hasanzad, Fardin & Rastegar, Hassan & B. Gharehpetian, Gevork & Pichan, Mohamad. (2017). Space Vector Modulation Technique to Reduce Leakage Current of a Transformerless Three-Phase Four-Leg Photovoltaic System. Iranian Journal of Electrical and Electronic Engineering. 13. 142-151. 10.22068/IJEEE.13.2.142

[10] P. N. Rao and J. Nakka, "Three-Phase Four-Leg Four-Wire Topology in High Power Factor Converter addressing the problem of unbalanced source currents," 2018 IEEE 8th Power India International Conference (PIICON), Kurukshetra, India, 2018, pp. 1-6, doi: 10.1109/POWERI.2018.8704390.

[11] M. Stecca, T. B. Soeiro, A. K. Iyer, P. Bauer and P. Palensky, "Battery Storage System as Power Unbalance Redistributor in Distribution Grids Based on Three Legs Four Wire Voltage Source Converter," in IEEE Journal of Emerging and Selected Topics in Power Electronics, vol. 10, no. 6, pp. 7601-7614, Dec. 2022, doi: 10.1109/JESTPE.2022.3199093.

[12] D. T. Anh, P. Vu, T. Vo-Duy and W. Martinez, "A Novel Soft-Start and -Stop Procedure for Current-Fed Dual Active Bridge," 2021 23rd European Conference on Power Electronics and Applications (EPE'21 ECCE Europe), Ghent, Belgium, 2021, pp. 1-8, doi: 10.23919/EPE21ECCEEurope50061.2021.9570677..

[13] M. Kumar, L. Huber and M. M. Jovanović, "Start-up procedure for three-phase six-switch boost PFC rectifier," 2014 IEEE Applied Power Electronics Conference and Exposition - APEC 2014, Fort Worth, TX, USA, 2014, pp. 1852-1859, doi: 10.1109/APEC.2014.6803558.

[14] A. Mallik, J. Lu, S. Zou, P. He and A. Khaligh, "Minimum inrush start-up control of a single-phase interleaved totem-pole PFC rectifier," 2018 IEEE Applied Power Electronics Conference and Exposition (APEC), San Antonio, TX, USA, 2018, pp. 754-759, doi: 10.1109/APEC.2018.8341096.

[15] B.G. Gu, J.H. Choi, and I.S. Jung, “Start-up current control method for three-phase PWM rectifiers with a low initial DC-link voltage,” J. Power Electron. (JPE), vol. 12, no. 4, pp. 587-594, Jul. 2012.

[16] Q. Zhang, T. Meng, H. Ben and W. Wang, "Implementation of a start-up scheme for single-stage full-bridge boost PFC converter," 2017 IEEE Transportation Electrification Conference and Expo, Asia-Pacific (ITEC Asia-Pacific), Harbin, China, 2017, pp. 1-5, doi: 10.1109/ITEC-AP.2017.8080872.

[17] Texas Instruments: TMS320F28379D Digital Signal Processor, Technical Reference Manual, 2011.

Vol 5 (1) (2024)

Measurement, Control, and Automation

Website: https:// mca-journal.org

ISSN 1859-0551

A Comparative Study of Machine Learning – based Models for Short-Term Multi-step Forecasting of Solar Power: An Application for Nhi Ha Solar Farm

Thu Nguyen Thi Hoai [1,*], Van Pham Nang [1], Khanh Ngo Van [1], Bach Do Xuan [1]

[1] *Power Grid and Renewable Energy Lab., School of Electrical and Electronic Engineering, Hanoi University of Science and Technology, Hanoi, Vietnam*

[*]*Corresponding author E-mail: thu.nguyenthihoai@hust.edu.vn*

Abstract

Over the past few decades, the utilization of solar power has gained immense significance in the power grid, gradually taking over the responsibilities of fossil fuel-based power. Therefore, accurate short-term forecasting of photovoltaic power output is crucial for making informed decisions regarding power generation, transmission, and distribution. Consequently, many machine-learning models were used to reliably forecast solar power. In this study, four machine learning models have been studied which are Artificial Neural Networks, Convolutional Neural Networks, Long Short-Term Memory (LSTM) and Extreme Learning Machine (ELM). They have been used to forecast the solar power of Nhi Ha solar farm in short-term. First, data from Nhi Ha solar farm were collected and underwent preprocessing before being utilized by aforementioned distinct machine learning models. The Root Mean Squared Error (RMSE) and normalized RMSE (N-RMSE) obtained from the models will be analyzed to determine the most effective model for short-term solar power forecasting. Following a comprehensive analysis, it has been determined that all four models have produced favorable outcomes, with low values of RMSE and N-RMSE indicating high levels of reliability and accuracy. Of the models considered, the LSTM and ELM models have demonstrated better performance, making them the good choice for precise short-term solar power forecasting.

Keywords*: Artificial Neural Networks, Convolutional Neural Networks, Machine learning, Short-term forecasting, Solar power*

Abbreviations

ANN	Artificial Neural Networks
CNN	Convolutional Neural Networks
ELM	Extreme learning machine
LSTM	Long short-term memory
RMSE	Root Mean Squared Error
N-RMSE	Normalized Root Mean Squared Error

1. Introduction

In recent years, the utilization of solar power in Vietnam has experienced a remarkable surge, with the government implementing plans to promote further use of this renewable energy source. In 2020, Decision 13/2020/QD-TTg was enacted, which introduced a variety of new incentives and mechanisms aimed at attracting investors to solar power projects within the country [1]**.** Considering Vietnam's accelerated expansion in the renewable energy sector, particularly in electricity, solar power is progressively becoming an indispensable element of Vietnam's power grid. This necessitates the development of precise and accurate forecasting models. The integration of solar energy into the power grid presents numerous challenges due to the highly volatile and unpredictable nature of solar energy sources. These characteristics are influenced by various environmental factors such as sunlight intensity, wind speed, and temperature. Any inaccuracies in forecasting can lead to errors in power grid management, potentially resulting in significant social and economic impacts that could disrupt businesses and civilian life. Consequently, the accurate forecasting of solar power is essential for ensuring the stability and maintenance of the power grid. The evolution and application of various forecasting models and technologies over recent decades have simplified the management of electricity in Vietnam, facilitating a more stable and seamless integration of solar power into the power grid.

Over the past several decades, numerous techniques have been developed to forecast the capacity of solar farms[2] . These forecasting methods can be classified in several ways, one of which is based on the forecasting models themselves. These categories include: Statistical methods (time series-based methods); Artificial intelligence methods; Physical methods; and Mixed methods (hybrid or ensemble methods) [3]. Statistical methods such as Autoregressive Moving Average (ARMA) [4], [5] or Autoregressive Integrated Moving Average (ARIMA) [6] have been widely used in various short-term solar power forecasting applications. However, these models often encounter several limitations, such as their inability to accurately forecast non-linear data or their dependence on historical data. To mitigate these inaccuracies, machine learning models or machine learning models are employed, yielding improved results.

Received: 21 November 2023; Accepted: 17 January 2024.

Owing to their superior performance, machine learning models have been increasingly adopted for short-term solar power forecasting. Common machine learning models include Artificial Neural Network (ANN), Convolutional Neural Network (CNN), Recurrent Neural Network (RNN), Long Short-Term Memory (LSTM), Auto-encoder (AE), among others. ANN is one of the most effective methods due to its adaptability to large fluctuations caused by changing environmental conditions [7]. CNNs have demonstrated significant effectiveness in short-term solar power forecasting. Utilizing temperature and solar irradiation as predictors, this algorithm has been used to predict the power output of a Photovoltaic (PV) system located in Italy, yielding satisfactory prediction results with a 10% error value. Lastly, LSTM is a model developed from the RNN model with the aim of mitigating RNN's weaknesses. LSTM-based model is particularly effective in dealing with time-series data and has demonstrated superior overall prediction accuracy for short-term forecasting [8] [9].

The primary contributions of this paper can be articulated as follows:

1. This paper studies four machine learning algorithms: Artificial Neural Networks (ANN), Convolutional Neural Networks (CNN), Long Short-Term Memory (LSTM) and Extreme Learning Machine (ELM). These algorithms are configured appropriately, and their results are compared to ascertain which algorithm yields the most accurate results. The comparison of these four algorithms could inform enhancements to future forecasting models, thereby assisting operators in maintaining power system reliability, preserving power quality, and mitigating uncertainty in the grid.
2. This paper aims to understand and apply 4 mentioned machine learning - based forecasting models to data collected from the Nhi Ha solar farm.

2. Methodology

2.1. Artificial Neural Network

Artificial Neural Network (ANN) is a type of machine learning model that mimics the human brain in information processing, problem-solving and self-learning abilities [10]. The ANN model presents several advantages, including its capacity to operate effectively with incomplete datasets and the ability to retain information throughout the entire network rather than relying on a database [11]. Nevertheless, it is crucial to acknowledge that the ANN is susceptible to overfitting and underfitting phenomena, exerting an impact on both the performance and generalization capabilities of the network [11]. ANN is composed of several parts mainly: Input layer, Hidden layer, and Output layer. The input layer is the first layer of nodes in ANN with the mission to receive input data from external sources. The hidden layers then take the information for processing. The obtained value from the hidden layers is sent to the output for further processing to obtain the final result. The output signal can be expressed as:

$$P_j = \sum_{k=0}^{n} w_{jk} h_k \quad (1)$$

Where:

P_j: Represent the output signal

w_{jk}: Represent the weighted strength of the connection between the neuron (j) and the hidden layer (k)

h_k: Represent the weighted sum of n signals for each hidden layer of k=1,2,3,…,n

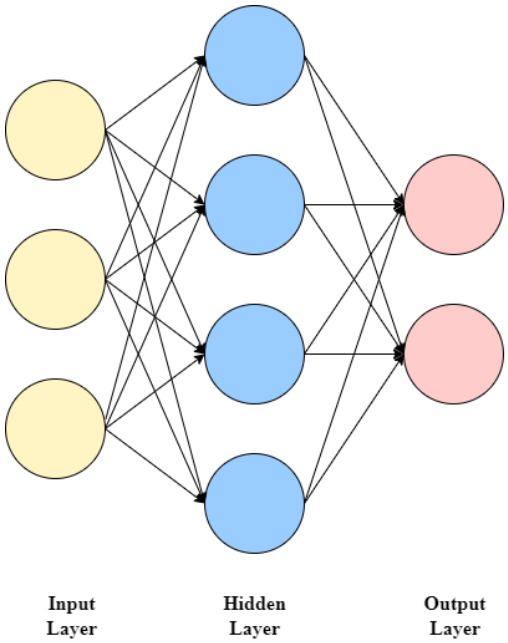

Figure 1: The structure of an ANN

2.2. Convolutional Neural Network

CNN is a type of feed-forward neural network mainly built for pattern recognition in images. It is mostly used for Object Detection [12], Image Classification [13], Face Recognition [14] etc. CNN is utilized in Computer Vision problems where data is composed of images passing through some optimization function and three layers namely: Convolutional Layer, Pooling Layer and Fully connected layer.

Apart from solving pattern recognition in image and Computer Vision problems, CNN can also be utilized in time-series forecasting by changing the dimensional structure of the input information.

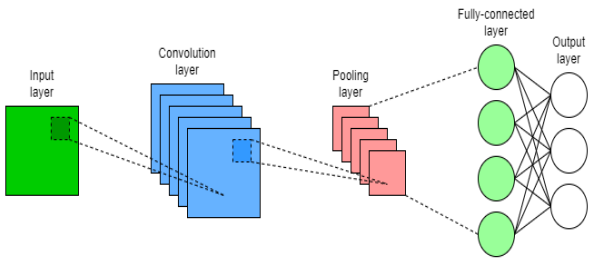

Figure 2: The structure of a CNN model

The following equation shows the output O of CNN calculation of some elements, where the Convolutional kernel is matrix P.

$$\begin{Bmatrix} o_{11} = f(\Sigma J \otimes P + b_1) \\ o_{21} = f(\Sigma J \otimes P + b_1) \\ o_{31} = f(\Sigma J \otimes P + b_1) \\ o_{12} = f(\Sigma J \otimes P + b_2) \\ o_{22} = f(\Sigma J \otimes P + b_2) \\ o_{32} = f(\Sigma J \otimes P + b_2) \\ o_{63} = f(\Sigma J \otimes P + b_3) \end{Bmatrix} \quad (2)$$

Beyond its advantages, the CNN model necessitates a substantial volume of data and resources for the training and optimization of network parameters. Furthermore, specialized hardware is imperative to expedite the computational processes associated with CNN, underscoring an additional requirement in its deployment. [15]

2.3. Long short-term memory

Recurrent Neural Networks (RNNs) are powerful machine learning models that have found use in a wide range of areas such as Speech Recognition [16], language translation [17] and image captioning problems [18]. When training a RNN model, one of the biggest problems is the "vanishing gradient". Long short-term memory (LSTM) [19] is a kind of RNN that was introduced to deal with the "vanishing gradient" problem in conventional RNNs. Furthermore, the LSTM model exhibits the capability to capture long-range dependencies and retain information over prolonged durations, rendering it well-suited for applications such as natural language processing and time series analysis [17]. Nevertheless, it is noteworthy that LSTM entails lengthier training periods and demands greater memory resources compared to simpler models, posing challenges in the context of large-scale applications [17]. Additionally, the susceptibility of LSTM to overfitting is particularly pronounced when confronted with limited or noisy training data. While dropout serves as a conventional technique to mitigate overfitting, its implementation in LSTM is more intricate compared to feedforward networks [17]. A LSTM unit is composed of: Forget gates, Input gates, the cell and the output gates. The forget gates filter redundant information by multiplying the value in the memory cell by a number of 0 or 1. The input gates determine which of the input values should be used to change the memory. The cell stores important information and the output gates control which information in the cell is kept as input value in the next timestep.

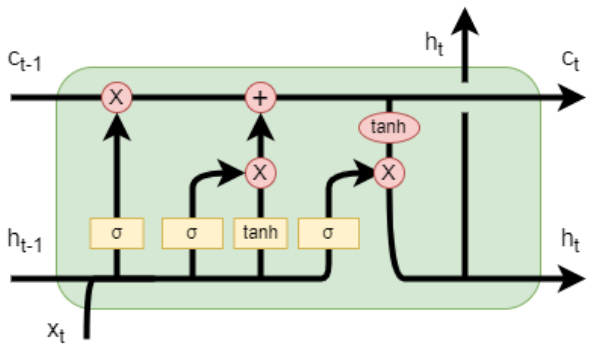

Figure 3: The structure of a LSTM unit

A LSTM block's mathematical model is presented by as follows:

$$i_t = \sigma(w_i[h_{t-1}, x_t] + b_i) \quad (3)$$
$$f_t = \sigma(w_f[h_{t-1}, x_t] + b_f) \quad (4)$$
$$o_t = \sigma(w_o[h_{t-1}, x_t] + b_o) \quad (5)$$
$$\bar{c}_t = tanh(w_c[h_{t-1}, x_t] + b_c) \quad (6)$$
$$c_t = (f \otimes c_{t-1}) \oplus (i_t \otimes \bar{c}_t) \quad (7)$$
$$h_t = o_t * \tanh(c_t) \quad (8)$$

Where:

i_t: represents input gate
f_t: represents forget gate
o_t: represents output gate
i_t: represents input gate
σ: represents sigmoid activation function
w_x: weight for the respective gate(x) neurons
h_{t-1}: output of the previous lstm block (at timestamp t-1)
x_t: input at current timestamp
b_x: biases for the respective gates(x)
c_t: cell state at timestamp(t)
$\bar{c}_t$: represents candidate for cell state at timestamp(t)

2.4. Extreme learning machine

ELM is a learning algorithm invented for the purpose of training single hidden layer feedforward neural network (SLFNs) and is known for its fast convergence and promising performance [20]. In contrast to the iterative interlayer weight updates in traditional neural network training algorithms, which utilize backpropagation, the Extreme Learning Machine (ELM) adopts a different approach. The weights connecting the input layer and the hidden layer are established through random initialization. Subsequently, the weights between the hidden layer and the output layer are learned using the least squares method. This methodology results in a rapid training process during the learning stage and swift inference during the testing stage. However, ELM's randomly assigned hidden layer parameters can also lead to overfitting, especially when the number of hidden nodes is large compared to the training data size [20]. While ELMs offer faster training compared to traditional neural networks, they also have less flexibility in terms of fine-tuning the model architecture. There is less control over the specific connections and weights in the hidden layer, which can limit the model's ability to capture complex relationships in the data [20]. Some applications of the model include classification [21] and regression [20] tasks.

For N different training data pairs (X_i , Y_i), $X_i = \left|x_{i_1}, x_{i_2}, \ldots, x_{ik}\right|^{\mathrm{T}} \in R^k$ is the ELM model input and $Y_i = \left| y_{i_1}, y_{i_2}, \ldots, y_{\mathrm{im}} \right|^{f' \in R^m}$ is the expected model output. If the activation function of the ELM with L hidden layer nodes is $g(x)$, the output function expression of the ELM is shown in Eq. (9).

$$\sum_{l=1}^{L} \beta_l g(b_l + W_l \cdot X_i) = O_i, i = 1, \ldots, N \quad (9)$$

where b_l is the threshold of the lth node of the hidden layer, $W_l = \left[\omega_{l_1}, \omega_{l_2}, \ldots, \omega_{\mathrm{lk}}\right]^{\mathrm{T}}$ is the weight connecting the input layer node and the lth hidden layer node, $\beta_{\mathrm{l}} = \left[\beta_{1_1}, \beta_{l_2}, \ldots, \beta_{\mathrm{lm}}\right]^{\mathrm{T}}$ is the weight connecting the lth hidden

layer node and the output layer node, $W_l \cdot X_i$ illustrates the inner product of W_l and X_i, and O_i is the output of the EIM model. In the ELM model calculation, the model output and expected output are equal; therefore, Eq. (10) can be obtained as follows:

$$\sum_{l=1}^{L} \beta_l g(b_1 + W_l \cdot X_i) = Y_i, i = 1, \dots, N \quad (10)$$

Eq. (10) is converted into the matrix representation in Eq. (11).

$$H\beta = Y \quad (11)$$

Where:

$$H = \begin{bmatrix} g(X_1 \cdot W_1 + b_1) & \cdots & g(X_1 \cdot W_L + b_L) \\ \vdots & \ddots & \vdots \\ g(X_N \cdot W_1 + b_1) & \cdots & g(X_N \cdot W_L + b_L) \end{bmatrix}_{N \times L} \quad (12)$$

$$\beta = \begin{bmatrix} \beta_1^T \\ \vdots \\ \beta_L^T \end{bmatrix}_{L \times m} \quad Y = \begin{bmatrix} Y_1^T \\ \vdots \\ Y_N^T \end{bmatrix}_{N \times m} \quad (13)$$

In the ELM model parameter training process, if $\bar{W}_l, \bar{b}_l$, and $\bar{\beta}_l$ can make Eq. (14) hold.

$$E = \min_{W,b,\beta} \sum_{L=1}^{N} \left(\sum_{L=1}^{L} \bar{\beta}_l g\left(\bar{W}_l \cdot X_l + \bar{b}_l\right) - Y_i \right)^2 = \min_{W,b,\beta} \| H\beta - Y \| \quad (14)$$

Then $\bar{W}_l, \bar{b}_l$ and $\bar{\beta}_l$ are the optimal ELM model parameters. In the ELM model, the determination of the input weight (W) and the hidden layer threshold (b) results in a unique output matrix (H) for the hidden layer. Given these conditions, the learning process of the ELM can be reformulated as a linear system.

$$\bar{\beta} = H^{-1}Y \quad (15)$$

Where H^{-1} is a generalized inverse matrix.

2.5. Data preprocessing

Prior to ingestion by the machine learning models, it is imperative to engage in preprocessing of the dataset. Within the context of this study, it is noteworthy that the original dataset is devoid of any missing values and manifests a consistent sampling interval of 30 minutes.

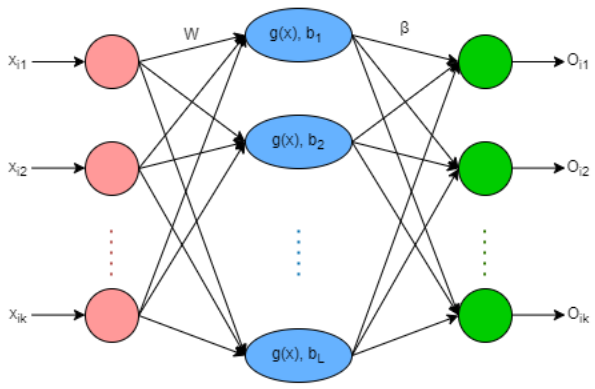

Figure 4: The structure of an ELM model

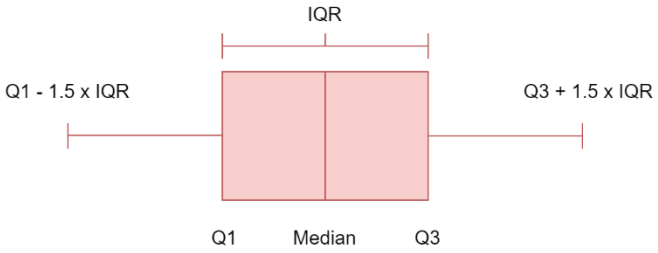

Figure 5: The Interquartile range (IQR)

Consequently, outlier detection be comes the sole preprocessing step necessary prior to deploying the dataset for forecasting purposes. The Interquartile Range (IQR) [22] is employed as the method of choice for outlier detection in this context.

The range of variations can be described using Figure 5, where:

Median: The central point that divides the dataset into upper and lower halves.

Q1, Q3: The first and third quartiles of the dataset.

Lower Bound: Q1 – 1.5 * IQR

Upper Bound: Q3 + 1.5 * IQR

The Interquartile Range (IQR) is calculated as the difference between the first quartile and the third quartile. An outlier is identified as a data point lying beyond the range defined by the Lower Bound and Upper Bound. Outliers detected are then determined to be replaced in the data set depending on their roles and importance.

2.6. Errors metrics

Error metrics are commonly used for analysis and comparison of different models. RMSE and N-RMSE are chosen as the metrics to compare the four machine learning models. RMSE and N-RMSE are defined using the following formula [23]:

$$\text{RMSE} = \sqrt{\frac{\sum_{i=1}^{N}(O_i - E_i)^2}{N}} \quad (16)$$

$$\text{N-RMSE} = \frac{\text{RMSE}}{\bar{O}} \times 100 \quad (17)$$

Where N was the number of validation data, O_i and E_i was the actual and estimated power value, respectively. $\bar{O}$ was the mean value of actual power value. In this study, the accuracy of the model was considered excellent when N-RMSE < 10%; good if 10% < N-RMSE < 20%; fair if 20% < N-RMSE < 30% and poor if N-RMSE ≥ 30% [23]

3. Data set

Table 1: Raw data from Nhi Ha power plant

No	Time	Output
1	6/21/2019 00:00	**0**
2	6/21/2019 00:30	**0**
3	6/21/2019 01:00	**0**
…	**…**	**…**
62159	1/08/2023 23:00	**0**
62160	1/08/2019 23:30	**0**

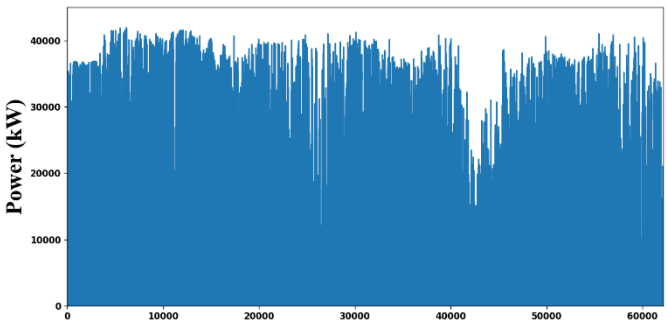

Figure 6: Output of Nhi Ha solar power plant

The data utilized in this study was meticulously gathered from the Nhi Ha Solar Power Plant, strategically situated in the Ninh Thuan province, a region in the southern part of Vietnam. The data was collected from 6/21/2019 00:00:00 to 01/08/2023 23:30:00 with a sample every 30 minutes. Because of this, there were a total of 62160 data points. Table 1 describes the raw data of the output obtained from the power plant. A visual representation of the solar power plant's output is provided in Figure 6 for further elucidation.

The output was recorded in kW. It is noteworthy to mention that the majority of deep learning models exhibit sensitivity to data scales, necessitating the standardization or normalization of the data. In the context of standardization, it is imperative that the mean of the data remains constant. Consequently, in this study, normalization of the data was executed within a range of 0 to 1.

During the application of the Interquartile Range (IQR) method for data preprocessing, various descriptive statistics were obtained. Specifically, the first quartile (Q1) was found to be 0 kW, while the third quartile (Q3) was identified as 16037.25 kW. The subsequent computation of the IQR resulted in a value of 16037.25 kW, which, in turn, guided the determination of the Upper Bound and the Lower Bound at 40093.13 kW and -24055.88 kW, respectively.

4. Results and discussion

4.1. Hyperparameter of the compared models

The specific hyperparameters of the machine learning models were presented in Table 2 and Table 3 The ANN model consists of 2 Dense layers while CNN and LSTM use only 1 Dense layer. Additionally, CNN uses 1 convolutional layer and LSTM use 2 LSTM layer.
On the other hand, ELM's hyperparameters include:

Table 2: Layer configuration for ANN, CNN and LSTM

Hyperparameter	ANN	CNN	LSTM
Conv1D	-	100	-
MaxPooling	-	2	-
LSTM1	-	-	100
LSTM2	-	-	50
Dropout	0.2	0.1	0.15
Dense1	64	50	32
Dense2	32	-	-
Activation Function	ReLU	ReLU	ReLU

Table 3: Layer configuration for ELM

Hyperparameter	ELM
Hidden neurons	100
Alpha	0.7
rbf_width	0.3
Activation Function	Sigmoid

The number of hidden neurons, alpha - the mixing coefficient for distance and dot product input activations, and rbf_width - the multiplier for the radial basis activation function.
ANN, CNN and LSTM utilize the ReLU activation function while ELM uses the Sigmoid activation function.

4.2. Forecasting result in error metrics

This section presented a comparative analysis of four machine-learning algorithms for solar power forecasting: Artificial Neural Network (ANN), Convolutional Neural Network (CNN), Long Short-Term Memory (LSTM) and Extreme Learning Machine (ELM). The performance of these models was evaluated using two error metrics: Root Mean Squared Error (RMSE) and Normalized Root Mean Squared Error (N-RMSE). The N-RMSE was used to evaluate the overall performance of the models while RMSE was used to compare the performance between each model.

Table 4 summarized the error parameters of the machine-learning algorithms. Figures 7-12 show the predicted solar power for 1, 3, 6, 12, 24 and 48 step forecasting scenarios. Overall, using N-RMSE, it is noticeable that the performance of each model is relatively well, with excellent accuracy of all models in 1 and 3-step forecasting, and good accuracy of all models in 6, 12, 24 and 48-step forecasting. Among the 4 models evaluated, LSTM and ELM demonstrated better performance in terms of accuracy. Conversely, CNN and ANN models yielded results that were notably below expectations.

A close examination of Table 4 reveals that all four models had relatively small errors in terms of RMSE and N-RMSE. However, LSTM and ELM achieved better accuracy compared to ANN and CNN. For single-step forecasting, ELM had the lowest error values among all models, with its RMSE being 8.8 kW lower than that of LSTM. ANN and CNNperformance was found to be inferior by a small margin when compared to LSTM and ELM. The RMSE of ANN was 239.1 kW lower than the RMSE of CNN, thereby rendering the CNN model as the least effective model among the four evaluated models when considering single-step forecasting. Figure 7 illustrated the actual power and the predicted power produced by the machine-learning algorithms in single-step forecasting.

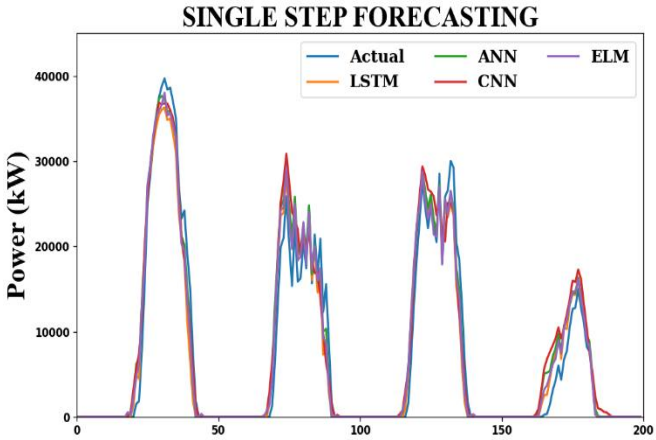

Figure 7: Actual power and predicted power of ML models in 1 step

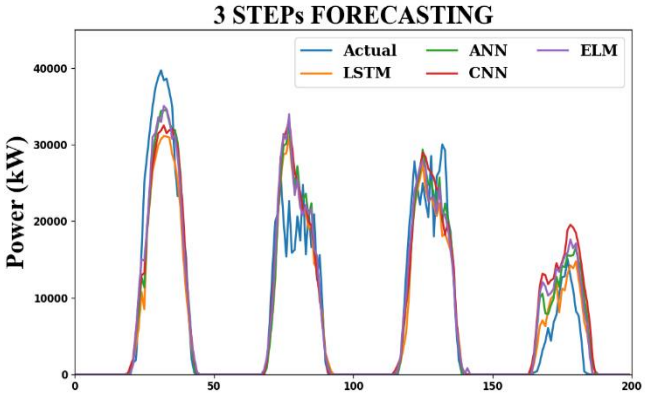

Figure 8: Actual power and predicted power of ML models in 3 steps

For multi-step forecasting with 3, 6, 12 and 24 steps ahead, the errors of all four models rose gradually, with LSTM overtook ELM in terms of accuracy, as ELM had higher RMSE than LSTM. The RMSE of LSTM were 45.6 kW, 137.6 kW, 108.9 kW and 65.1 kW lower than the RMSE of ELM for 3, 6, 12 and 24 step ahead, respectively. Despite small improvements, CNN persistently remained the least accurate model. However, it is noteworthy that the disparity in accuracy between ANN and CNN has been gradually diminishing with forecasting that has higher steps. Figure 8-11 illustrated the actual and forecasted power output using 4 machine learning methods in 3, 6, 12 and 24 steps ahead forecasting.

Finally, from 48 steps forecasting, the errors of all four models only increase by a small amount, with the ELM model surpassing the LSTM model and emerging as the most effective among the four forecasting models under consideration. The ELM model outperformed its closest competitor, LSTM, by just 7 kW in terms of RMSE. As evidenced by the data presented in Table 4, the CNN and ANN models continued to exhibit worse performance relative to the other models. The RMSE of CNN was only a 36.5 kW increase from the RMSE of ANN, making ANN the least accurate model when compared to the others model. Figure 12 provided a visual representation of the actual and predicted power output as forecasted by the different machine-learning methods in 48 steps forecasting.

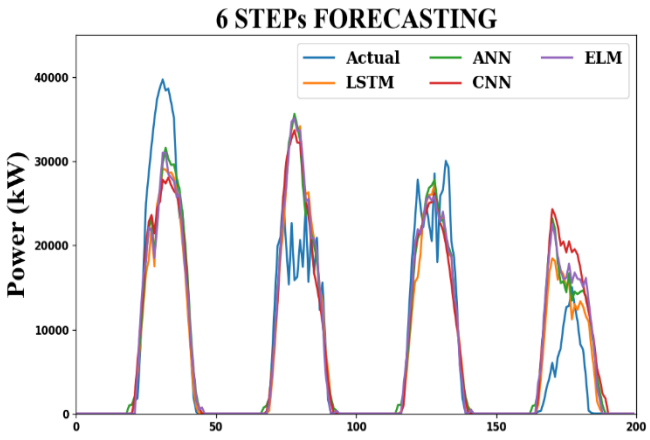

Figure 9: Actual power and predicted power of ML models in 6 steps

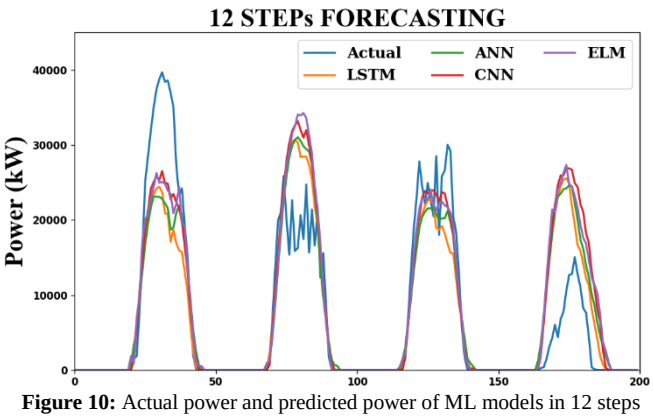

Figure 10: Actual power and predicted power of ML models in 12 steps

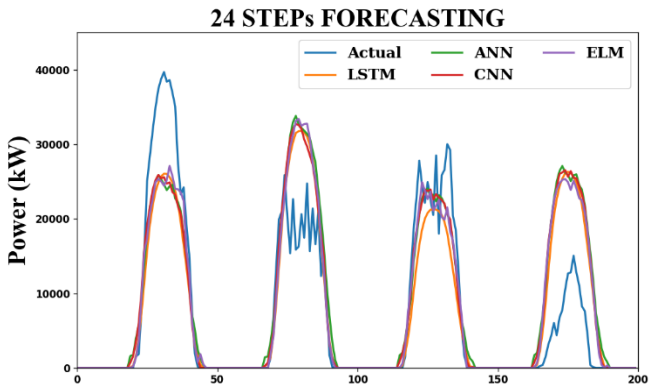

Figure 11: Actual power and predicted power of ML models in 24 steps

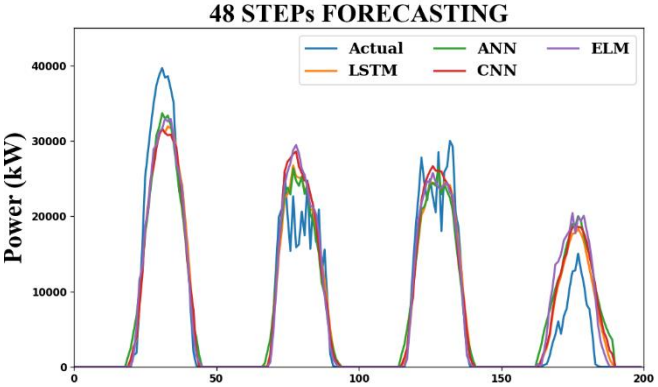

Figure 12: Actual power and predicted power of ML models in 48 steps

Based on the acquired findings, several targeted improvements can be implemented to augment the advantages for grid operators and stakeholders. In particular, the forecasting models developed for 1 and 3-step forecasting can be effectively employed to forecast solar power outputs, thereby facilitating more accurate management of solar farms. For forecasting involving higher steps, additional efforts will need to be directed toward enhancing the accuracy of the forecasting models. Consequently, grid operators will experience increased ease in efficiently administering and optimizing the power grid. Moreover, the results can assist shareholders of solar power plants in optimizing their revenues and profits by enabling them to participate in electricity markets, bid for contracts, and avoid financial losses for under or over-production of electricity.

4.3. Forecasting result in training and testing time

In addition to RMSE and n-RMSE, the training time and testing time of each model may be employed as metrics for comparative analysis. The training time denotes the duration required for model training, while the testing time represents the duration for a model to generate output.

As illustrated in Table 5, the LSTM model exhibits training and testing times of approximately 14 minutes in all step, and 5 minutes in all step, respectively.

These outcomes imply that the LSTM model demonstrates the lengthiest durations for both training and testing among the four models considered. The lengthy training period is one of the disadvantages of the LSTM model that has been mentioned in [17]. Conversely, the ELM model attains the shortest training time, reaching 0.09s at 1, 2, 4 and 48-step and 0.10s at 3,6 and 12-step. The model also has the shortest training time with the highest only being 0.78s at 48-step. The utilization of randomly generated weights in ELM serves to circumvent iterative learning processes and mitigates computational complexity. Furthermore, the training and testing times for the ANN model rank as the second lowest among the models, registering the highest recorded value of 1 minute and 26.82 seconds at 6-step, and 0.92 seconds at 6-step, respectively. Meanwhile, the CNN model follows the ANN model in terms of training and testing times, with the highest durations of 6 minutes and 57.78 seconds at 48-step, and 1.63 seconds at 24-step, respectively.

5. Conclusion.

Due to the unstable nature of solar power, forecasting of photovoltaic power output is essential for the operation of grid operators. In this paper, the accuracy of machine learning models including ANN, CNN, LSTM, and ELM was compared based on RMSE and N-RMSE errors combined with training time and testing time. All four machine learning models performed well, with minor differences in error rates. The data set had low variability, so any of the four methods yielded good results. However, applying these models to new data sets from other case studies would require readjusting and recalculating the hyperparameters, reevaluating the forecasting accuracy. To achieve better forecasting performance in future research, other techniques such as decomposition, hybrid models, or error correction should be considered.

Table 4: Evaluation of LSTM, CNN, ANN and ELM with error metrics in 1, 3, 6, 12, 24 and 48 steps

		1 step	3 steps	6 steps	12 steps	24 steps	48 steps
LSTM	**RMSE (kW)**	2671.1	3847.5	4397.0	4716.0	4781.5	4867.1
	N-RMSE (%)	6.5	9.4	10.7	11.5	11.7	11.9
CNN	**RMSE (kW)**	2930.5	4008.7	4605.0	4760.0	4851.9	4898.2
	N-RMSE (%)	7.1	9.8	11.2	11.6	11.8	11.9
ANN	**RMSE (kW)**	2698.6	3900.0	4515.3	4836.4	4894.8	4934.7
	N-RMSE (%)	6.6	9.5	11.0	11.8	11.9	12.0
ELM	**RMSE (kW)**	2662.3	3893.1	4534.6	4824.9	4846.6	4860.1
	N-RMSE (%)	6.5	9.5	11.0	11.8	11.8	11.8

Table 5: Evaluation of LSTM, CNN, ANN and ELM with training and testing time in 1, 3, 6, 12, 24 and 48 steps

		1 step	3 steps	6 steps	12 steps	24 steps	48 steps
LSTM	**Testing time**	00:05.24	00:04.90	00:05.86	00:05.19	00:05.19	00:04.81
	Training time	15:07.81	14:37.53	13:10.21	13:48.68	14:27.20	13:24.04
CNN	**Testing time**	00:01.40	00:00.79	00:01.12	00:00.68	00:01.63	00:01.19
	Training time	02:40.29	04:56.81	04:36.76	04:14.77	04:23.62	06:57.78
ANN	**Testing time**	00:00.64	00:00.58	00:00.92	00:00.60	00:00.52	00:00.67
	Training time	00:45.68	01:26.01	01:26.82	01:16.67	01:08.64	01:17.31
ELM	**Testing time**	00:00.09	00:00.10	00:00.10	00:00.10	00:00.09	00:00.09
	Training time	00:00.70	00:00.72	00:00.79	00:00.79	00:00.75	00:00.78

References

[1] Prime Minister of Vietnam, "Decision on mechanisms to promote the development of solar power projects in Viet Nam," Apr. 2020.

[2] P. Singla, M. Duhan, and S. Saroha, "A comprehensive review and analysis of solar forecasting techniques," *Front. Energy*, vol. 16, no. 2, pp. 187–223, Apr. 2022, doi: 10.1007/s11708-021-0722-7.

[3] D. C. Montgomery, C. L. Jennings, and M. Kulahci, *Introduction to time series analysis and forecasting*. John Wiley & Sons, 2015.

[4] K. Benmouiza and A. Cheknane, "Small-scale solar radiation forecasting using ARMA and nonlinear autoregressive neural network models," *Theor Appl Climatol*, vol. 124, no. 3–4, pp. 945–958, May 2016, doi: 10.1007/s00704-015-1469-z.

[5] J. Lu *et al.*, "Two-Tier Reactive Power and Voltage Control Strategy Based on ARMA Renewable Power Forecasting Models," *Energies*, vol. 10, no. 10, p. 1518, Oct. 2017, doi: 10.3390/en10101518.

[6] W. Wang, K. Chau, D. Xu, and X.-Y. Chen, "Improving Forecasting Accuracy of Annual Runoff Time Series Using ARIMA Based on EEMD Decomposition," *Water Resour Manage*, vol. 29, no. 8, pp. 2655–2675, Jun. 2015, doi: 10.1007/s11269-015-0962-6.

[7] M. Q. Raza, M. Nadarajah, and C. Ekanayake, "On recent advances in PV output power forecast," *Solar Energy*, vol. 136, pp. 125–144, Oct. 2016, doi: 10.1016/j.solener.2016.06.073.

[8] N. N. V. Nhat, D. N. Huu, and T. N. T. Hoai, "Evaluating the EEMD-LSTM model for short-term forecasting of industrial power load: A case study in Vietnam," *Int. J. Renew. Energy Dev.*, vol. 12, no. 5, pp. 881–890, Sep. 2023, doi: 10.14710/ijred.2023.55078.

[9] N. T. H. Thu, P. N. Van, and P. Q. Bao, "Multi-step Ahead Wind Speed Forecasting Based on a Bi-LSTM Network Combined with Decomposition Technique," in *Computational Intelligence Methods for Green Technology and Sustainable Development*, vol. 567, Y.-P. Huang, W.-J. Wang, H. A. Quoc, H.-G. Le, and H.-N. Quach, Eds., in Lecture Notes in Networks and Systems, vol. 567. , Cham: Springer International Publishing, 2023, pp. 569–580. doi: 10.1007/978-3-031-19694-2_50.

[10] Y. Huang, "Advances in Artificial Neural Networks – Methodological Development and Application," *Algorithms*, vol. 2, no. 3, pp. 973–1007, Aug. 2009, doi: 10.3390/algor2030973.

[11] M. M. Mijwil, "Artificial Neural Networks Advantages and Disadvantages," *Mesopotamian Journal of Big Data*, vol. 2021, pp. 29–31, Aug. 2021, doi: 10.58496/MJBD/2021/006.

[12] C. Wang and Z. Peng, "Design and Implementation of an Object Detection System Using Faster R-CNN," in *2019 International Conference on Robots & Intelligent System (ICRIS)*, Haikou, China: IEEE, Jun. 2019, pp. 204–206. doi: 10.1109/ICRIS.2019.00060.

[13] N. Jmour, S. Zayen, and A. Abdelkrim, "Convolutional neural networks for image classification," in *2018 International Conference on Advanced Systems and Electric Technologies (IC_ASET)*, Hammamet: IEEE, Mar. 2018, pp. 397–402. doi: 10.1109/ASET.2018.8379889.

[14] D. Wang, H. Yu, D. Wang, and G. Li, "Face Recognition System Based on CNN," in *2020 International Conference on Computer Information and Big Data Applications (CIBDA)*, Guiyang, China: IEEE, Apr. 2020, pp. 470–473. doi: 10.1109/CIBDA50819.2020.00111.

[15] L. Alzubaidi *et al.*, "Review of deep learning: concepts, CNN architectures, challenges, applications, future directions," *J Big Data*, vol. 8, no. 1, p. 53, Mar. 2021, doi: 10.1186/s40537-021-00444-8.

[16] H. Sak, A. Senior, and F. Beaufays, "Long Short-Term Memory Based Recurrent Neural Network Architectures for Large Vocabulary Speech Recognition," 2014, doi: 10.48550/ARXIV.1402.1128.

[17] G. Van Houdt, C. Mosquera, and G. Nápoles, "A review on the long short-term memory model," *Artif Intell Rev*, vol. 53, no. 8, pp. 5929–5955, Dec. 2020, doi: 10.1007/s10462-020-09838-1.

[18] A. K. Poddar and Dr. R. Rani, "Hybrid Architecture using CNN and LSTM for Image Captioning in Hindi Language," *Procedia Computer Science*, vol. 218, pp. 686–696, 2023, doi: 10.1016/j.procs.2023.01.049.

[19] S. Hochreiter and J. Schmidhuber, "Long Short-Term Memory," *Neural Computation*, vol. 9, no. 8, pp. 1735–1780, Nov. 1997, doi: 10.1162/neco.1997.9.8.1735.

[20] G.-B. Huang, Q.-Y. Zhu, and C.-K. Siew, "Extreme learning machine: Theory and applications," *Neurocomputing*, vol. 70, no. 1–3, pp. 489–501, Dec. 2006, doi: 10.1016/j.neucom.2005.12.126.

[21] F. Mercaldo, L. Brunese, F. Martinelli, A. Santone, and M. Cesarelli, "Experimenting with Extreme Learning Machine for Biomedical Image Classification," *Applied Sciences*, vol. 13, no. 14, p. 8558, Jul. 2023, doi: 10.3390/app13148558.

[22] N. C. Schwertman, M. A. Owens, and R. Adnan, "A simple more general boxplot method for identifying outliers," *Computational Statistics & Data Analysis*, vol. 47, no. 1, pp. 165–174, Aug. 2004, doi: 10.1016/j.csda.2003.10.012.

[23] M.-F. Li, X.-P. Tang, W. Wu, and H.-B. Liu, "General models for estimating daily global solar radiation for different solar radiation zones in mainland China," *Energy Conversion and Management*, vol. 70, pp. 139–148, Jun. 2013, doi: 10.1016/j.enconman.2013.03.004.

Vol 5 (1) (2024)

Measurement, Control, and Automation

Website: https:// mca-journal.org

ISSN 1859-0551

Lyapunov-based design of a model reference adaptive control for half-car active suspension systems

Le-Hoa Nguyen*, Huu-Lap-Truong Nguyen

The University of Danang - University of Science and Technology
**Corresponding author email: nlhoa@dut.udn.vn*

Abstract

This paper proposes a model reference adaptive control (MRAC) design for vehicle active suspension systems with unknown spring stiffness and damping coefficients with the aim of improving the performance of suspension systems. A mathematical model of a half-car active suspension system is first presented, then a reference model of a half-car suspension system that utilizes the skyhook damping concept is proposed. The control law and adaptation laws for the MRAC that guarantee the dynamic responses of the active suspension system follow well the dynamic responses of the reference model, were derived based on the Lyapunov stability criteria. To evaluate the advantages of the proposed reference model as well as the efficiency of the designed MRAC, the dynamic responses of the reference model, passive, and active suspension systems were analyzed and evaluated both in the frequency and time domains. The obtained results demonstrated that the active suspension system with MRAC provides a better performance in terms of the ride comfort and suspension deflection compared with the passive suspension system.

***Keywords**: Suspension system; half-car model; MRAC; Lyapunov stability.*

Symbols

Symbols	Units	Description
$\mathbf{A}_p$, $\mathbf{A}_m$, $\mathbf{B}_p$, $\mathbf{B}_m$, $\mathbf{C}_p$,		Space state matrix
$\mathbf{X}_p$, $\mathbf{X}_m$		State vector
m_p, m_m	kg	Vehicle body mass
I_p, I_m	kg.m^2	Moment inertia
l_f, l_r	m	Distance from front/rear wheel to the center of gravity
k_{fp}, k_{fm}	N/m	Spring stiffness of front/rear suspension
c_{fp}, c_{fm}	N.s/m	Damping coefficient of front/rear suspension
c_{sky}	N.s/m	Skyhook damping coefficient

Abbreviations

MRAC	Model reference adaptive control

1. Introduction

Suspension system is a crucial part of vehicle, its main functions include: 1) to isolate the vehicle chassis from road disturbances (ride comfort) and 2) to keep the tire in contact with the road surface and to support the vehicle's static weight (road holding) [1]. To improve the ride comfort, it is important to attenuate vertical vibrations in the human sensitive frequency range 4 -8 Hz [2, 3] and around the natural frequency of the vehicle body (usually ~ 1.5 Hz) [4, 5]. The ride comfort is usually quantitatively evaluated by the vertical acceleration of the vehicle body. Road holding is related to the abilities of cornering, braking, and traction during maneuver of the vehicle. These abilities depend on the contact forces between the road surface and the vehicle tire [6, 7]. Therefore, to improve the road holding, it is necessary to minimize the tire deflection and suspension deflection variations induced by road irregularities, especially around the resonance frequency of the unsprung mass (~ 10 Hz) [1, 8]. However, ride comfort and road holding are conflicting performance indexes in suspension system control and design [4, 6, 8].

Based on the ability of to be controlled, suspension systems are classified into three categories: passive suspension, semi-active suspension, and active suspension. A passive suspension system consists of fixed-stiffness spring and non-adjustable damper, therefore, it is difficult to achieve a desired performance simultaneously of ride comfort and road holding [9]. Semi-active suspension systems are equipped with adjustable dampers that can provide performance compared with the passive system. However, control forces generated by adjustable dampers depend on the velocity of suspension deflection [6, 8, 10, 11]. In contrast to the passive and semi-active suspension systems, active suspension systems use external (hydraulic, electromagnetic or pneumatic) power actuators to generate independent forces on the suspension system [12]. Consequently, the active suspension system is the most effective way to improve the vehicle suspension performance and various active suspension control techniques have been

Received: 13 August 2023; Accepted: 06 February 2024.

proposed over the past decades [3, 6, 7, 13-22]. In terms of the ride comfort improvement, Erik et al. proposed to use a model predictive control to compensate the influence of actuator limitations on the ride comfort [13]. To enhance the ride comfort in the human sensitive frequency range (4-8 Hz), the H-infinity control technique that aims to minimize H-infinity norm in specific frequency band was introduced by Sun et al. [3]. A comparative study of different model-based control laws for the active quarter car suspension system such as first-order sliding mode control, high-order sliding mode control, integral sliding mode control, PID control, and linear quadratic regulator control was conducted by Shahid and Wei [14]. To overcome the conflict between ride comfort and road holding, a number of control techniques have been presented such as hybrid fuzzy logic control [6], robust-based H-infinity and mu-synthesis control [15], predictive control based on particle swarm optimization algorithm [16], model reference adaptive control for the quarter car model [17-19], optimal control with exponential decay rate [20], etc.

In practical vehicle systems, the performance of suspension system will be degraded by the variations in the system's parameters. For example, changes in suspension damping coefficient that leads to significantly changes in the ride comfort and road holding indexes [21]. However, the control techniques mentioned above cannot guarantee a desired suspension performance under the parameter uncertainties. To address this issue, adaptive control techniques are the most suitable choice. In [22], the authors proposed an adaptive control design for active quarter suspension system, in which the nonlinear spring stiffness and piece-wise damper dynamics are assumed to be unknown. A constrained adaptive backstepping control scheme for the quarter car active suspension model was presented in [23], where the sprung mass is considered as an uncertain parameter. Model reference adaptive control (MRAC) technique has been proposed in many previous studies to control active suspension systems [17-19]. In the work of Sunwoo et al. [17], MRAC technqique was designed to control the quarter car active suspension model where the sprung mass, suspension spring stiffness and suspension damping coefficient were assumed to be unknown. The obtained results show a significant improvement in term of the ride comfort of the proposed active suspension system to compared with the passive system. A variable structure MRAC was also proposed by Mohammadi [18] to control a quarter car active suspension system. In this work, two skyhook dampers were designed for both the sprung mass and unsprung mass of the reference model in order to achive an improvement in ride comfort and rattle suspension space. To deal with non ideal actuator, a tube-based MRAC approach agumented by a disturbance observer was developed by Mousavi et al. [19] for a quarter car active suspension system. However, the MRAC methods mentioned above are restricted on the quarter car model where pitch motion of the vehicle as well as the delay in road disturbance between the front and rear wheels cannot be evaluated.

In this paper, we proposed a MRAC scheme for the half-car active suspension system with fully unknown in spring stiffness and damping coefficients of both front and rear suspensions is proposed. A skyhook damping concept originally proposed by Karnopp et al. [24] is used to develop the reference model of a half-car active suspension. An adaptation scheme based on Lyapunov stability criteria is developed to guarantee that the dynamic responses of the active suspension system follow asymptotically the dynamic responses of the reference suspension system. Performance of the active suspension system (as well as the reference suspension system) are analyzed and compared with the passive suspension system in both the frequency domain and the time domain. This study contributes the literature as follows:

- A conceptual reference model for the half-car suspension system. The performance of the proposed reference model has been proven to be much better than that of the passive model through the dynamic response analysis in both the time and frequency domains.
- An efficient MRAC scheme for the half-car active suspension system. To our best knowledge, no previous studies have applied MRAC to the half-car suspension model. The proposed method can accommodate large variations in the spring stiffness and damping coefficients of the suspension system and the simulation results show significant improvements over the passive suspension system.

2. Mathematical modelling

2.1. Model of a half-car active suspension

In this current study, to simply the control problem under investation, the following assumptions are applied:

- The nonlinear dynamics such as nonlinear characteristics of stiffness and damping are ignored.
- The actuator dynamic is not discussed, actuator saturation is also ignored.
- All state variables are accessable.

Based on the above assumptions, a half-car active suspension model is depicted in Figure 1.

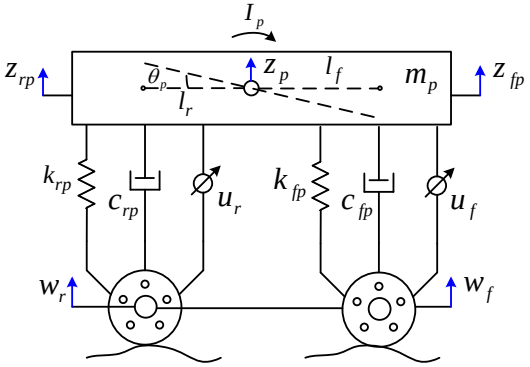

Figure 1: The half-car active suspension model.

The parameters involved include: the mass of vehicle body is m_p, the mass moment of inertia for the vehicle body is I_p, the spring stiffness of the front/rear suspensions are k_{fp} and k_{rp}, respectively, the damping coefficients of the front/rear suspensions are c_{fp} and c_{rp}, respectively, the distances of the front/rear suspension location, with reference to the center of gravity of the vehicle body are l_f and l_r, respectively. Let z_{fp} and z_{rp} be the vertical displacements of the vehicle body at the front/rear suspension locations, respectively. Let w_f and w_r are the vertical displacements of the front/rear wheels,

respectively. The vertical displacement and the rotary angle of the vehicle body at the center of gravity are denoted as z_p and θ_p, respectively.

The equations of motion for the vehicle body are given by

$$\begin{aligned} m_p\ddot{z}_p &= -k_{rp}\left(z_{rp}-w_r\right)-c_{rp}\left(\dot{z}_{rp}-\dot{w}_r\right)+u_r \\ &\quad -k_{fp}\left(z_{fp}-w_f\right)-c_{fp}\left(\dot{z}_{fp}-\dot{w}_f\right)+u_f, \end{aligned} \tag{1}$$

$$\begin{aligned} I_p\ddot{\theta}_p &= -\left[k_{rp}\left(z_{rp}-w_r\right)+c_{rp}\left(\dot{z}_{rp}-\dot{w}_r\right)-u_r\right]l_r \\ &\quad +\left[k_{fp}\left(z_{fp}-w_f\right)+c_{fp}\left(\dot{z}_{fp}-\dot{w}_f\right)-u_f\right]l_f. \end{aligned} \tag{2}$$

and the constraints are as follows

$$z_{rp} = z_p + l_r\theta_p, \tag{3}$$

$$z_{fp} = z_p - l_f\theta_p. \tag{4}$$

where u_r and u_f are the control force exerted by controllable actuators at the front/rear suspensions, respectively. In this paper, it is assumed that the exact values of these parameters k_{fp}, k_{rp}, c_{fp}, and c_{rp} are unknown. It is also assumed that there is no limitation on exerting the control forces of the actuators. By defining state variables as $x_{1p}=z_{rp}-w_r$, $x_{2p}=z_{fp}-w_f$, $x_{3p}=\dot{z}_p$, and $x_{4p}=\dot{\theta}_p$, the equations of motion (1)-(2) can be expressed in the state space equation as follows

$$\dot{\mathbf{X}}_p = \mathbf{A}_p\mathbf{X}_p + \mathbf{B}_p\mathbf{v} + \mathbf{C}_p\mathbf{u}, \tag{5}$$

where $\mathbf{v}=\begin{bmatrix}\dot{w}_r & \dot{w}_f\end{bmatrix}^T$, $\mathbf{u}=\begin{bmatrix}u_r & u_f\end{bmatrix}^T$, and the matrices $\mathbf{A}_p$, $\mathbf{B}_p$, and $\mathbf{C}_p$ are obtained as follows:

$$\mathbf{A}_p = \begin{bmatrix} 0 & 0 & 1 & l_r \\ 0 & 0 & 1 & -l_f \\ -\frac{k_{rp}}{m_p} & -\frac{k_{fp}}{m_p} & -\frac{c_{rp}+c_{fp}}{m_p} & \frac{c_{fp}l_f-c_{rp}l_r}{m_p} \\ -\frac{k_{rp}l_r}{I_p} & \frac{k_{fp}l_f}{I_p} & \frac{c_{fp}l_f-c_{rp}l_r}{I_p} & -\frac{c_{rp}l_r^2+c_{fp}l_f^2}{I_p} \end{bmatrix},$$

$$\mathbf{B}_p = \begin{bmatrix} -1 & 0 \\ 0 & -1 \\ \frac{c_{rp}}{m_p} & \frac{c_{fp}}{m_p} \\ \frac{c_{rp}l_r}{I_p} & -\frac{c_{fp}l_f}{I_p} \end{bmatrix}, \quad \mathbf{C}_p = \begin{bmatrix} 0 & 0 \\ 0 & 0 \\ \frac{1}{m_p} & \frac{1}{m_p} \\ \frac{l_r}{I_p} & -\frac{l_f}{I_p} \end{bmatrix}.$$

2.2. Proposed reference model of a half-car suspension system

In order to specify the desired performance of ride quality of the suspension system, a skyhook damping system was chosen as the reference model. A skyhook damping model was originally introduced by Karnopp et al. [24]. In this work, to suppress the vibrations of the vehicle body against road disturbances, an inertial damper is connected between the vehicle body and the stationary sky. Based on this concept, a skyhook damping model for a half-car suspension system is proposed in Figure 2.

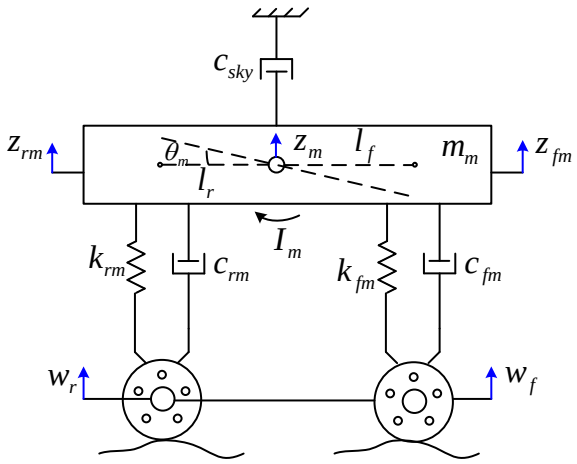

Figure 2: The proposed reference half-car model.

The system's parameters include: the spring stiffness of the front and rear suspensions k_{fm} and k_{rm}, respectively, the damping coefficients of the front and rear suspensions c_{rm} and c_{fm}, respectively, the skyhook damping coefficient c_{sky}, the mass moment of inertia for the vehicle body I_m, and the mass of the vehicle body m_m.

The equations of motion for this model are given by

$$\begin{aligned} m_m\ddot{z}_m &= -k_{rm}\left(z_{rm}-w_r\right)-c_{rm}\left(\dot{z}_{rm}-\dot{w}_r\right) \\ &\quad -k_{fm}\left(z_{fm}-w_f\right)-c_{fm}\left(\dot{z}_{fm}-\dot{w}_f\right)-c_{sky}\dot{z}_m, \end{aligned} \tag{6}$$

$$\begin{aligned} I_m\ddot{\theta}_m &= -\left[k_{rm}\left(z_{rm}-w_r\right)+c_{rm}\left(\dot{z}_{rm}-\dot{w}_r\right)\right]l_r \\ &\quad +\left[k_{fm}\left(z_{fm}-w_f\right)+c_{fm}\left(\dot{z}_{fm}-\dot{w}_f\right)\right]l_f. \end{aligned} \tag{7}$$

and the constraints are

$$z_{rm} = z_m + l_r\theta_m, \tag{8}$$

$$z_{fm} = z_m - l_f\theta_m. \tag{9}$$

As before, we also define the state variables as $x_{1m}=z_{rm}-w_r$, $x_{2m}=z_{fm}-w_f$, $x_{3m}=\dot{z}_m$, and $x_{4m}=\dot{\theta}_m$, the state space equation is obtained as follows:

$$\dot{\mathbf{X}}_m = \mathbf{A}_m\mathbf{X}_m + \mathbf{B}_m\mathbf{v}, \tag{10}$$

where the matrices $\mathbf{A}_m$ and $\mathbf{B}_m$ are given by

$$\mathbf{A}_m = \begin{bmatrix} 0 & 0 & 1 & l_r \\ 0 & 0 & 1 & -l_f \\ -\frac{k_{rm}}{m_m} & -\frac{k_{fm}}{m_m} & -\frac{c_{sky}+c_{rm}+c_{fm}}{m_m} & \frac{c_{fm}l_f-c_{rm}l_r}{m_m} \\ -\frac{k_{rm}l_r}{I_m} & \frac{k_{fm}l_f}{I_m} & \frac{c_{fm}l_f-c_{rm}l_r}{I_m} & -\frac{c_{fm}l_f^2+c_{rm}l_r^2}{I_m} \end{bmatrix},$$

$$\mathbf{B}_m = \begin{bmatrix} -1 & 0 \\ 0 & -1 \\ \frac{c_{rm}}{m_m} & \frac{c_{fm}}{m_m} \\ \frac{c_{rm}l_r}{I_m} & -\frac{c_{fm}l_f}{I_m} \end{bmatrix}.$$

3. Design of an MRAC controller

The goal of the controller is to bring the state variables of the active suspension system (plant) $\mathbf{X}_p$ described by (5) asymptotically approach the corresponding state variables of the reference system $\mathbf{X}_m$ described by (10) in a short time. In order to achieve that goal, an MRAC method was used. In MRAC algorithm, the controller's parameters are adjusted based on the error between the desired responses of the reference model $\mathbf{X}_m$ and that obtained by the plant model $\mathbf{X}_p$. To ensure the controller's parameters converge to the ideal values that cause the plant's responses to match the responses of the reference model, a Lyapunov stability method was used. In this paper, all state variables as well as the vertical velocities of the wheels are assumed to be accessible.

3.1. Dynamics of error

Let choose the control law as follows:

$$\mathbf{u} = \mathbf{K}_x \mathbf{X}_p + \mathbf{K}_v \mathbf{v}, \tag{11}$$

where $\mathbf{K}_x$ and $\mathbf{K}_v$ are adjustable gain matrices. They are specified as matrices of size (2x4) and (2x2), respectively.
Substituting (11) into (5) yields

$$\dot{\mathbf{X}}_p = \left(\mathbf{A}_p + \mathbf{C}_p \mathbf{K}_x\right)\mathbf{X}_p + \left(\mathbf{B}_p + \mathbf{C}_p \mathbf{K}_v\right)\mathbf{v}. \tag{12}$$

It is obvious that, there would be exist a set of unknown constant gains $\mathbf{K}_x^*$ and $\mathbf{K}_v^*$ such that

$$\mathbf{A}_p + \mathbf{C}_p \mathbf{K}_x^* = \mathbf{A}_m, \tag{13}$$

$$\mathbf{B}_p + \mathbf{C}_p \mathbf{K}_v^* = \mathbf{B}_m. \tag{14}$$

Define the error between the states of the plant model and that of the reference model as

$$\mathbf{e} = \mathbf{X}_p - \mathbf{X}_m. \tag{15}$$

By considering (10) and (12), the dynamics of error yields

$$\dot{\mathbf{e}} = \mathbf{A}_m \mathbf{e} + \left(\mathbf{A}_p - \mathbf{A}_m\right)\mathbf{X}_p + \left(\mathbf{B}_p - \mathbf{B}_m\right)\mathbf{v} + \mathbf{C}_p \mathbf{u}. \tag{16}$$

Using (11), (13), and (14), the dynamics of error is rewritten as follows

$$\dot{\mathbf{e}} = \mathbf{A}_m \mathbf{e} + \mathbf{C}_p \boldsymbol{\Psi} \mathbf{X}_p + \mathbf{C}_p \boldsymbol{\Phi} \mathbf{v}. \tag{17}$$

where $\boldsymbol{\Psi}$ and $\boldsymbol{\Phi}$ are defined as: $\boldsymbol{\Psi} = \mathbf{K}_x - \mathbf{K}_x^*$ and $\boldsymbol{\Phi} = \mathbf{K}_v - \mathbf{K}_v^*$. They are unknown but adjustable gain error matrices.

3.2. Lyapunov stability and adaptation laws

In order to derive parameter adjustment laws, we introduce a Lyapunov function as follows:

$$V = \mathbf{e}^T \mathbf{P} \mathbf{e} + \mathrm{tr}\left(\boldsymbol{\Psi} \mathbf{G}_1^{-1} \boldsymbol{\Psi}^T\right) + \mathrm{tr}\left(\boldsymbol{\Phi} \mathbf{G}_2^{-1} \boldsymbol{\Phi}^T\right) \geq 0, \tag{18}$$

where $\mathrm{tr}(\cdot)$ is the trace of matrix operation, $\mathbf{G}_1$ and $\mathbf{G}_2$ are the adaptation gain matrices of size (4x4) and (2x2), respectively. They are asymmetric and positive definite. Derivative of V along the error, we have

$$\dot{V} = \dot{\mathbf{e}}^T \mathbf{P} \mathbf{e} + \mathbf{e}^T \mathbf{P} \dot{\mathbf{e}} + 2\mathrm{tr}\left(\boldsymbol{\Psi} \mathbf{G}_1^{-1} \dot{\boldsymbol{\Psi}}^T\right) + 2\mathrm{tr}\left(\boldsymbol{\Phi} \mathbf{G}_2^{-1} \dot{\boldsymbol{\Phi}}^T\right). \tag{19}$$

Substituting (17) into (19), yields

$$\begin{aligned} \dot{V} = {} & \mathbf{e}^T \left(\mathbf{A}_m^T \mathbf{P} + \mathbf{P} \mathbf{A}_m\right)\mathbf{e} + 2\mathbf{e}^T \mathbf{P} \mathbf{C}_p \boldsymbol{\Psi} \mathbf{X}_p \\ & + 2\mathbf{e}^T \mathbf{P} \mathbf{C}_p \boldsymbol{\Phi} \mathbf{v} + 2\mathrm{tr}\left(\boldsymbol{\Psi} \mathbf{G}_1^{-1} \dot{\boldsymbol{\Psi}}^T\right) + 2\mathrm{tr}\left(\boldsymbol{\Phi} \mathbf{G}_2^{-1} \dot{\boldsymbol{\Phi}}^T\right). \end{aligned} \tag{20}$$

Let choose $\mathbf{P}$ as an asymmetric, positive definite matrix and a unique solution of the following equation

$$\mathbf{A}_m^T \mathbf{P} + \mathbf{P} \mathbf{A}_m = -\mathbf{Q}, \tag{21}$$

where $\mathbf{Q}$ is a symmetric, positive definite matrix, and to be specified by the user.
Substituting (21) into (20), we obtained

$$\begin{aligned} \dot{V} = {} & -\mathbf{e}^T \mathbf{Q} \mathbf{e} + 2\mathbf{e}^T \mathbf{P} \mathbf{C}_p \boldsymbol{\Psi} \mathbf{X}_p + 2\mathbf{e}^T \mathbf{P} \mathbf{C}_p \boldsymbol{\Phi} \mathbf{v} \\ & + 2\mathrm{tr}\left(\boldsymbol{\Psi} \mathbf{G}_1^{-1} \dot{\boldsymbol{\Psi}}^T\right) + 2\mathrm{tr}\left(\boldsymbol{\Phi} \mathbf{G}_2^{-1} \dot{\boldsymbol{\Phi}}^T\right). \end{aligned} \tag{22}$$

If we choose $\boldsymbol{\Psi}$ and $\boldsymbol{\Phi}$ such that

$$\dot{\boldsymbol{\Psi}} = -\mathbf{C}_p^T \mathbf{P} \mathbf{e} \mathbf{X}_p^T \mathbf{G}_1, \tag{23}$$

$$\dot{\boldsymbol{\Phi}} = -\mathbf{C}_p^T \mathbf{P} \mathbf{e} \mathbf{v}^T \mathbf{G}_2, \tag{24}$$

then, we have

$$\begin{aligned} 2\mathrm{tr}\left(\boldsymbol{\Psi} \mathbf{G}_1^{-1} \dot{\boldsymbol{\Psi}}^T\right) &= -2\mathrm{tr}\left(\boldsymbol{\Psi} \mathbf{G}_1^{-1} \mathbf{G}_1 \mathbf{X}_p \mathbf{e}^T \mathbf{P} \mathbf{C}_p\right) = -2\mathrm{tr}\left(\boldsymbol{\Psi} \mathbf{X}_p \mathbf{e}^T \mathbf{P} \mathbf{C}_p\right) \\ &= -2\mathrm{tr}\left(\mathbf{e}^T \mathbf{P} \mathbf{C}_p \boldsymbol{\Psi} \mathbf{X}_p\right) = -2\mathbf{e}^T \mathbf{P} \mathbf{C}_p \boldsymbol{\Psi} \mathbf{X}_p. \end{aligned} \tag{25}$$

Similarly, we can write

$$2\mathrm{tr}\left(\boldsymbol{\Phi} \mathbf{G}_2^{-1} \dot{\boldsymbol{\Phi}}^T\right) = -2\mathbf{e}^T \mathbf{P} \mathbf{C}_p \boldsymbol{\Phi} \mathbf{v}. \tag{26}$$

Substituting (25) and (26) into (22), finally, we obtain

$$\dot{V} = -\mathbf{e}^T \mathbf{Q} \mathbf{e} < 0. \tag{27}$$

By the Lyapunov stability theorem [25], conditions (18) and (27) ensure that the state error $\mathbf{e}$, and parameter gain error matrices $\boldsymbol{\Psi}$, $\boldsymbol{\Phi}$ are stable in the sense of Lyapunov. Furthermore, if we choose the matrices $\mathbf{P}$ and $\mathbf{Q}$ as strictly positive definite matrices, then $\mathbf{e}$, $\boldsymbol{\Psi}$, and $\boldsymbol{\Phi}$ will converge asymptotically to zero.
Finally, it is noted that $\dot{\boldsymbol{\Psi}} = \dot{\mathbf{K}}_x$ and $\dot{\boldsymbol{\Phi}} = \dot{\mathbf{K}}_v$, the parameter adjustment laws are obtained as follows:

$$\dot{\mathbf{K}}_x = -\mathbf{C}_p^T \mathbf{P} \mathbf{e} \mathbf{X}_p^T \mathbf{G}_1, \tag{28}$$

$$\dot{\mathbf{K}}_v = -\mathbf{C}_p^T \mathbf{P} \mathbf{e} \mathbf{v}^T \mathbf{G}_2. \tag{29}$$

The controlled system scheme is depicted in Figure 3.

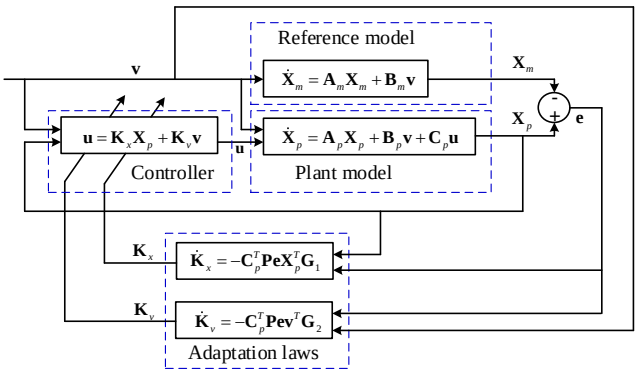

Figure 3: The MRAC scheme of active suspension system.

4. Results and discussions

We will first analyse the performance of the proposed reference system based on the comparison with the performance of the passive suspension system. Note that the half-car passive suspension model can be obtained from (4) by setting control signals $u = 0$. The frequency-domain analysis was performed to investigate the dynamic responses of both the reference and passive models, where the parameters of these two models are given in Table 1. The parameters of the passive system are

assumed to be unknown in practice. For simulation, we may select $m_p = m_m$, $I_p = I_m$, $l_{rp} = I_{rm} = l_r$, $l_{fp} = I_{fm} = l_f$, the spring stiffness (k_{fp}, k_{rp}) and the damping coefficients (c_{fp}, c_{rp}) of the front/rear suspension of the passive system are varied up to 30% from these parameters of the reference system, as shown in Table 1. In the following simulations, we consider 6 cases of these parameters of the passive system as follows:

- Case 1: $c_{rp} = c_{rm}$, $c_{fp} = c_{fm}$, $k_{rp} = k_{rm}$, $k_{fp} = k_{fm}$,
- Case 2: $c_{rp} = c_{rm} + 0.3c_{rm}$, $c_{fp} = c_{fm} + 0.3c_{fm}$,
- Case 3: $c_{rp} = c_{rm} - 0.3c_{rm}$, $c_{fp} = c_{fm} - 0.3c_{fm}$,
- Case 4: $k_{rp} = k_{rm} + 0.3k_{rm}$; $k_{fp} = k_{fm} + 0.3k_{fm}$,
- Case 5: $k_{rp} = k_{rm} - 0.3k_{rm}$; $k_{fp} = k_{fm} - 0.3k_{fm}$,
- Case 6: $k_{rp} = k_{rm} + 0.3k_{rm}$, $c_{rp} = c_{rm} - 0.3c_{rm}$.

Table 1: Parameter values of the reference and the passive/active suspension systems

Description	Units	Values	
		Reference model	Passive/active model
Vehicle body mass	kg	$m_m = 850$	$m_p = 850$
Moment inertia of the vehicle body	kg.m^2	$I_m = 1250$	$I_p = 1250$
Distance between the center of gravity and the front suspension	m	$l_f = 1.18$	$l_f = 1.18$
Distance between the center of gravity and the rear suspension	m	$l_r = 1.56$	$l_r = 1.56$
Spring stiffness of the front suspension	N/m	$k_{fm} = 25000$	$k_{fp} = k_{fm} \pm 0.3k_{fm}$
Spring stiffness of the rear suspension	N/m	$k_{rm} = 28000$	$k_{rp} = k_{rm} \pm 0.3k_{rm}$
Damping coefficient of the front suspension	N.s/m	$c_{fm} = 1750$	$c_{fp} = c_{fm} \pm 0.3c_{fm}$
Damping coefficient of the rear suspension	N.s/m	$c_{rm} = 1550$	$c_{rp} = c_{rm} \pm 0.3c_{rm}$
Skyhook damping coefficient	N.s/m	$c_{sky} = 4000$	

Except for the parameters mentioned above, the remaining parameters of the passive system are chosen to be the same as those of the reference system.

The frequency responses of the vehicle body vertical acceleration ($\ddot{z}$) with respect to the derivative of vertical displacements of the front wheel ($\dot{w}_f$) and the rear wheel ($\dot{w}_r$) are shown in Figure 4(a) and Figure 4(b), respectively. It can be seen from Figure 4 that the magnitude of the vehicle body vertical acceleration of the reference system (solid line) is smaller than that of all passive systems (dotted lines) over a large frequency range, especially around the nature frequency of the vehicle body (~ 1.5 Hz) and in the human sensitive frequency range (4-8 Hz) [2]. This also means that the reference system exhibits better ride comfort compared with all passive systems.

Figure 5 shows the frequency responses of the suspension deflection ($z - w$) with respect to the derivative of vertical displacements of the wheel ($\dot{w}$) for the reference system (solid line) and all passive systems (dotted lines). The figures show that the reference system provides a smaller magnitude of the suspension deflection around the natural frequency of the vehicle body ((~ 1.5 Hz) than that of passive systems. In the high frequency region (above 2 Hz), the reference system is observed to have the same magnitude of suspension deflection as passive systems. However, this magnitude is larger than that of passive systems in the low frequency region (below 0.8 Hz).

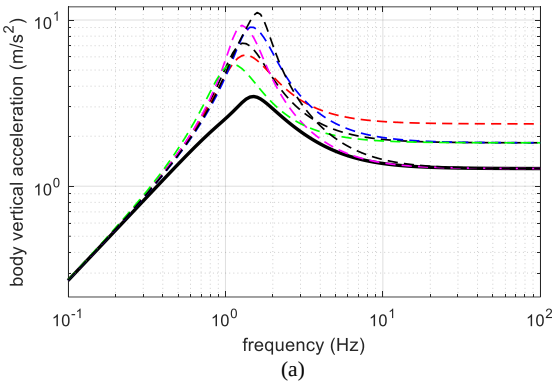

(a)

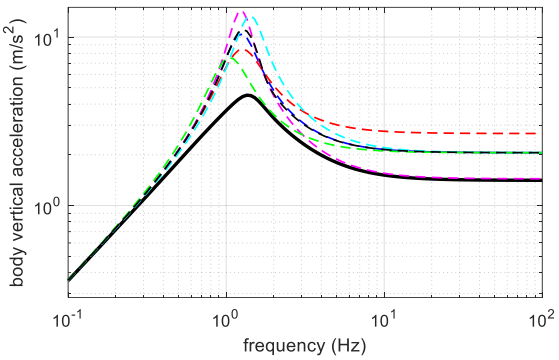

(b)

Figure 4: Frequency responses of vehicle body vertical acceleration with respect to the derivative of vertical displacement of a) front wheel, and b) rear wheel (solid line - reference system, dotted lines – passive system).

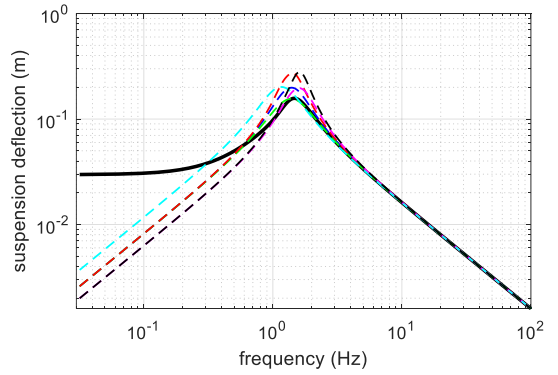

(a)

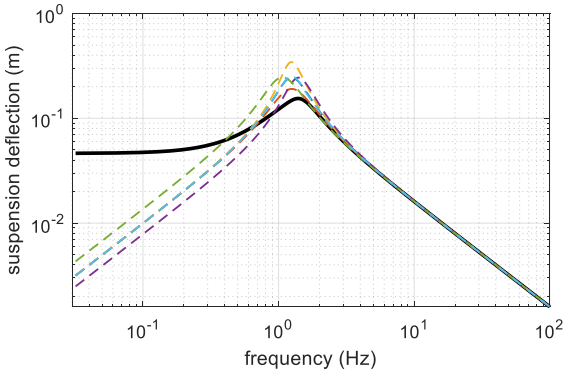

(b)

Figure 5: Frequency responses of suspension deflections at a) the front wheel and b) the rear wheel with respect to the derivative of vertical displacement of the front wheel and rear wheel, respectively, (solid line - reference system, dotted lines – passive system).

Next, the effectiveness of the proposed MRAC scheme for the active suspension system will be examined. To verify the adaptability and robustness of the control system, many different cases that correspond to the variations in the spring stiffness and damping coefficients (Case 1 to Case 6 as mentioned above) of the active system were simulated.

In this simulation, a variable road profile following ISO-2361 was used [26], as follows:

$$\dot{w}(t) + 2\pi v n_0 w(t) = \sqrt{G_q(\Omega_0)}v\delta(t), \quad (30)$$

where v is a constant vehilce velocity, n_0 is the reference spatial frequency defined as $n_0 = 0.1$ (cycle/m), $G_q(\Omega_0)$ is the coefficient of road roughness, and $\delta(t)$ is a time-domain white noise. When the vehicle travels at a speed v = 20 m/s under a grade-poor road ($G_q(\Omega_0) = 256\times10^{-6} m^3$), the time series of the road disturbance is depicted as in Figure 6.

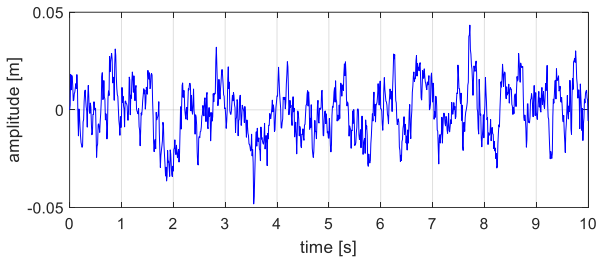

Figure 6: Time course of a grade-poor road.

Since the distance between the front wheel and the rear wheel is $l_f + l_r = 2.74$ m, therefore, a time delay of 0.137 seconds was applied to the rear wheel disturbance (i.e., $w_r(t) = w_f(t - 0.137)$.

The obtained results show that the trajectory of the active system follows well the trajectory of the reference one. To analyze in more detail, the simulation results for Case 2 (i.e., both damping coefficients of the front and the rear suspension of the active system were increased up to 30% from the nominal values of the reference system) are shown in Figure 7 to Figure 12.

To make sure the convergence of the active suspension's responses to that of the passive suspension system based on the control scheme depicted in Figure 3, the matrices **Q**, **P**, $\mathbf{G}_1$, $\mathbf{G}_2$ must be chosen properly (some trail and error is needed). In this simulation, we first chose **Q** as the identity matrix (i.e., $\mathbf{Q} = \mathbf{I}_4$). Solving the Lyapunov equation (21), we obtain

$\mathbf{P}$ = [1.931 -0.1715 0.0117 0.005; -0.1715 2.2936 0.0049 -0.0128;
0.0117 0.0049 0.0603 -0.0037; 0.005 -0.0128 -0.0037 0.1056]

Then, after some efforts, the values of matrices $\mathbf{G}_1$ and $\mathbf{G}_2$ are selected as

$$\mathbf{G}_1 = 10^6 \times [200\ 10\ 5\ 1;\ 10\ 50\ 6\ 7;\ 5\ 6\ 60\ 10;\ 1\ 7\ 10\ 70],$$

$$\mathbf{G}_2 = 5\times10^4 \times [5\ \ 1;\ 1\ \ 10].$$

Figure 7 shows the errors between states of the active system and the reference model. It is clear that the active suspension system incorporated with MRAC follows well the dynamic response of the reference model. The convergence of the adaptation gains $\mathbf{K}_x$ and $\mathbf{K}_v$ is presented in Figure 8 and Figure 9, respectively.

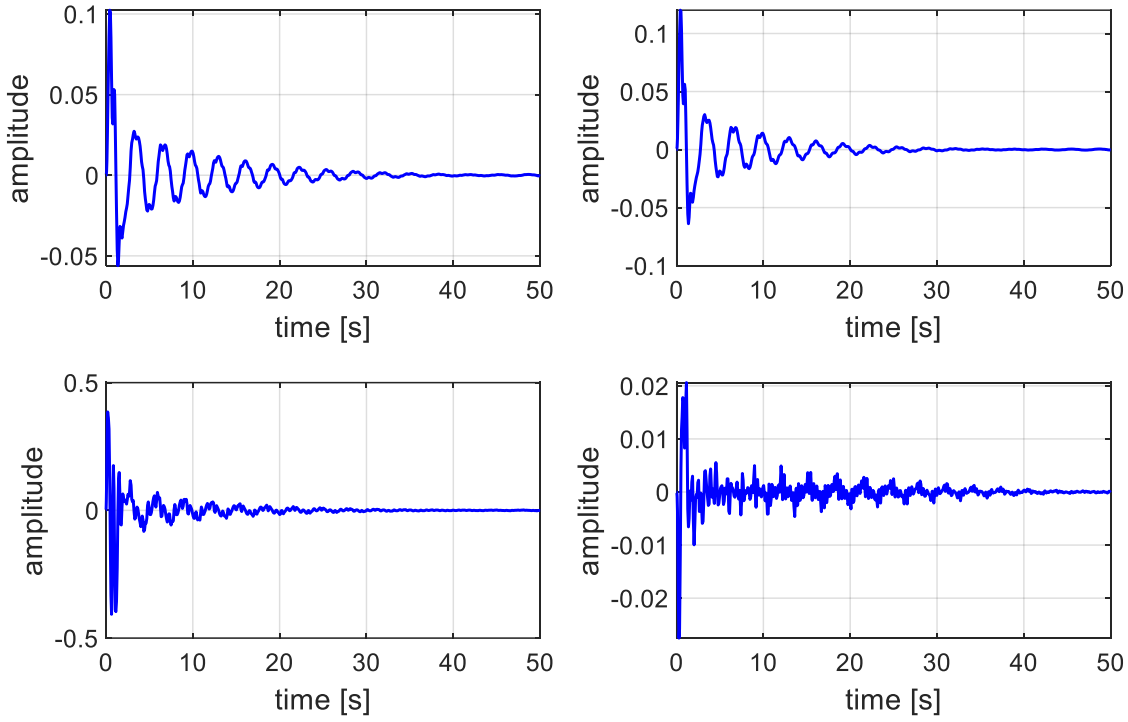

Figure 7: State errors between the reference model and the active system

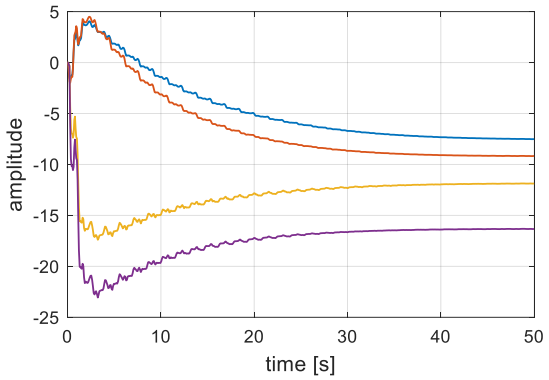

Figure 8: Convergence of the controller gains, $\mathbf{K}_v$.

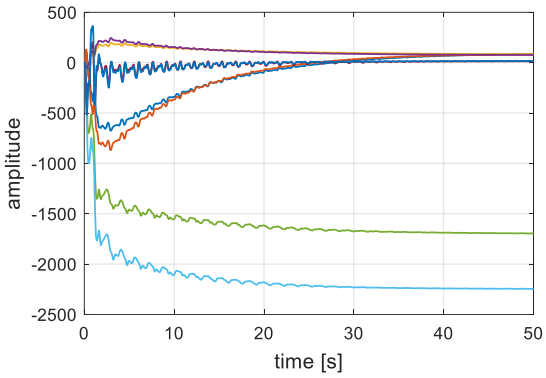

Figure 9: Convergence of the controller gains, $\mathbf{K}_x$.

The time responses of the vehicle body vertical accelerations and pitch angle of the active suspension system (solid line) and the passive system (dotted line) over the road input defined above is depicted in Figure 10 and Figure 11, respectively. It is revealed that the active suspension system has significantly improved the ride comfort compared with the passive system in terms of reduction the magnitude of vehicle body vertical acceleration and pitch angle.

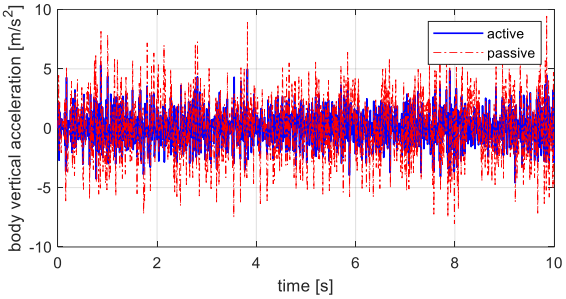

Figure 10: Vehicle body vertical accelerations (solid line – active system, dotted line - passive system).

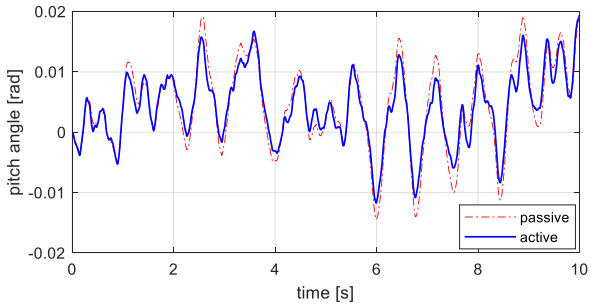

Figure 11: Pitch angle of the vehicle body (solid line – active system, dotted line - passive system).

The comparison of the suspension deflections at the front/rear wheel between the active system and the passive one is shown in Figure 12, in which the solid lines are for the active system and the dotted lines are for the passive system. To quantitatively evaluate the performance of the active suspension system with MRAC, root mean square values of the body vertical acceleration, suspension deflection of both passive and active system were calculated, and the obtained results are shown in Table 2. It can be seen from Table 2 that compared with the passive suspension system, the active system with MRAC can improve the ride comfort in term of vehicle body vertical acceleration by 45.51% and in term of pitch angle by 13.25%. The suspension deflections at the front wheel and the rear wheel are also improved by 18,09% and 34.42%, respectively.

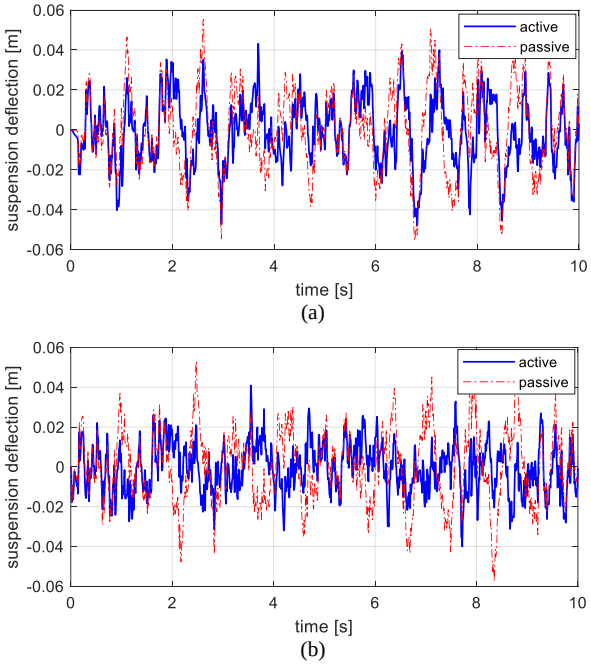

Figure 12: Suspension deflections at a) the rear wheel and b) the front wheel (solid line – active system, dotted line - passive system).

Table 2: Root mean square values of suspension performance indexes.

Suspension performance index	Passive system (Case 2)	Active system with MRAC	Improvement
Body vertical acceleration (m/s^2)	2.6118	1.4232	45.51%
Suspension deflection at front wheel (m)	0.0199	0.0163	18,09%
Suspension deflection at rear wheel (m)	0.0183	0.0120	34,42%
Pitch angle (rad)	0.0083	0.0072	13.25%

5. Conclusion

This paper presented a MRAC for the half-car active suspension systems with unknown spring stiffness and damping coefficients. A reference model for the half-car suspension system was proposed. The Lyapunov stability criteria was utilized for the MRAC design. The responses in the frequency domain show that the reference model provides better performance in terms of the ride comfort and suspension deflection

than all the passive suspension systems with spring stiffness and damping coefficients were varied up to 30% from the nominal values of the reference system. The convergence of the dynamic responses of the active suspension system incorporated with MRAC to that of the reference model was verified by numerical simulations in the time domain. The obtained results in the time domain are also revealed that the performance of the active suspension system with MRAC (i.e., vehicle body vertical acceleration, pitch angle, and suspension deflection) has been significantly. To implement the MRAC in practice, futher studies are required to examine realistic phenomena such as nonlinearity, uncertainty, physical limitations, etc. Also, the effects of tire dynamics and full-car model should be considered.

Acknowledgement

This research is funded by the Murata Foundation under the project code: T2022-02-06-MSF.

References

[1] Goodarzi and A. Khajepour, "Vehicle suspension system technology and design," *Synthesis Lectures on Advances in Automotive Technology*, vol. 1, no. 1, pp. i-77, 2017. https://doi.org/10.1007/978-3-031-01494-9

[2] ISO 2631-1, "International organization of standardization. Mechanical vibration and shock – evaluation of human exposure to whole body vibration. Part 1: General requirement," Geneva, 1997. https://www.iso.org/standard/7612.html

[3] W. Sun, H. Gao, and O. Kaynak, "Finite frequency H-infinity control for vehicle active suspension systems," *IEEE Transactions on Control Systems Technology*, vol. 19, no. 2, pp. 416-422, 2011. https://doi.org/10.1109/TCST.2010.2042296

[4] Y. Qin, M. Dong, R. Langari, L. Gu, and J. Guan, "Adaptive hybrid control of vehicle semiactive suspension based on road profile estimation," *Shock and Vibration*, ID 636739, 2015. https://doi.org/10.1155/2015/636739

[5] L.H. Nguyen, K.-S. Hong, and S. Park, "Road frequency adaptive control for semi-active suspension systems," *International Journal of Control, Automation, and System*, vol. 8, no. 5, pp. 1029-1038, 2010. https://doi.org/10.1007/s12555-010-0512-1

[6] M.O. Yatak and F. Sahin, "Ride comfort-road holding trade-off improvement of full vehicle active suspension system by interval type 2 fuzzy control," *Engineering Science and Technology, an International Journal*, vol. 24, no. 1, pp. 259-270, 2021. https://doi.org/10.1016/j.jestch.2020.10.006

[7] W. Li, Z. Xie, P.N. Wong, Y. Cao, X. Hua, and J. Zhao, "Robust nonfragile H-infinity optimum control for active suspension systems with time-varying actuator delay," *Journal of Vibration and Control*, vol. 0, no. 0, pp. 1-18, 2019. https://doi.org/10.1177/1077546319857338

[8] S. Nie, Y. Zhuang, F. Chen, Y. Wang, and S. Liu, "A method to estimate unsprung adverse effect of in-wheel motor-driven vehicles," *Journal of Low Frequency Noise, Vibration and Active Control*, vol. 37, no. 4, pp. 955-976, 2018. https://doi.org/10.1177/1461348418767096

[9] G.D. Shelke, A.C. Mitra, and V.R. Varude, "Validation of simulation and analytical model of nonlinear passive vehicle suspension system for quarter car," *Materials Today: Proceedings*, vol. 5, no. 9, pp. 19294-19302, 2018. https://doi.org/10.1016/j.matpr.2018.06.288

[10] M.M. Rashid, M.A. Hussain, N.A. Rahim, and J.S. Momoh, "Development of semi-active car suspension control system using magneto-rheological damper model," *International Journal of Mechanical and Materials Engineering*, vol. 2, no. 2, pp. 93-108, 2007. https://core.ac.uk/download/pdf/162010461.pdf

[11] K.H. Florean-Aquino, M. Arias-Montiel, J. Linares-Flores, J.B. Mendoza-Larios, and A. Cabrera-Amado, "Modern semi-active control schemes for suspension with MR actuator for vibration attenuation," *Actuators*, vol. 10, no. 2, 2021. https://doi.org/10.3390/act10020022

[12] Y. Zhao and X. Wang, "A review of low-frequency active vibration control of seat suspension systems," *Applied Science*, vol. 9, no. 16, pp. 1-28, 2019. https://doi.org/10.3390/app9163326

[13] E. Enders, G. Burkhard, and N. Munzinger, "Analysis of the influence of suspension actuator limitations on ride comfort in passenger cars using model predictive control," *Actuators*, vol. 9, no. 3, 2020. https://doi.org/10.3390/act9030077

[14] Y. Shahid and M. Wei, "Comparative analysis of different model-based controllers using active vehicle suspension system," *Algorithms*, vol. 13, no. 1, 2020. https://doi.org/10.3390/a13010010

[15] N. Singh, H. Chhabra, and K. Bhangal, "Robust control of vehicle active suspension system" *International Journal of Control and Automation*, vol. 9, no. 4, pp. 149-160, 2016. http://article.nadiapub.com/IJCA/vol9_no4/15.pdf

[16] Q. Zhao and B. Zhu, "Multi-objective optimization of active suspension predictive control based on improved PSO algorithm," *Journal of Vibroengineering*, vol. 21, no. 5, pp. 1388-1404, 2019. https://doi.org/10.21595/jve.2018.19580

[17] M. Sunwoo, K. C. Cheok, and N.J. Huang, "Model reference adaptive control of vehicle active suspension systems," *IEEE Transactions on Industrial Electronics*, vol. 38, no. 3, pp. 217-222, 1991. https://doi.org/10.1109/41.87590

[18] A.K. Mohammadi, "Active control of vehicle active suspension with preview using variable structure model reference adaptive controller," *International Journal of Vehicle Autonomous Systems*, vol. 3, no. 2-4, 253-264, 2005. https://doi.org/10.1504/IJVAS.2005.008236

[19] Y. Mousavi, A. Zarei, I.B. Kucukdemiral, A. Fekih and A. Alfi, "Disturbance observer and tube-based model reference adaptive control for active suspension systems with non-ideal actuators," *IFAC PapersOnline*, vol. 56, no. 2, pp. 1076-1081, 2023. https://doi.org/10.1016/j.ifacol.2023.10.1707

[20] Y.J. Liang and S.L. Wu, "Optimal vibration control for tracked vehicle suspension systems," *Mathematical Problems in Engineering*, vol. 2013, ID. 178354, 2013. https://doi.org/10.1155/2013/178354

[21] S.D. Bruyne, H.V. Auweraer, J. Anthonis, W. Desmet, and J. Swevers, "Preview control of a constrained hydraulic active suspension system," *in 51st IEEE Conference on Decision and Control*, Hawaii, USA, 2012, pp. 4400-4405. https://doi.org/10.1109/CDC.2012.6425847

[22] Y. Huang, J. Na, X. Wu, X. Liu, and Y. Guo, "Adaptive control of nonlinear uncertain active suspension systems with prescribed performance," *ISA Transactions*, vol. 54, pp. 145-155, 2015. https://doi.org/10.1016/j.isatra.2014.05.025

[23] W. Sun, H. Pan, Y. Zhang, and H. Gao, "Multi-objective control for uncertain nonlinear active suspension systems," *Mechatronics*, vol. 24, no. 4, pp. 318-327, 2014. https://doi.org/10.1016/j.mechatronics.2013.09.009

[24] D. Karnopp, M.J. Crosby, and R.A. Harwood, "Vibration control using semi-active force generators," *Journal of Engineering for Industry*, vol. 96, no. 2, pp. 619-626, 1974. https://doi.org/10.1115/1.3438373

[25] H.K. Khalil, *Nonlinear Systems*, 3rd edition, Prentice Hall, 2001.

[26] Y. Zhang, W. Chen, L. Chen, and W. Shangguan, "Non-stationary random vibration analysis of vehicle with fractional damping," *in 13th National Conference on Mechanisms and Machines*, Bangalore, India, 2007, pp. 171-178. https://doi.org/10.1109/ICICTA.2008.348

Vol 5 (1) (2024)

Measurement, Control, and Automation

Website: https:// mca-journal.org

ISSN 1859-0551

Parameter Optimization of Sliding Mode Controller for Tower Crane Using Particle Swarm Optimization Algorithm

Thi-Ly Tong[1], Minh-Trung Ho[2], Hoang-Hiep Dao[3], Vu-Khanh Pham[3], Minh-Duc Duong[3], Quy-Thinh Dao[3,]*

[1]*Faculty of Electrical Engineering, Hanoi University of Industry*
[2]*Military Environmental Chemistry Institute, Chemical Corps*
[3]*School of Electrical and Electronic Engineering, Hanoi University of Science and Technology*
**Corresponding author E-mail: thinh.daoquy@hust.edu.vn*

Abstract

Tower cranes find extensive application in the construction, ports, and industrial sectors for efficiently managing the transportation of heavy loads. However, operators face potential risks due to oscillations that occur during load movements. This not only diminishes operational efficiency but also poses significant hazards. Consequently, the control of tower cranes becomes a formidable challenge. To address this issue, various studies have been proposed, with particular attention given to the use of Sliding Mode Control (SMC). Vibrations caused by tower cranes have been mitigated by these studies. However, with SMC controllers for tower cranes, the problem of optimal parameter selection has not been adequately addressed by existing research. In this paper, a Particle Swarm Optimization (PSO) algorithm is used in conjunction with an SMC controller to determine the optimal parameter set for tower crane systems. A hierarchical sliding mode controller (HSMC) is utilized to control the position and minimize load oscillations. The PSO algorithm is applied to optimize the position settling time and angular deviation of the load. The SMC controller with the obtained optimal parameters achieves superior performance in tower crane systems, as demonstrated in simulations and experiments.

***Keywords**: Hierarchical sliding mode controller, Particle swarm optimization, Sliding mode control, Tower crane.*

Symbols

Symbols	Units	Description
m_t, m_c	kg	Trolley mass and load mass
R	m	Trolley position
γ	Degree	Jib angle
α, β	Degree	Load angles on plane Oxz and Oyz
u_t	N	Trolley's control signal
u_r	Nm	Jib's control signal
l	m	Rope length
λ_1, λ_2, λ_3, λ_4, η_1, η_2, K_1, K_2		Controller parameter

Abbreviations

SMC	Sliding Mode Controllers
HSMC	Hierarchical Sliding Mode Controller
PSO	Particle Swarm Optimization

1. Introduction

Tower cranes are a vital component in the construction of tall buildings, massive structures, and complex projects. However, the crane operation is highly susceptible to the payload's oscillatory movements, which might put workers and equipment at risk. [1]. Typically, suppressing these movements calls for a more sophisticated control algorithm. A great variety of contributions to crane control can be found [2]. The proposed methods are mainly divided into two techniques including open-loop approaches and closed-loop approaches.

For open-loop control techniques, there are three widely used methods for tower crane systems which are command shaping [3], [4], filtering [5], [6], and command smoothing [7]–[9]. The advantage of these techniques is that they are simple to implement in practice, along with low cost. However, the impact of external disturbances such as wind, load changes, etc., on the system cannot be avoided. These noise effects cannot be eliminated using only open-loop control methods.

In the case of disturbances, closed-loop control techniques are more effective, the position of the load can be precisely controlled, and the system's swing angle can also be quickly suppressed. Regarding closed-loop control techniques, many controllers have been applied to tower crane systems such as linear control [10]–[14], predictive control [15], [16], adaptive control [17]–[20], fuzzy logic approaches [21]–[24], and sliding mode control [25]–[27], etc. Among these close-loop techniques, sliding mode control – SMC is a well-known method owing to its effectiveness, simplicity to implement in practice, stability, and robustness, even when the system encounters [28]. The efficiency of SMC for vibration suppression has been proven in [29]–[31]. However, up to now, only a few publications have mentioned the methods for selecting parameters for the controller as well as evaluating the

Received: 09 January 2024; Accepted: 20 February 2024.

effectiveness between different sets of parameters for the same system.

This article proposes an approach to designing a position and anti-vibration controller for tower cranes, based on the SMC method that integrates the following functions:

- A hierarchical structure for the sliding mode controller.
- Employing an optimization algorithm PSO for selecting SMC's parameter to reduce the system's setting time and lower the load's angle.

Because the tower crane is an under-actuated system, the hierarchical sliding controller was designed and utilized. In addition, the PSO algorithm will help to find parameter values to achieve the goal of optimizing setup time and reducing load swing angle deviation.

The rest of this paper is organized as follows: Section 2 introduces a dynamic model of a tower crane and details important components of this model; Section 3 presents the design of the SMC controller, developed for position control and vibration suppression of tower cranes. This is an important part, explaining in detail the SMC sliding control method and how to apply it to the tower crane system; Section 4 introduces the PSO optimization algorithm to adjust parameters in the controller. This section demonstrates how to apply the PSO algorithm to find optimal parameters for the SMC controller; Section 5 presents simulation results on Matlab/Simulink and provides results from the experimental model. This is the part to evaluates the performance and effectiveness of the proposed method through simulation and experimental results; Finally, Section 6 is the conclusion, summarizing the results and emphasizing the contributions and limitations of the research, while also suggesting future development directions.

2. Tower Crane system dynamic

The physical model of the tower crane illustrated in Figure 1, includes two motions which are the translation motion of the trolley on the jib and the slewing motion of the jib around the tower. The cargo mass m_c is attached to the trolley through a cable system that is responsible for lifting and lowering loads. When a force and a torque are acted on the trolley and the jib, the load will vibrate due to fictitious force during movement. In this system, considering only the translation motion and the slewing motion, ignoring the mass of the rope and the elastic deformation of the tower, assuming that the load angles are small, and the length of the cable stays unchanged, Euler-Lagrange equations are used to obtain the dynamics of the tower crane.

The kinetic energy of the tower crane is calculated as:

$$K = \frac{1}{2} m_t \dot{x}_t^2 + \frac{1}{2} m_c \dot{x}_c^2 + \frac{1}{2} J \dot{\gamma}^2 \quad (1)$$

where:

$\dot{x}_t$ is the velocity of the trolley.

$\dot{x}_c$ là the velocity of the load.

$\dot{\gamma}$ is the angular velocity of the jib.

The potential energy of the tower crane is determined as:

$$P = -m_c g l \cos\beta \cos\alpha \quad (2)$$

From (1) and (2), the Lagrange function is established as:

$$L = K - P = \frac{1}{2} m_t \dot{x}_t^2 + \frac{1}{2} m_c \dot{x}_c^2 + \frac{1}{2} J \dot{\gamma}^2 + m_c g l \cos\beta \cos\alpha \quad (3)$$

Figure 1. Tower crane model.

Corresponding to each state variable, the dynamic equations are established [32]:

$$\begin{cases} \dfrac{d}{dt}\left(\dfrac{\partial L}{\partial \dot{R}}\right) - \dfrac{\partial L}{\partial R} = u_t \\ \dfrac{d}{dt}\left(\dfrac{\partial L}{\partial \dot{\gamma}}\right) - \dfrac{\partial L}{\partial \gamma} = u_r \\ \dfrac{d}{dt}\left(\dfrac{\partial L}{\partial \dot{\alpha}}\right) - \dfrac{\partial L}{\partial \alpha} = 0 \\ \dfrac{d}{dt}\left(\dfrac{\partial L}{\partial \dot{\beta}}\right) - \dfrac{\partial L}{\partial \beta} = 0 \end{cases} \quad (4)$$

Ignoring the small complicated non-linear components, trigonometric approximations are also used to simplify the calculations (4), the dynamics model of the tower crane is obtained:

$$\begin{cases} \ddot{R} + \dfrac{m_c}{m_t} g\alpha = \dfrac{u_t}{m_t} \\ (1 + \dfrac{m_t}{J} R^2)\ddot{\gamma} - \dfrac{m_c}{J} gR\alpha = \dfrac{u_r}{m_t} \\ l\ddot{\alpha} + g\alpha - \ddot{R} = 0 \\ l\ddot{\beta} + g\beta + R\ddot{\gamma} = 0 \end{cases} \quad (5)$$

The differential equations in (5) describe the variation of state variables, including the trolley position R, the rotation angle γ of the jib, and the swing angles α and β of the load. The state variables depend on the input variables, including the force u_t acts on the trolley, the torque u_r acts on the jib, and model parameters such as m_t, l, m_c, J, and g.

In practice, the movement of the trolley R and the jib γ are controlled independently by two motors with drivers allowing us to control the speed of the trolley and the jib separately, accurately, and eliminate the effect of external disturbances. Although equation (5) has four state variables, there are only two actuators, making the system an under-actuated system. We can see that the first and second equations in (5) interact with the swing angle state variable α. However, in this study, by using motor drivers with ideal current loops and speed loops, the influence of angle α on the first two equations can be eliminated. Besides, because the inner circuit which is used to drive the motors, is much faster than the outer speed circuit,

according to [33] we can simplify the first equation. and the second of (5) as follows:

$$\frac{R(s)}{U_t(s)} = \frac{F_1}{s(T_1 s + 1)} \tag{6}$$

Where, U(s) is the Laplace transformation of the voltage signal control the trolley $u_t(t)$, $R(s)$ is the Laplace transformation of the position of the trolley $r(t)$, $F_1$is a gain factor, and T_1 is the time constant of the system.
Inverse Laplace transform equation (6), we have:

$$\ddot{R} + \frac{1}{T_1}\dot{R} = \frac{F_1}{T_1}u_t \tag{7}$$

Similarly, the model that controls the rotation angle of the jib can be expressed as:

$$\ddot{\gamma} + \frac{1}{T_2}\dot{\gamma} = \frac{F_2}{T_2}u_r \tag{8}$$

The dynamic model of the tower crane can be rewritten as follows:

$$\ddot{R} + \frac{1}{T_1}\dot{R} = \frac{F_1}{T_1}u_t \tag{9}$$

$$\ddot{\gamma} + \frac{1}{T_2}\dot{\gamma} = \frac{F_2}{T_2}u_r \tag{10}$$

$$l\ddot{\alpha} + g\alpha - \ddot{R} = 0 \tag{11}$$

$$l\ddot{\beta} + g\beta + R\ddot{\gamma} = 0 \tag{12}$$

It should be noted here that we will design the position and angle control by including the motor transmission system, so the input control signal has been converted to voltage. In this study, we will use equations (9)-(12) to design a controller for the tower crane in the next section.

3. Controller design and control parameter optimization

3.1. Design of the Hierarchical Sliding Mode Controller

According to the dynamics model (9)-(12), the tower crane is an under-actuated system. The purpose of this paper is to design a controller that drives the trolley and the jib to the desired position and reduces the swing angles of the cargo to zero. A hierarchical sliding mode control approach is proposed to control the under-actuated system such as the tower crane with u_t, u_r are the control inputs and R, γ, α, β are the system state. Designing of the HSMC includes two steps:

- First, a first-order sliding surface is defined to attract all state trajectories.
- Then a control scheme is built to force all system states to their reference values on the sliding surface.

Set the system state R, γ, α, β as state variables as follow:

$$\begin{aligned} &x_1 = R;\ x_2 = \dot{x}_1;\ x_3 = \gamma;\ x_4 = \dot{x}_3; \\ &x_5 = \alpha; x_6 = \dot{x}_5; x_7 = \beta; x_8 = \dot{x}_7 \end{aligned} \tag{13}$$

Define the regulation error vectors as follows:

$$e_1 = x_1 - x_{1d};\ e_3 = x_3 - x_{3d};\ e_5 = x_5;\ e_7 = x_7 \tag{14}$$

Substituting (13) into equations (9)-(12) and presenting them in the state-space model, one can obtain the state-space model of the tower crane as follows:

$$\begin{aligned} &\dot{x}_1 = x_2; \quad \dot{x}_2 = \frac{F_1}{T_1}u_t - \frac{1}{T_1}x_2; \\ &\dot{x}_3 = x_4; \quad \dot{x}_4 = \frac{F_2}{T_2}u_r - \frac{1}{T_2}x_4; \\ &\dot{x}_5 = x_6; \quad \dot{x}_6 = \frac{\dot{x}_2}{l} - \frac{gx_5}{l}; \\ &\dot{x}_7 = x_8; \quad \dot{x}_8 = -x_1\frac{\dot{x}_4}{l} - \frac{gx_7}{l}; \end{aligned} \tag{15}$$

Define the sliding surface as:

$$S = \begin{bmatrix} S_1 & S_2 \end{bmatrix}^T \tag{16}$$

Where:

$$\begin{aligned} S_1 &= \dot{e}_1 + \lambda_1 e_1 + \eta_1 \dot{e}_5 + \lambda_3 e_5 \\ S_2 &= \dot{e}_3 + \lambda_2 e_3 + \eta_2 \dot{e}_7 + \lambda_4 e_7 \end{aligned} \tag{17}$$

Differentiating equation (16) with respect to time, we have:

$$\begin{cases} \dot{S} = \begin{bmatrix} \dot{S}_1 & \dot{S}_2 \end{bmatrix}^T \\ \dot{S}_1 = \ddot{e}_1 + \lambda_1 \dot{e}_1 + \eta_1 \ddot{e}_5 + \lambda_3 \dot{e}_5 \\ \dot{S}_2 = \ddot{e}_3 + \lambda_2 \dot{e}_3 + \eta_2 \ddot{e}_7 + \lambda_4 \dot{e}_7 \end{cases} \tag{18}$$

Next, we choose the constant rate reaching law for the system:

$$\begin{cases} \dot{S}_1 = -K_1 sign(S_1) \\ \dot{S}_2 = -K_2 sign(S_2) \end{cases} \tag{19}$$

Substituting equations (15)-(18) into equation (19), the control signal can be established as:

$$\begin{aligned} u_t = \frac{1}{F_1(\eta_1 + l)}[&T_1\eta_1 g x_5 + l x_2 + \eta_1 x_2 \\ &+ T_1 l(\ddot{x}_{1d} - \lambda_1(x_2 - \dot{x}_{1d}) - \lambda_3 x_6) - T_1 l K_1 \operatorname{sgn}(S_1)] \end{aligned} \tag{20}$$

$$\begin{aligned} u_r = \frac{1}{F_2 J(l - \eta_2 x_1)}[&l x_4 - \eta_2 x_1 x_4 + T_2\eta_2 g x_7 \\ &+ T_2 l(\ddot{x}_{3d} - \lambda_2(x_4 - \dot{x}_{3d}) - \lambda_4 x_8) - T_2 l K_2 \operatorname{sgn}(S_2)] \end{aligned} \tag{21}$$

To reduce the effect of the chattering phenomenon, we replace the Sign function with a saturation function as follows:

$$sat\left(\frac{s_i}{\varepsilon}\right) = \begin{cases} sign(s_i) \text{ khi } |s_i| > \varepsilon \\ \dfrac{s_i}{\varepsilon} \text{ khi } |s_i| \le \varepsilon \end{cases}; \tag{22}$$

3.2. Stability analysis

To ensure the stability of the system, as a first step, we choose the Lyapunov function $V = \frac{1}{2}S^T S \ge 0$. Where: $\dot{V} = -K_1|S_1| - K_2|S_2| \le 0$ with every $K_1 > 0$, $K_2 > 0$. This means the system can maintain sliding on the sliding surface S = 0. However, for each sliding surface, it is a combination of the error between the output value compared to the setpoint value and the swing angle of the cargo. Thus, this combination doesn't guarantee that all the controlled variables will converge to their references on the sliding manifold. Therefore,

we need to consider the system state on the sliding surface. Substituting S = 0 into equation (17), then into equation (15). Through these transformations, we obtain a space-state model represented as follows:

$$\dot{Y} = AY \tag{23}$$

where $Y = [Y_1 \quad Y_2 \quad Y_3 \quad Y_4 \quad Y_5 \quad Y_6]^T$ with $Y_1 = x_5 = \alpha$; $Y_2 = x_7 = \beta$; $Y_3 = x_6 = \dot{x}_5$; $Y_4 = x_8 = \dot{x}_7$; $Y_5 = x_1 - x_{1d}$; $Y_6 = x_3 - x_{3d}$.

$$A = \begin{bmatrix} A_1 & A_2 & A_3 & A_4 & A_5 & A_6 \end{bmatrix}$$

where

$$A_1 = \begin{bmatrix} 0 & 0 & \dfrac{\lambda_1\lambda_3 - g}{(\eta_1 + l)} & 0 & -\lambda_3 & 0 \end{bmatrix}^T$$

$$A_2 = \begin{bmatrix} 0 & 0 & 0 & -\dfrac{x_1\lambda_2\lambda_4 + g}{l - \eta_2 x_1} & 0 & -\lambda_4 \end{bmatrix}^T$$

$$A_3 = \begin{bmatrix} 1 & 0 & \dfrac{\lambda_1\eta_1 - \lambda_3}{(\eta_1 + l)} & 0 & -\eta_1 & 0 \end{bmatrix}^T$$

$$A_4 = \begin{bmatrix} 0 & 1 & 0 & -x_1\dfrac{\lambda_2\eta_2 - \lambda_4}{l - \eta_2 x_1} & 0 & -\eta_2 \end{bmatrix}^T$$

$$A_5 = \begin{bmatrix} 0 & 0 & \dfrac{\lambda_1^{\,2}}{(\eta_1 + l)} & 0 & -\lambda_1 & 0 \end{bmatrix}^T$$

$$A_6 = \begin{bmatrix} 0 & 0 & 0 & -x_1\dfrac{\lambda_2^{\,2}}{l - \eta_2 x_1} & 0 & -\lambda_2 \end{bmatrix}^T$$

To guarantee the stability of the system, the linearized state matrix **A** should be Hurwitz (i.e. its eigenvalues are located in the left half of the complex plane). After a series of calculations, the stability conditions are given as:

$$\begin{cases} \lambda_1 > 0 \\ \eta_1 > -l \\ \lambda_3 > \lambda_1\eta_1 \\ \lambda_2 > 0 \\ \eta_2 x_{1d} < l \\ \lambda_4 x_{1d} < \lambda_2\eta_2 x_{1d} \end{cases} \tag{24}$$

With the proposed HSMC controller (20)-(21), the performance quality of the tower crane not only depends on model parameters such as *l, and J*, but also on the parameters of the controller including λ_1, λ_2, λ_3, λ_4, η_1, η_2, K_1, K_2. In this paper, we propose the use of the PSO algorithm to find the optimal parameters for the HSMC controller, with the goal of optimizing the settling time and swing angle error of the load.

3.3. HSMC's parameter optimization

In this paper, the PSO algorithm is used to obtain 8 parameters $\lambda_1, \lambda_2, \lambda_3, \lambda_4, \eta_1, \eta_2, K_1, K_2$ of the HSMC controller base on fitness function. How this fitness function is defined depends on the optimization target of each problem. As mentioned before, the goal of this research is to reduce the settling time. Furthermore, this paper also aims to lower the load's angle when the trolley and jig reach their reference position. From those targets, the fitness function for the PSO algorithm in this study is chosen as follows:

$$J = T_{xl} + \mu E_r \tag{25}$$

where

- T_{xl} is the 2% setting time of the system.
- $E_R = \sum_{t=T_{xl}}^{\infty}(|\alpha(t)| + |\beta(t)|)$ is the sum of swing angles after the system has settled.
- μ: weighting factor between T and e. If μ >1, PSO will prioritize for optimizing oscillations suppression. Otherwise, with μ <1 PSO will put more effort into reducing the settling time. In this article, the value of μ is chosen as 0.1.

The PSO algorithm is population-based optimization, where "particles" represent potential solutions. Particles move in the search space and interact with each other to search for the best location. The best location will correspond to the smallest fitness function value J.

The optimization will be done by adjusting the controller's parameter. With each set of parameters, the system will have a different response. Those responses will be evaluated by the fitness function. After many iterations of adjusting parameters and evaluating the response, the optimal parameters, which have a minimum value of J, are obtained.

From the works above, the whole control system can be summarized as in Figure 2.

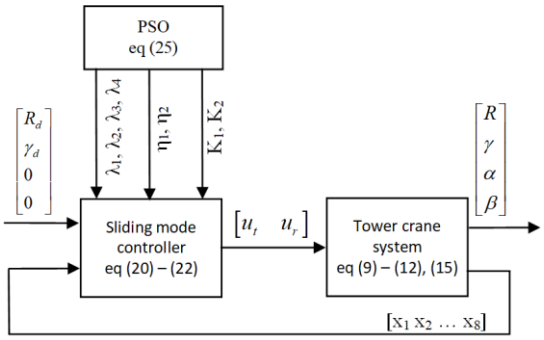

Figure 2. Tower crane control system diagram. Note that $x_1 = R, x_2 = \dot{x}_1, x_3 = \gamma, x_4 = \dot{x}_3, x_5 = \alpha, x_6 = \dot{x}_5, x_7 = \beta, x_8 = \dot{x}_7$.

4. Simulation and experimental results

4.1. Simulation and experimental setup

The parameter of the tower crane in this paper is: $T_1 = 0.01, T_2 = 0.08, F_1 = \frac{70\times2\times\pi\times0.016}{60}, F_2 = \frac{\left(\frac{10}{11}\right)\times2\pi}{60}, l = 0.59m,\ g = 9.81\frac{m}{s^2}$The starting positions of trolley and jib are R = 0 m and $\gamma = 0°$. The reference positions are $R = 0.3\ m, \gamma = 45°$. The boundary of controller parameters is detailed in (24). Control signal boundary is $\pm10V$ for u_t and $\pm10V$ for u_r.

In the next stage, PSO is started in Matlab/Simulink. First, a population of 50 particles is initialized. The maximum iteration is $K_{max} = 100$. With the PSO algorithm, the optimal parameter is obtained after K_{max} iterations.

This study is deployed on a tower crane model in the WSR laboratory of Hanoi University of Science and Technology. The tower crane model's structure is specified in Figures 3

and 4. The tower crane model has 2 moving axes driven by 2 servo transmission systems. Axis 1 is the rotation of the jib controlled by a servo motor accompanied by a high-ratio reduction gearbox. The transmission number is 1:11. The other axis is the forward motion of the trolley along the jib. The trolley is driven by a similar servo motor. Both motors used in the experiment are now in speed control mode. The entire system is controlled by the NI myRIO 1900 microcontroller, Table 1 describes the parameters of the servo motor. Labview software is used to program, control, and monitor the system. After obtaining the full parameters of the model and controller, the research was implemented on system simulation on Matlab/Simulink and then on the experimental model. Two scenarios are implemented in simulation and experiment to compare and evaluate the effectiveness of the parameter set that is determined by PSO:

- **Scenario 1:** The parameter of the SMC controller is selected manually.
- **Scenario 2**: Using the SMC controller parameters specified by the PSO algorithm.

Parameter sets of two scenarios are described in Table 2.

Table 1: Motor parameters

	Trolley's motor	Jib's motor
Rated output	200 W	200 W
Rated torque	1.27 N.m	1.27 N.m
Rated Speed	3000 rpm	3000 rpm
Inertia torque	$0.018 * 10^{-4}\ kg.m^2$	$0.018 * 10^{-4}\ kg.m^2$
Speed coefficient	$70\frac{rpm}{v}$	$10\frac{rpm}{v}$

Table 2: Controller parameters

SMC	SMC-PSO
$\lambda_1 = 1\ \ \lambda_2 = 0.9$	$\lambda_1 = 1.01\ \ \lambda_2 = 0.98$
$\lambda_3 = 1.1\ \ \lambda_4 = -1.5$	$\lambda_3 = 2.196\ \ \lambda_4 = -2.07$
$\eta_1 = 0.05$	$\eta_1 = 0.05$
$\eta_2 = -0.01$	$\eta_2 = -0.012$
$K_1 = 25\ \ K_2 = 70$	$K_1 = 35\ \ K_2 = 75$

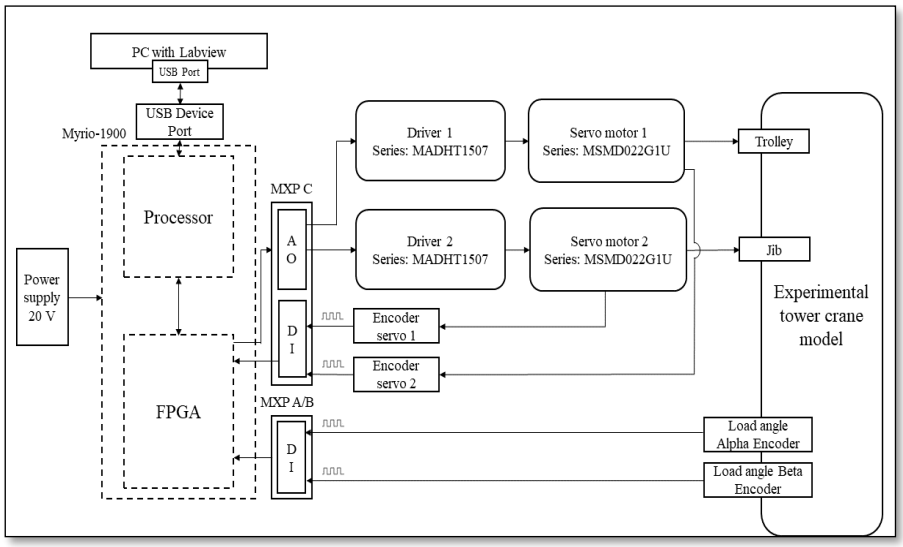

Figure 3. Experimental diagram.

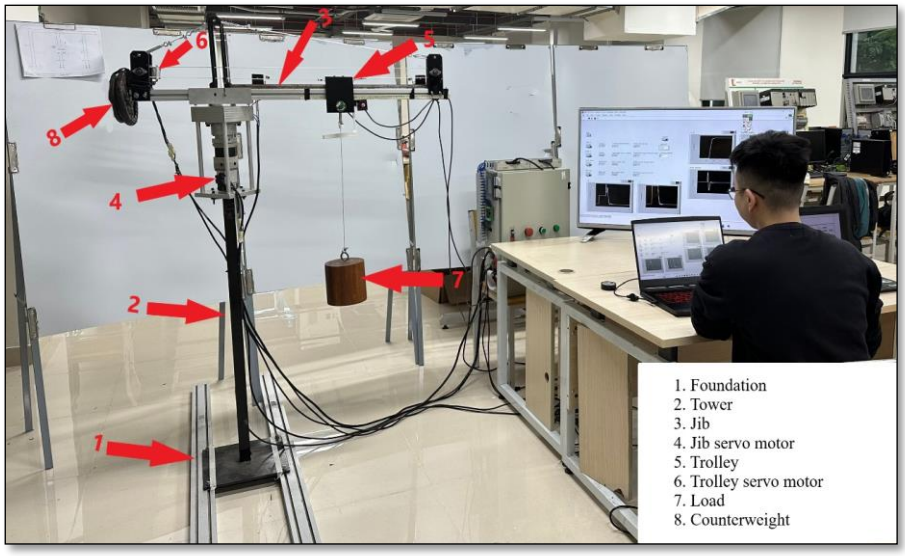

Figure 4. Experimental setup.

4.2. Simulation results

The results of the load angles α and β in Figure 5 show that with the use of the PSO-SMC controller, the settling time of the angles α and β are 2.5 seconds and 6.5 seconds, respectively. Meanwhile, when using the SMC controller without optimal parameters, the settling time of angles α and β is 7 seconds and 8.5 seconds. From these results, we can see the anti-vibration effectiveness of the PSO-SMC controller.

Figure 6 is the result of the position response R of the trolley and the rotation angle γ of the jib. The results show that when applying the PSO-SMC controller, the response time of rotation angle γ decreases from 4.2 seconds to 3.51 seconds. This result shows that the PSO algorithm has reduced the system setup time, as set out in section 4.1.

The voltage signals controlling the trolley u_t and the jib u_r are depicted in Figure 7, we can see that the PSO-SMC controller helps reduce the fluctuation of the control signal. This is achieved thanks to the rapid anti-vibration effect that the proposed controller provides.

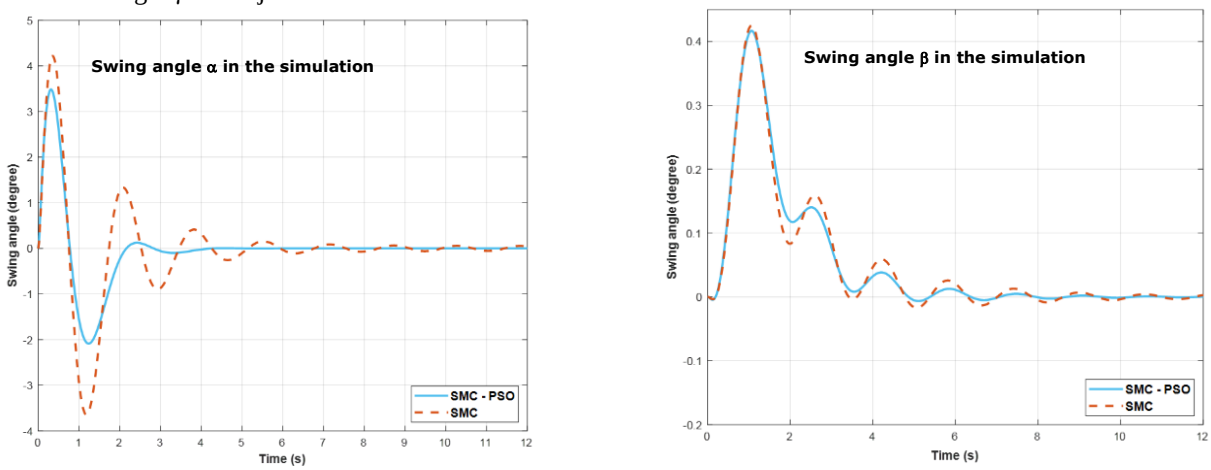

Figure 5. Load swing angle α and β in simulation.

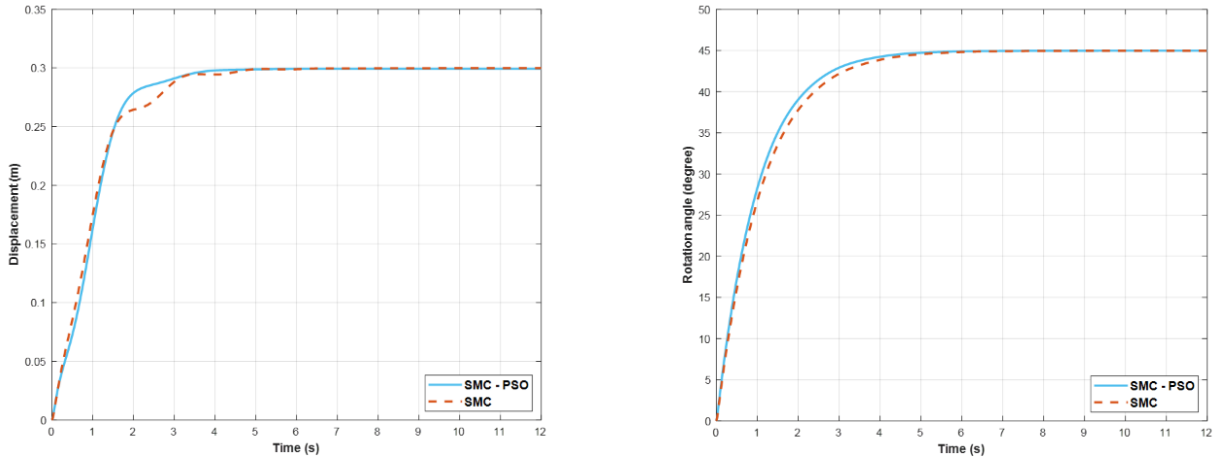

Figure 6. Trolley position in the jib and jib rotation angle in simulation.

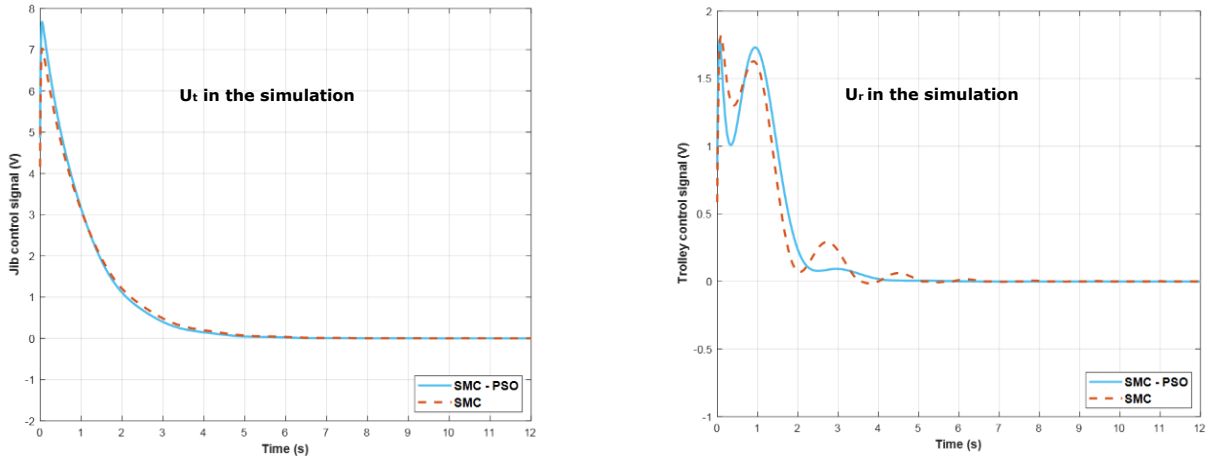

Figure 7. The control signal U_t and U_r in simulation

4.3. Experimental result

Experimental results Figure 8 verifies the anti-vibration effectiveness as mentioned in the simulation results above. When combining PSO with SMC, the oscillation angles α and β of the load are extinguished at the 5th second. Meanwhile, in the SMC controller with randomly selected parameters in scenario 1, the oscillation time of angles α and β is up to 11 seconds. Through this, we conclude that the PSO-SMC controller brings efficient oscillation suppression.

Figure 9 is the response of the trolley and jib when deployed on the experimental model. The jib settling time changes from 7.36 seconds to 6.27 seconds when applying the parameter set specified by PSO.

Figure 10 is the experimental result of the voltage signal controlling the trolley u_t and the jib u_r. Similar to the simulation results in Figure 6, when the oscillation phenomenon of the control signals u_r and u_t of the PSO-SMC controller is minimized.

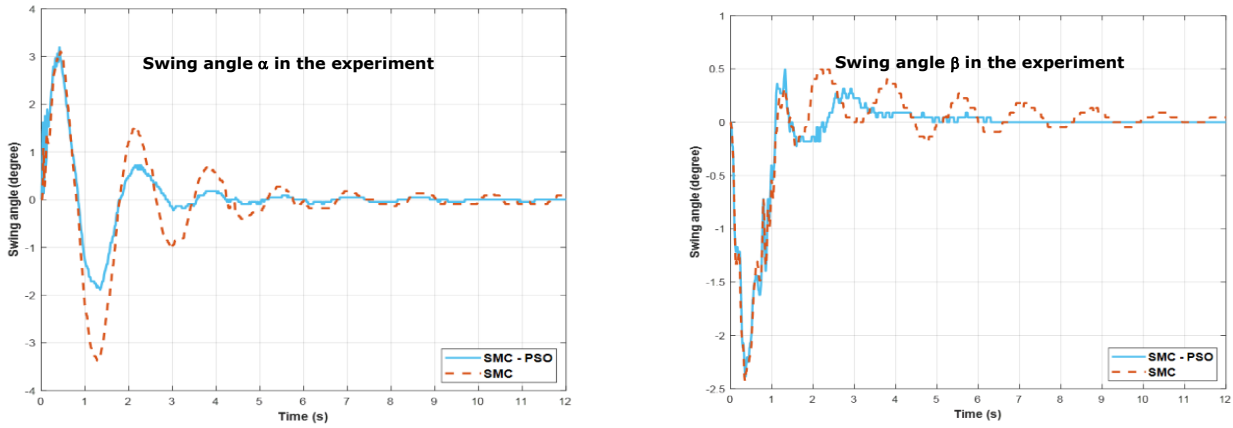

Figure 8. Load swing angle α and β in the experiment.

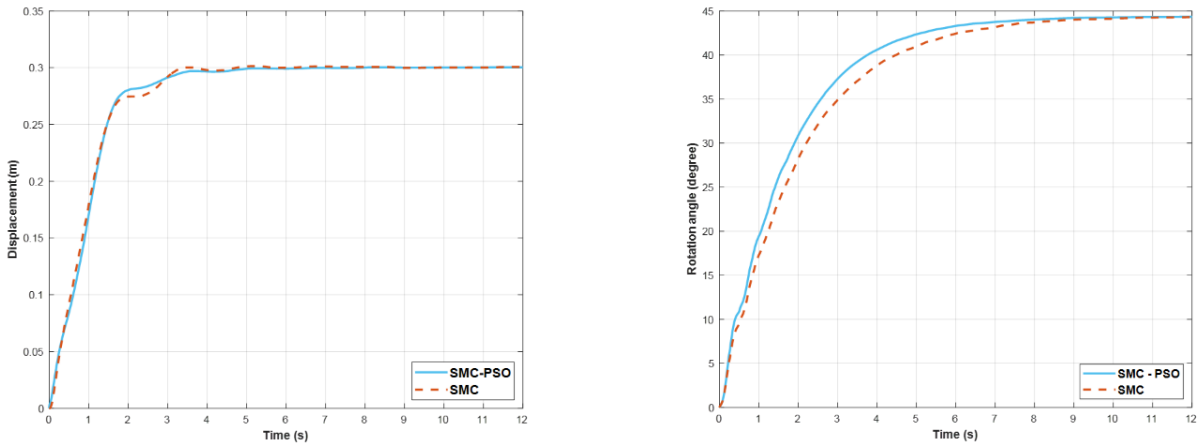

Figure 9. Trolley position in the jib and jib rotation angle in the experiment.

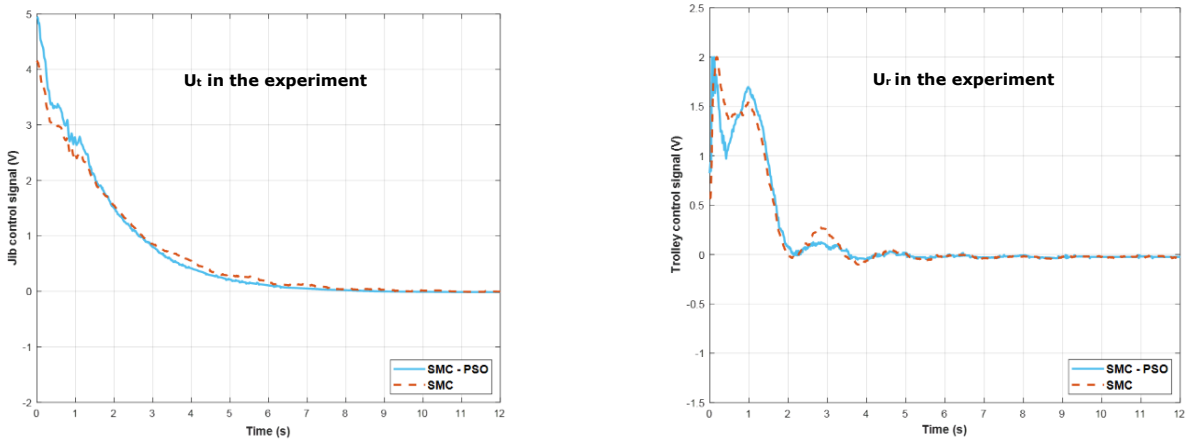

Figure 10. The control signal U_t and U_r in the experiment.

4.4. Evaluation of simulation and experimental results

From the results of simulation and experiment, we have a table of optimal results as shown in Table 3.

Table 3: Results comparison table.

		SMC	SMC-PSO
Simulation	System settling time	4.2s	3.51s
	Fitness function value J	4.34	3.53
Experiment	System settling time	7.36s	6.27s
	Fitness function value J	12.98	7.58

From Table 3, when using only the independent SMC controller, the settling time of the simulation system is 4.2 seconds, and the objective function value is 4.34. However, after integrating the PSO algorithm, this settling time is reduced to 3.51 seconds, and the objective function value is 3.53. In the experimental results, when using the PSO-SMC controller, the system settling time is only 6.27 seconds compared to 7.36 seconds when using the SMC controller. In addition, the objective function value is also reduced by 1.76 times.

Although there is a difference between the experimental and simulation results, both results show that the PSO-SMC controller provides higher anti-swinging performance and shorter settling time. This difference can be explained by the discrepancy between the real system and its mathematical model.

5. Conclusion

This article has presented an anti-vibration control method for tower cranes using the SMC sliding controller combined with the PSO optimization algorithm. Simulations and experiments have been implemented to demonstrate the correctness of this control method. After comparing the simulation and experimental results of the proposed controller with the SMC controller, some assessments are drawn including the PSO-SMC controller has a faster settling time (respectively 8.32% for simulation and 41.22% for experiment), along with the ability to suppress load vibrations faster as shown in Figure 4 and Figure 8. From these results, the combination between the PSO algorithm and SMC controller helps reduce system settling time, while improving anti-vibration efficiency.

However, the disadvantage of the SMC controller is that the system's control signals change too quickly. This phenomenon is called “Chattering”, which can cause high-frequency oscillations that adversely affect the system. Although after integrating the PSO algorithm, this phenomenon has been reduced thanks to the ability to quickly reduce vibration, the problem has not been completely resolved. Therefore, in the future, we will consider combining the PSO-SMC controller with the input signal shaping method. Finally, the above control method will also be considered and researched for implementation in tower crane systems with variable rope lengths.

References

[1] R.L. Neitzel, N.S.Seixas, and K.K. Ren, “A Review of Crane Safety in the Construction Industry: Applied Occupational and Environmental Hygiene: Vol 16, No 12.”

[2] L. Ramli, Z. Mohamed, A. M. Abdullahi, H. I. Jaafar, and I. M. Lazim, “Control strategies for crane systems: A comprehensive review,” *Mech. Syst. Signal Process.*, vol. 95, pp. 1–23, Oct. 2017, doi: 10.1016/j.ymssp.2017.03.015.

[3] Gordon G. Parker, Ben Petterson, Clark R. Dohrmann, and Rush D. Robinett III, “Vibration suppression of fixed-time jib crane maneuvers.”

[4] G. G. Parker, B. Petterson, C. Dohrmann and R. D. Robinett, “Command shaping for residual vibration free crane maneuvers,” Seattle, WA, USA: IEEE, 1995, pp. 934–938. doi: 10.1109/ACC.1995.529385.

[5] Q. Wu, X. Wang, L. Hua, and M. Xia, “Improved time optimal anti-swing control system based on low-pass filter for double pendulum crane system with distributed mass beam,” *Mech. Syst. Signal Process.*, vol. 151, p. 107444, Apr. 2021, doi: 10.1016/j.ymssp.2020.107444.

[6] D. Economou, C. Mavroidis and I. Antoniadis, “Comparison of filter types used for command preconditioning in vibration suppression applications,” Anchorage, AK, USA,: IEEE, 2022, pp. 2273–2278. doi: 10.1109/ACC.2002.1023979.

[7] J. Huang, Z. Liang, and Q. Zang, “Dynamics and swing control of double-pendulum bridge cranes with distributed-mass beams,” *Mech. Syst. Signal Process.*, vol. 54–55, pp. 357–366, Mar. 2015, doi: 10.1016/j.ymssp.2014.09.005.

[8] K. A. Alghanim, K. A. Alhazza, and Z. N. Masoud, “Discrete-time command profile for simultaneous travel and hoist maneuvers of overhead cranes,” *J. Sound Vib.*, vol. 345, pp. 47–57, Jun. 2015, doi: 10.1016/j.jsv.2015.01.042.

[9] R. Tang and J. Huang, “Control of bridge cranes with distributed-mass payloads under windy conditions,” *Mech. Syst. Signal Process.*, vol. 72–73, pp. 409–419, May 2016, doi: 10.1016/j.ymssp.2015.11.002.

[10] Shengzeng Zhang, Xiongxiong He, Haiyue Zhu, Xiaocong Li, and Xinggao Liu, “PID-like coupling control of underactuated overhead cranes with input constraints,” *ScienceDirect*, vol. 178, Oct. 2022, doi: 10.1016/j.ymssp.2022.109274.

[11] S. Chen, P. Xie, J. Liao, S. Wu, and Y. Su, “NMPC-PID control of secondary regulated active heave compensation system for offshore crane,” *Ocean Eng.*, vol. 287, p. 115902, Nov. 2023, doi: 10.1016/j.oceaneng.2023.115902.

[12] Hui Li, Yan-Ho Bui, Qiao Wang, Hong-Xiao Yang and Lin-Jun Wang, “Design of Anti-Swing PID Controller for Bridge Crane Based on PSO and SA Algorithm,” *Electronics*, vol. 11, no. 19, Sep. 2022, doi: 10.3390/electronics11193143.

[13] H. I. Jaafar, S. Y. S. Hussien, R. Ghazali and Z. Mohamed, “Optimal tuning of PID+PD controller by PFS for Gantry Crane System,” presented at the 2015 10th Asian Control Conference (ASCC), Kota Kinabalu, Malaysia, pp. 1–6. doi: 10.1109/ASCC.2015.7244695.

[14] F. Panuncio, W. Yu and X. Li, “Stable neural PID anti-swing control for an overhead crane,” presented at the 2013 IEEE International Symposium on Intelligent Control (ISIC), Hyderabad, India, 2013, pp. 53–58. doi: 10.1109/ISIC.2013.6658616.

[15] T. Baris̆a and M. Bartulovic, “Nonlinear Predictive Control of a Tower Crane using Reference Shaping Approach,” *Th Int. Power Electron. Motion Control Conf. Expo.*, 2014.

[16] P. Schubert and D. Abel, “Flatness-based Model Predictive Payload Control for Offshore Cranes,” in *2023 European Control Conference (ECC)*, Jun. 2023, pp. 1–8. doi: 10.23919/ECC57647.2023.10178159.

[17] N. Sun, Y. Fang, and H. Chen, “Adaptive antiswing control for cranes in the presence of rail length constraints and uncertainties,” *Nonlinear Dyn.*, vol. 81, Jul. 2015, doi: 10.1007/s11071-015-1971-y.

[18] J. Huang, W. Wang and J. Zhou, “Adaptive Control Design for Underactuated Cranes With Guaranteed Transient Performance: Theoretical Design and Experimental Verification,” vol. 69, no. 3, pp. 2822–2832, Mar. 2022, doi: 10.1109/TIE.2021.3065835.

[19] Menghua Zhang, Xin Ma, Xuewen Rong, Xincheng Tian, and Yibin Li, “Adaptive tracking control for double-pendulum overhead cranes subject to tracking error limitation, parametric uncertainties and external disturbances,” *Mech. Syst. Signal Process.*, vol. 76–77, pp. 15–32, 2016, doi: 10.1016/j.ymssp.2016.02.013.

[20] L. Yang and H. Ouyang, “Precision-positioning adaptive controller for swing elimination in three-dimensional overhead cranes with distributed mass beams,” *ISA Trans.*, vol. 127, pp. 449–460, Aug. 2022, doi: 10.1016/j.isatra.2021.08.035.

[21] T. Popadic, F. Kolonic, and A. Poljugan, “A fuzzy control scheme for the gantry crane position and load swing control,” vol. 3, Jan. 2006.

[22] L. Ramli, I. M. Lazim, H. I. Jaafar, and Z. Mohamed, “Modelling and Fuzzy Logic Control of an Underactuated Tower Crane System,” *Appl. Model. Simul.*, vol. 4, no. 0, Art. no. 0, Jan. 2020.

[23] Ling Ma, Xuyang Lou, Wei Wu and Xin Huang, "Neural network-based boundary control of a gantry crane system subject to input deadzone and external disturbance | Nonlinear Dynamics," Mar. 2022, doi: 10.1007/s11071-022-07356-z.

[24] Y. Qian, H. Zhang and D. Hu, "Finite-Time Neural Network-Based Hierarchical Sliding Mode Antiswing Control for Underactuated Dual Ship-Mounted Cranes With Unmatched Sea Wave Disturbances Suppression," *IEEE Transactions on Neural Networks and Learning Systems*, doi: 10.1109/TNNLS.2023.3257508.

[25] Qihang Guo, Lin Chai and Huikang Liu, "Anti-swing sliding mode control of three-dimensional double pendulum overhead cranes based on extended state observer," 2023, doi: 10.1007/s11071-022-07859-9.

[26] N. B. Almutairi and M. Zribi, "Sliding Mode Control of a Three-dimensional Overhead Crane," *J. Vib. Control*, vol. 15, no. 11, pp. 1679–1730, Nov. 2009, doi: 10.1177/1077546309105095.

[27] Le Anh Tuan, Jae-Jun Kim, Soon-Geul Lee, Tae-Gyoon Lim, and Luong Cong Nho, "Second-Order Sliding Mode Control of a 3D Overhead Crane with Uncertain System Parameters," *Int. J. Precis. Eng. Manuf.*, vol. 15, 2014, doi: 10.1007/s12541-014-0404-z.

[28] S. J. Gambhire, D. R. Kishore, P. S. Londhe, and S. N. Pawar, "Review of sliding mode based control techniques for control system applications," *Int. J. Dyn. Control*, vol. 9, no. 1, pp. 363–378, Mar. 2021, doi: 10.1007/s40435-020-00638-7.

[29] N. B. Almutairi and M. Zribi, "Sliding Mode Control of a Three-dimensional Overhead Crane," *J. Vib. Control*, vol. 15, no. 11, pp. 1679–1730, Nov. 2009, doi: 10.1177/1077546309105095.

[30] L. A. Tuan and S.-G. Lee, "Sliding mode controls of double-pendulum crane systems," *J. Mech. Sci. Technol.*, vol. 27, no. 6, pp. 1863–1873, Jun. 2013, doi: 10.1007/s12206-013-0437-8.

[31] K.-K. Shyu, C.-L. Jen, and L.-J. Shang, "Design of sliding-mode controller for anti-swing control of overhead cranes," in *31st Annual Conference of IEEE Industrial Electronics Society, 2005. IECON 2005.*, Nov. 2005, p. 6 pp.-. doi: 10.1109/IECON.2005.1568895.

[32] Hanafy M. Omar, "Control of Gantry and Tower Cranes," Blacksburg, Virginia, Jan. 2003.

[33] M. Böck and A. Kugi, "Real-time Nonlinear Model Predictive Path-Following Control of a Laboratory Tower Crane," *IEEE Trans. Control Syst. Technol.*, vol. 22, no. 4, pp. 1461–1473, Jul. 2014, doi: 10.1109/TCST.2013.2280464.

Vol 5 (1) (2024)

Measurement, Control, and Automation

Website: https:// mca-journal.org

ISSN 1859-0551

Online Inductances Estimation of the Permanent Magnet Synchronous Machines based on Deep Learning and Recursive Least Square Algorithms

Bui Xuan Minh[1]*, Le Khac Thuy[1], Le Minh Kien[1], Nguyen Trung Kien[1], Nguyen Thanh Tien[1], Pham Xuan Phuong[1]

[1] *Le Quy Don Technical University, Ha Noi, Vietnam*
**Corresponding author E-mail: minh.buixuan@ieee.org*

Abstract

This paper presents a novel method to identify in real time d- and q- axes inductances of the permanent magnet synchronous machines (PMSMs), which normally vary during the operation due to the saturation of the magnetic fields. The proposed method is based on the combination of deep learning and recursive least square algorithms. The deep learning model is trained offline to compensate the non-linearity effect of the voltage source inverter and the position measurement error, while the recursive least square algorithm is employed to estimate online d- and q- axes inductances based on the compensation d- and q- axes stator voltages, measured d- and q- axes stator currents and the operating speed. The proposed methods can overcome the problems associated with the existing model-based methods known as the effect of position measurement error and the unavailability of accurate information of the inverter. Extensive experimental studies were conducted to evaluate the estimation accuracy and the robustness of the proposed method in critical operating conditions including the variation of load torque, operating speed, and field-weakening condition.

Keywords*: PMSM, Online Parameter Identification, Deep Learning, Recursive Least Square.*

Symbols

Symbols	Units	Description
Ψ_m	Wb	Rotor flux linkage
R_s	Ω	Stator resistance
L_d, L_q	H	*d*- and *q*- axes stator inductance
i_d, i_q	A	*d*- and *q*- axes stator currents
v_d, v_q	V	*d*- and *q*- axes stator voltages
ω_{re}	Rad/s	Electrical angular speed of the rotor
θ_{re}	Rad/s	Electrical angular position of the rotor

Abbreviations

PMSM	Permanent Magnet Synchronous Machines
RLS	Recursive Least Square
ANN	Adaline Neural Network
FOC	Field Oriented Control
DTC	Direct Torque Control
MPC	Model Predictive Control

1. Introduction

Permanent magnet synchronous machines (PMSM) have been widely used in high-end applications, such as electric vehicles, wind-turbine generation, and robotics. The main advantages of these types of electric machines are known as high power density, high torque density and high control performance. So far, field-oriented control (FOC), direct torque control (DTC) and model predicted control (MPC) are the most popular control schemes for PMSMs. These control methods require accurate parameters of the machines including stator resistance, d- and q- axes inductances and the rotor flux linkages. Among these four parameters, stator resistance and rotor fluxing linkage do not change significantly during the operation; in contrast, d- and q- axes inductances are normally varied according to the variation of the load torque due to the saturation of the magnetic field [1]. So far, the techniques to identify machine parameters can be classified as offline and online. The offline methods are based on running of the rotor at a certain speed [2] or locking the rotor at a specific position [3], applying the test signals and then processing the current or voltage response to identify the machine parameters. These methods exhibit the weakness of requiring additional hardware for producing test signals and the mechanical systems to clamp or run the rotor shaft.

Received: 03 November 2023; Accepted: 13 March 2024.

Online methods in contrast have been proposed to estimate the machine parameters during the normal operation of the control system. Most of the existing online methods are based on the dynamic model of the machine on the synchronous reference frame (dq), and the utilization of advanced control theories, such as recursive least square [4-7], Kalman filters [8-10], model reference adaptive system [11-13], Adaline neural network [14, 15]. These methods are based on the measurement of the d- axis and q-axis stator current, rotor speed and the estimated d- and q- stator voltages. Normally, the phase voltages are noisy, pulsated and not available to calculate the d- and q- axes stator voltages. Therefore, these voltages are taken as output voltage of the corresponding d- and q- axes current controller in FOC algorithm [16]. However, due to the non-linearity of the voltage source inverter, there is a deviation of the measured and the actual d- and q- axes voltages. Consequently, the compensation of the non-linearity of the inverter must be implemented. The compensation scheme requires accurate information of the inverter including characteristics of the main switches and the freewheel diodes, which are not normally available in most of the commercial voltage source inverters. In addition, the delay of the inverter and the digital sampling also produce the error between the actual and the measured rotor position [17]. This hinders the compensation implementation and the application of the aforementioned methods. The method shown in [18] has shown the merits in identifying four machine parameters by using the feedforward neural network; however, the experimental verification has not been published.

In order to solve the challenges of the model based online methods, the authors in [19, 20] have presented a method to estimate the d- and q- axes inductances of the IPMSM based on the measurement of the slopes of the phase current, together with the DC bus voltage during excitation of every voltage and zero voltage vector in a pule width modulation (PWM) cycle. Although these approaches have shown high estimation accuracy, it requires high-bandwidth current sensors, high-speed analog to digital converter (ADC) and high-computational digital signal processors (DSPs), such as Field Programmable Gate Array (FPGA). This is still a challenge for the application of this method in the drive systems with low computational capability.

Therefore, this paper proposes a novel method to estimate the machine inductances in real-time and overcome the weakness of the existing online model-based methods due to the effect of noise and the non-linearity of the voltage source inverter. The proposed parameter estimation method is based on the combination of deep learning and recursive least square algorithm. The deep learning neural network model was trained offline using experimental data in order to compensate the measured d- and q- voltages. On the other hand, the recursive least square algorithm was utilized to estimate d- and q- axes inductances of the PMSM. The rest of this paper is organized as follows: the second section presents the details of the proposed online parameter identification method, while the third section presents the experimental validation of the proposed approach. Finally, the conclusion is presented in the fourth section.

2. Proposed online parameters identification method.

2.1. PMSM dynamic model

The dynamic model of the PMSM on the actual d-q reference frame can be expressed as followed:

$$\begin{aligned} v_d &= R_s i_d + L_d \frac{di_d}{dt} - \omega_{re} L_q i_q \\ v_q &= R_s i_q + L_q \frac{di_q}{dt} + \omega_{re}(L_d i_d + \psi_m) \end{aligned} \quad (1)$$

where $v_{d,q}$ and $i_{d,q}$ are the d- and q- axes stator voltage and current, respectively; $L_{d,q}$ are d- and q- axes inductances. ω_{re} is the actual electrical rotor speed; R_s and ψ_m are the stator winding resistance and the rotor flux linkage, respectively.

The dynamic model of the PMSM on the estimated d-q reference can be represented as [17]:

$$\begin{aligned} \hat{v}_d &= R_s \hat{\imath}_d + L_d \tfrac{d\hat{\imath}_d}{dt} - \hat{\omega}_{re} L_q \hat{\imath}_q + \hat{E}_{ex} sin\tilde{\theta}_{re} \\ \hat{v}_q &= R_s \hat{\imath}_q + L_q \tfrac{d\hat{\imath}_q}{dt} + \hat{\omega}_{re} L_d \hat{\imath}_d + \hat{E}_{ex} cos\tilde{\theta}_{re} \\ \hat{E}_{ex} &= \hat{\omega}_{re}\psi_m + \hat{\omega}_{re}(L_d - L_q)\hat{\imath}_d - (L_d - L_q)(\frac{d\hat{\imath}_q}{dt}) \end{aligned} \quad (2)$$

where the accent symbol "^" indicates the quantities on the estimated d-q reference frame $(\hat{d}, \hat{q})$; $\tilde{\theta}_{re} = \hat{\theta}_{re} - \theta_{re}$ is the error between the measured $(\hat{\theta}_{re})$ and the actual electrical rotor position (θ_{re}).

2.2. Non-linearity effect of the voltage source inverter

Usually, three phase voltages of the machine are not available for estimating the d- and q- axes stator voltages as shown in equation (2). Therefore, the reference d- and q- axes stator voltages as the output of the corresponding d- and q-axes current controllers are often used as the input of the conventional model-based control and parameter identification methods. However, due to the effect of the deadtime, the voltage drop on the main switches and free wheel diodes of the two level three phase inverter, there exists the deviation of the measured and the actual d- and q- axes voltages as followed [8]:

$$\begin{pmatrix} \Delta\hat{v}_d \\ \Delta\hat{v}_q \end{pmatrix} = U_{DB} P(\hat{\theta}_{re}) \big(\text{sign}(i_a), \text{sign}(i_b), \text{sign}(i_c)\big)^T \quad (3)$$

where:

$$\text{sign}(i_j) = \begin{cases} 1 \; if \; i_j \geq 0 \\ -1 \; if \; i_j < 0 \end{cases} \text{ with } j = a, b, c \quad (4)$$

$$P(\hat{\theta}_{re}) = \frac{2}{3}\begin{pmatrix} \cos(\hat{\theta}_{re}) & \cos(\hat{\theta}_{re} - 2\pi/3) & \cos(\hat{\theta}_{re} + 2\pi/3) \\ \sin(\hat{\theta}_{re}) & \sin(\hat{\theta}_{re} - 2\pi/3) & \sin(\hat{\theta}_{re} + 2\pi/3) \\ 1/2 & 1/2 & 1/2 \end{pmatrix} \quad (5)$$

$$U_{DB} = \frac{T_{DB} + T_{on} - T_{off}}{T_{PWM}}(V_{DC} - V_S + V_D) + \frac{V_S + V_D}{2} \quad (6)$$

where T_{DB}, T_{on}, T_{off} and T_{PWM} are the dead time of the voltage source inverter, turning on time, turning off time of the main switch and the PWM period, respectively; V_{DC} is the DC bus voltage; V_S and V_D are the voltage drop on the main switch and the free wheel diode, respectively.

By combining the effects of the position measurement error and the non-linearity of the inverter, the dynamic model of PMSM on the estimated d-q reference frame can be presented as follows:

$$\begin{aligned} \hat{v}_d^* + \Delta\hat{v}_d &= R_s\hat{\imath}_d + L_d\frac{d\hat{\imath}_d}{dt} - \hat{\omega}_{re}L_q\hat{\imath}_q + \hat{E}_{ex}sin\tilde{\theta}_{re} \\ \hat{v}_q^* + \Delta\hat{v}_q &= R_s\hat{\imath}_q + L_q\frac{d\hat{\imath}_q}{dt} + \hat{\omega}_{re}L_d\hat{\imath}_d + \\ &\quad + \hat{E}_{ex}\left(1 - 2\sin^2\left(0.5\tilde{\theta}_{re}\right)\right) \end{aligned} \tag{7}$$

where $\hat{v}_d^*$ and $\hat{v}_q^*$ are the measured voltages at the output of the d- and q- axes current controllers, respectively.

Define the compensated d-and q- axes stator voltages on the estimated d-q reference frame:

$$\begin{aligned} \hat{v}_{d,comp} &= \Delta\hat{v}_d - \hat{E}_{ex}sin\tilde{\theta}_{re} \\ \hat{v}_{q,comp} &= \Delta\hat{v}_q + 2\hat{E}_{ex}\sin^2\left(0.5\tilde{\theta}_{re}\right) \end{aligned} \tag{8}$$

Equations (7) can be rewritten as:

$$\begin{aligned} \hat{v}_d^* + \hat{v}_{d,comp} &= R_s\hat{\imath}_d + L_d\frac{d\hat{\imath}_d}{dt} - \hat{\omega}_{re}L_q\hat{\imath}_q \\ \hat{v}_q^* + \hat{v}_{q,comp} &= R_s\hat{\imath}_q + L_q\frac{d\hat{\imath}_q}{dt} + \hat{\omega}_{re}(L_d\hat{\imath}_d + \psi_m) \end{aligned} \tag{9}$$

2.3. Proposed method based on deep learning and RLS algorithms

The block diagram of the proposed deep learning and RLS based estimator and the control system is shown in figure 1. Field oriented control algorithm of the control system is implemented in the microcontroller. The reference operating speed (ω_r^*), parameters of the id and iq controllers are set in the "User interface" block on Matlab/Simulink. The output of the d- and q- axes current controllers ($\hat{v}_d^*, \hat{v}_q^*$), the measured d- and q- axes currents ($\hat{\imath}_d, \hat{\imath}_q$) and the measured electrical speed ($\hat{\omega}_{re}$) from the microcontroller are fed to the deep neural network model for training and predicting the compensated d- and q- axes voltages ($\hat{v}_{d,comp}, \hat{v}_{q,comp}$) in Matlab/Simulink. These compensated d- and q- axes voltages together with those signals from microcontrollers are sent to the RLS based estimator to identify the machine inductances ($L_{d,est}, L_{q,est}$).

The mathematical model of a RLS based estimator is:

$$y_k = \Phi_k^T x \tag{10}$$

where x is vector of the unknown parameters to be estimated; Φ_k and y_k denote the input and output of the system, respectively; k is the sample instant. The update rule for RLS is:

$$\begin{aligned} \hat{x}_{k+1} &= \hat{x}_k + G_{k+1}[y_{k+1} - \Phi_{k+1}^T\hat{x}_k] \\ G_{k+1} &= P_k\Phi_{k+1}^T\left[I\lambda + \Phi_{k+1}^T P_k\Phi_{k+1}\right]^{-1} \\ P_{k+1} &= (P_k - G_{k+1}\Phi_{k+1}^T P_k)/\lambda \end{aligned} \tag{11}$$

where I is the identity matrix; λ is the forgetting factor; G_k and P_k the gain and covariance matrices, respectively.

The RLS algorithm can be implemented to estimate d- and q-axes inductances, the corresponding model will be:

$$x = \begin{bmatrix} L_{q,est} \\ L_{d,est} \end{bmatrix}, \Phi = \begin{bmatrix} -\hat{\omega}_{re}\hat{\imath}_q & 0 \\ 0 & \hat{\omega}_{re}\hat{\imath}_d \end{bmatrix} \tag{12}$$

$$y = \begin{bmatrix} \hat{v}_d^* + \hat{v}_{d,comp} - R_s\hat{\imath}_d \\ \hat{v}_q^* + \hat{v}_{q,comp} - R_s\hat{\imath}_q - \psi_m\hat{\omega}_{re} \end{bmatrix} \tag{13}$$

As can be seen in equations (3), (6) and (8), the compensated d- and q- axes voltages ($\hat{v}_{d,comp}, \hat{v}_{q,comp}$) are nonlinearly dependent of the parameters of the voltage source inverter, such as voltage drop on the main switches and free-wheel diodes, which are normally not available. This paper proposed a feedforward neural network model to estimate the compensated d- and q- axes voltages ($\hat{v}_{d,comp}, \hat{v}_{q,comp}$) based on the output of the d- and q- axes current controllers ($\hat{v}_d^*, \hat{v}_q^*$), the measured d- and q- axes currents ($\hat{\imath}_d, \hat{\imath}_q$) and the measured electrical speed ($\hat{\omega}_{re}$). The mechanism of this approach is the non-linear mapping of five measured input variables from microcontroller with two output variables. Therefore, the offline training of the neural network must be implemented using the PMSM with known parameters including stator resistance, d- and q- axes inductances, and rotor flux linkage. These parameters are experimentally identified by using the offline standstill IEEE standard method shown in [3].

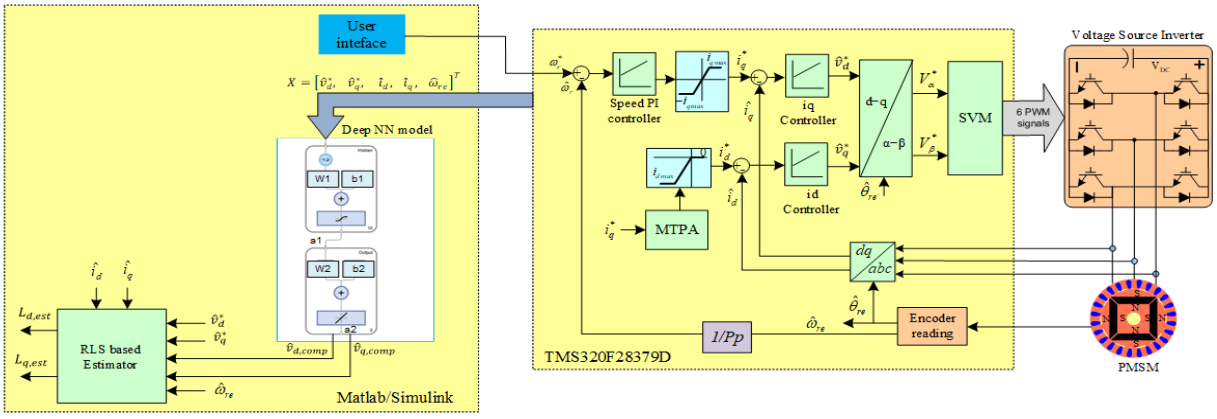

Figure 1: Block diagram of the proposed deep learning and RLS based estimator and control system.

As shown in (9), the output variables of the deep learning model can be calculated based on the measured input variables as follows:

$$\begin{aligned}\hat{v}_{d,comp}^{(training)} &= -\hat{v}_d^* + R_s\hat{\imath}_d + L_d\frac{d\hat{\imath}_d}{dt} - \hat{\omega}_{re}L_q \\ \hat{v}_{q,comp}^{(training)} &= -\hat{v}_q^* + R_s\hat{\imath}_q + L_q\frac{d\hat{\imath}_q}{dt} + \hat{\omega}_{re}(L_d\hat{\imath}_d + \psi_m)\end{aligned} \tag{14}$$

where $\hat{v}_{d,comp}^{(training)}$ and $\hat{v}_{q,comp}^{(training)}$ are compensated d- and q- axes voltages used to train to deep neural network model as the output variables.

The mathematic representation of every layer of the proposed feedforward neural network model shown in figure 1 is as follows:

$$\begin{aligned}a_1 &= tansig(W_1X + b_1) \\ a_2 &= purelin(W_2a_1 + b_2)\end{aligned} \tag{15}$$

where $X = \left[\hat{v}_d^*,\ \hat{v}_q^*,\ \hat{\imath}_d,\ \hat{\imath}_q,\ \hat{\omega}_{re}\right]^T$ is the input vector of the model; a_1, a_2 is the output of the hidden and output layer, respectively. a_2 is also the estimated compensated d- and q- axes stator voltages; W_1, b_1 and W_2, b_2 are weight, bias of the hidden and output layers, respectively.

The training data were collected by running the PMSM machine at different speeds from zero to rated value under different loading condition from no load to full load. The weight and bias metrices are updated using the Levenberg–Marquardt algorithm since this method can produce fast and stable convergence for the non-linear function [21]. The flow chart of the offline training process is presented in Figure 2 with the following steps [21].

- Step 1: Randomly initialize weights and bias matrices:

  $W_1[10\times 5], b_1[10\times 1], W_2[2\times 10], b_2[2\times 1].$

  In this study, the hidden layer was tested with a size of 10.

- Step 2: At every training epoch *k*, evaluate the mean square error (MSE) E_k.

$$E_k = \frac{1}{2}\sum_{i=1}^{2}\sum_{j=1}^{M} e_{ijk}^2 \tag{16}$$

$$e_{ijk} = a_{2,ijk} - \hat{a}_{2,ijk}$$

where M is the number of data set (70% of total data set); $\hat{a}_{2,ijk}$ is the output variable from the data set and calculated as shown in (14); $a_{2,ijk}$ is the estimated output variable from the neural network model as shown in (15).

- Step 3: Calculate the Jacobian matrices corresponding to weight and bias:

$$J_{W1,k} = \frac{\partial E_k}{\partial W_1} \qquad J_{W2,k} = \frac{\partial E_k}{\partial W_2}$$
$$J_{b1,k} = \frac{\partial E_k}{\partial b_1} \qquad J_{b2,k} = \frac{\partial E_k}{\partial b_2} \tag{17}$$

- Step 4: Update the weight and bias matrices.

$$\begin{aligned}W_{1,k+1} &= W_{1,k} - \left(J_{W1,k}^T J_{W1,k} + \mu I\right)J_{W1,k}e_k \\ W_{2,k+1} &= W_{2,k} - \left(J_{W2,k}^T J_{W2,k} + \mu I\right)J_{W2,k}e_k \\ b_{1,k+1} &= b_{1,k} - \left(J_{b1,k}^T J_{b1,k} + \mu I\right)J_{b1,k}e_k \\ b_{2,k+1} &= b_{2,k} - \left(J_{b2,k}^T J_{b2,k} + \mu I\right)J_{b2,k}e_k\end{aligned} \tag{18}$$

- Step 5: With the new weights and bias, evaluate the total error E_{k+1}.
- If the current total error is increased as a result of the update, then reset the weight and bias to the precious value) and increase combination coefficient μ by a factor of 10 and go back to step 4.
- If the current total error is decreased as a result of the update, then keep the new weight vector as the current one and decrease the combination coefficient μ by a factor of 10.
- Step 6: End the training if the total error is below the required value.

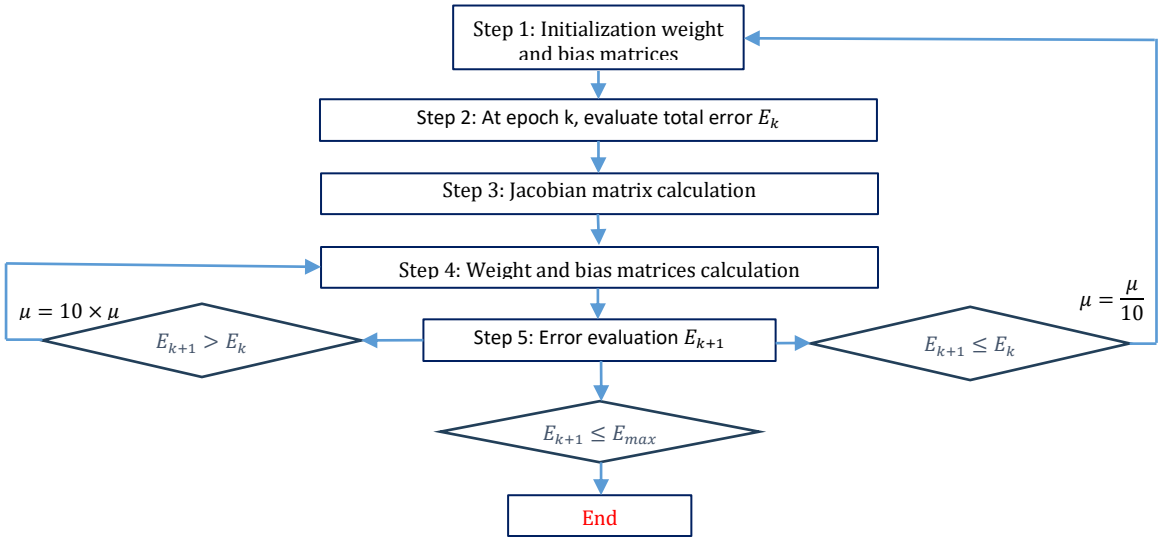

Figure 2: Flow chart of the offline training of the neural network for estimating the compensated d- and q- axes voltages.

3. Experimental validation

3.1 Experimental setup

The experimental setup is shown in figure 3. The tested PMSM's parameters are shown in Table I. The powder clutch ZKB0.6AN is used to load the tested PMSM. The three-phase two-level voltage source inverter, current sensing and DC voltage sensing circuits are integrated in the TI_IDDK_V2.2.1 evaluation module. The microcontroller TMS320F28379D-C2000-Delfino is used to implement the field-oriented control algorithm for the PMSM drive system. Matlab/Simulink and Code Composer Studio are used to compose and flash the program to the microcontroller. Matlab/Simulink are also used to implement the proposed parameter identification method, including the offline training and implementation of the deep neural network model for estimating the compensated d- and q- axes voltages, and realizing the RLS estimator for identifying machine inductances online.

Table1: Parameters of the teste PMSM (experiment)

Nominal Parameters	Value
L_d	0.0087 (H)
L_q	0.0087 (H)
ψ_m	0.063 (Wb)
R_s	2.25 (Ω)
Rated current (RMS)	2.7(A)
Rated torque	1.27 (Nm)
V_{DC}	300 (V)

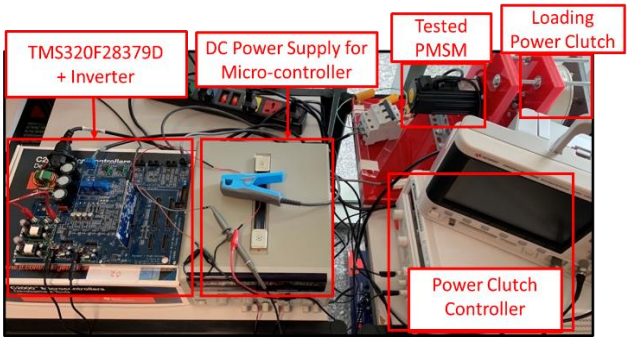

Figure 3: Experimental setup.

3.2 Offline training of the deep neural network using the experimental data

The feedforward neural network model for estimating the compensated d- and q- axes stator voltage was trained offline using the experimental data obtained by running the machine at different speed from zero to rated speed and loading conditions from no load to full load. The input and output data of 400000 samples are divided for the training, testing and validation by 70%, 15% and 15%, respectively. The hyper-parameters of the offline model training can be seen in Table II. The training statistic shown in figure 4 indicates that after 276 epochs, the mean square error (MSE) of the estimated and the actual compensated voltages is 0.0047. Further training accuracy can be achieved with larger training epochs.

Table 2: Hyper- Parameters of the offline training (experiment)

Parameter	Value
Size of hidden layers	10
Training Algorithm	Levenberg-Marquardt
μ	0.0001
Time delay	0.0001 (s)

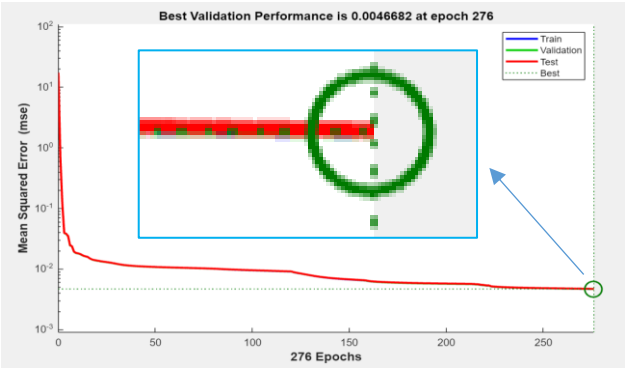

Figure 4. Training statistics of the neural network to estimate the compensated d-q axes stator voltage (experiment).

3.3. Experimental results

In order to evaluate the estimation accuracy and the robustness of the proposed parameter identification method against noise and effect of the non-linearity of the inverter, extensive experimental studies in various operation conditions of the control system were conducted. For the tested PMSM machine, the offline test shows that the machine inductances remain nearly unchanged over the loading range from no load to full load. Therefore, the armature reaction is negligible over the operating current range from zero to the rated value. Among all tested cases, the experimental results of the critical cases including the variation of the operating speed, load torque and field-weakening condition are presented as follows.

3.3.1. Variation of operating speeds

The performance of the proposed method under the variation of the operating speed is shown in figure 5. As can be seen in the first top subplot of figure 3, at time 4s the machine accelerates from 300 rpm to 1500 rpms, then decelerates to 900 rpm at time 8s. The measured d- and q-axes voltages (*vd meas* and *vq meas*) as the output of the corresponding id and iq current controllers in blue colors of the top second and third subplots vary according to the operating speeds. The compensation d- and q- axes voltages (*vd comp* and *vq comp*), which are sum of the compensated and the measured corresponding d- and q-axes voltages are shown in red color of the top second and third subplots. These compensation voltages also vary with the speeds and are deviated from the measured ones as the results of the proposed compensation scheme for the nonlinearity effect of the voltage source inverters. During the change of the operating speeds, the d-axis current was controlled at the value of -0.6A, and the light load was applied with q-axis current of 0.4A as can be seen in the subplot 4 and 5, respectively.

The comparison of the estimated (*Ld est* and *Lq est*) and the actual d- and q- axes inductances (*Ld actual* and *Lq actual*) are presented in subplot 6 and 7, respectively. It is clear that the estimated inductances follow closely with the actual ones of 8.7mH during the transient and steady states of the speed variations. The root mean square errors (RMSE) between the estimated and the actual d- and q- axes inductance over the whole period are 0.36 mH, 0.44 mH, respectively.

Discussion about the effect of the operation speed on the compensated d-axis voltage: Assume the expression of three phase currents as follows:

$$\begin{aligned} i_a &= I_m \cos(\hat{\theta}_{re}) \\ i_b &= I_m \cos(\hat{\theta}_{re} - \frac{2\pi}{3}) \\ i_c &= I_m \cos(\hat{\theta}_{re} + 2\pi/3) \end{aligned} \tag{19}$$

Assume the electric rotor angle $\hat{\theta}_{re}$ is between (0 to $\pi/3$), thus: $i_a > 0; i_b < 0; i_c > 0$

$$\rightarrow \left(\text{sign}(i_a), \text{sign}(i_b), \text{sign}(i_c)\right)^T = (1, -1, 1)^T \tag{20}$$

d- and q- axes voltage errors due to the inverter can be calculated as:

$$\begin{aligned} &\rightarrow \begin{pmatrix} \Delta\hat{v}_d \\ \Delta\hat{v}_q \end{pmatrix} \\ &= \frac{2}{3} U_{DB} \begin{pmatrix} \cos(\hat{\theta}_{re}) & \cos\left(\hat{\theta}_{re} - \frac{2\pi}{3}\right) & \cos\left(\hat{\theta}_{re} + \frac{2\pi}{3}\right) \\ \sin(\hat{\theta}_{re}) & \sin\left(\hat{\theta}_{re} - \frac{2\pi}{3}\right) & \sin\left(\hat{\theta}_{re} + \frac{2\pi}{3}\right) \\ \frac{1}{2} & \frac{1}{2} & \frac{1}{2} \end{pmatrix} \\ &\times \begin{pmatrix} 1 \\ -1 \\ 1 \end{pmatrix} \end{aligned} \tag{21}$$

$$\rightarrow \Delta\hat{v}_d = -\frac{4}{3} U_{DB} \cos\left(\hat{\theta}_{re} - \frac{2\pi}{3}\right) \tag{22}$$

Similarly, the d-axis voltage error can be calculated for other 60^o electric angle $\hat{\theta}_{re}$ between $\frac{\pi}{3}$ and 2π.

The average d-axis voltage error can be calculated as:

$$\begin{aligned} \Delta\bar{v}_d &= \frac{1}{\frac{\pi}{3}} \int_0^{\frac{\pi}{3}} -\frac{4}{3} U_{DB} \cos\left(\hat{\theta}_{re} - \frac{2\pi}{3}\right) \mathrm{d}(\hat{\theta}_{re}) \\ &= \frac{4\sqrt{3}}{\pi} U_{DB} \end{aligned} \tag{23}$$

If position measurement error ($\tilde{\theta}_{re}$) between the measured electric angle and the actual one is considered and $L_d = L_q$, the compensated d- axis voltage can be calculated as:

$$\hat{v}_{d,comp} = \Delta\hat{v}_d - \omega_{re}\psi_m sin\tilde{\theta}_{re} \tag{24}$$

Thus, the average compensated d-axis voltage can be calculated as:

$$\bar{v}_{d,comp} = \frac{4\sqrt{3}}{\pi} U_{DB} - \omega_{re}\psi_m sin\tilde{\theta}_{re} \tag{25}$$

It can be seen from equation (25) that the average compensated d-axis voltage $\bar{v}_{d,comp}$ is inversely proportional to the electrical speed ω_{re}. This can be verified by the experimental results shown in figure 5. To be specific, at the speed of 1500 rpm from 4 to 8s, the compensated d-axis voltage is about 0.5V, while at lower speed of 300 rpm from zero to 4s, the compensated d-axis voltage is much higher (about 3V). This explains why during the period from 0 to 4s, and from 4 to 8s the compensation d-axis voltage, which is the sum of the compensated and measured d-axis voltages, is relatively large compared to the measured one.

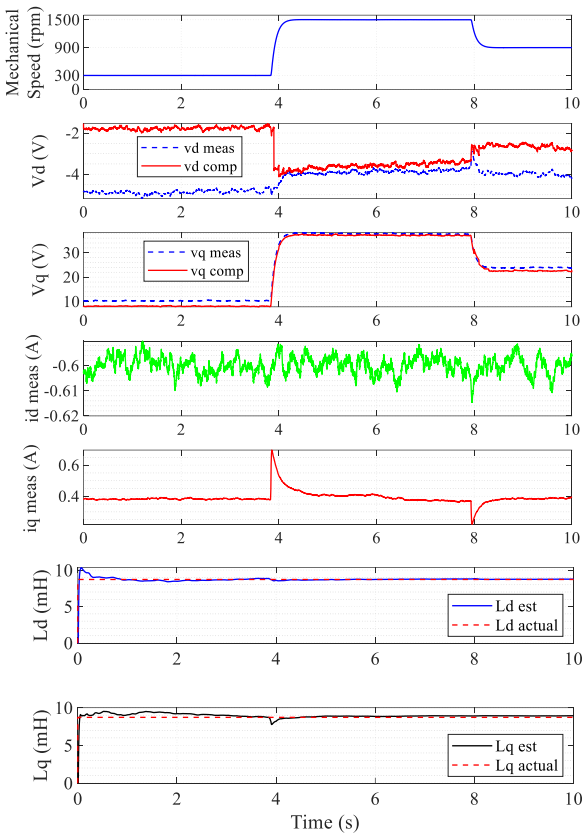

Figure 5. Estimation performance under the variation of the operating speeds (experiment).

3.3.2. Variation of load torque

The performance of the proposed methods with the variation of the load torque between light and full load under the operating speed of 300 rpm is shown in figure 6. The arrangement of the subplots of figure 6 is the same as for figure 5. As can be seen in the fifth subplot of figure 6, the load torque of the machine was changed between light to full loads at time 2s and 6.5s with the corresponding change of the q- axis current between 0.4A to 2.5A. It is worth mentioning that d-axis current is unchanged at -0.6A during the variation of the load torque as shown in the fourth subplot. As shown in the second and third subplots, the compensation d- and q- axes voltages are deviated from the measured d- and q- axes voltages as the results of the proposed compensation method.

The voltage difference between the measured and the computation vd is proportional to the operating current iq. This can be explained based on equations (6) and (25).

Equation (25) shows that the compensated vd ($\bar{v}_{d,comp}$) is proportional to U_{DB}. In addition, based on equation (6), U_{DB} is nearly proportional to the voltage drop on the main switch (V_S), since the term $\frac{T_{DB}+T_{on}-T_{off}}{T_{PWM}} \ll 0.5$. Furthermore, the V_S is nearly proportional to the operating current (iq) since the main switch (MOSFET) can be treated as a resistor.

It is clear in subplot 6 and 7 that the estimated inductances are closely matched with the actual ones of 8.7mH during the transient and steady states of the load torque variations. The RMSE between the estimated and the actual d- and q- axes inductances over the whole period are 0.51 mH, 0.64 mH respectively.

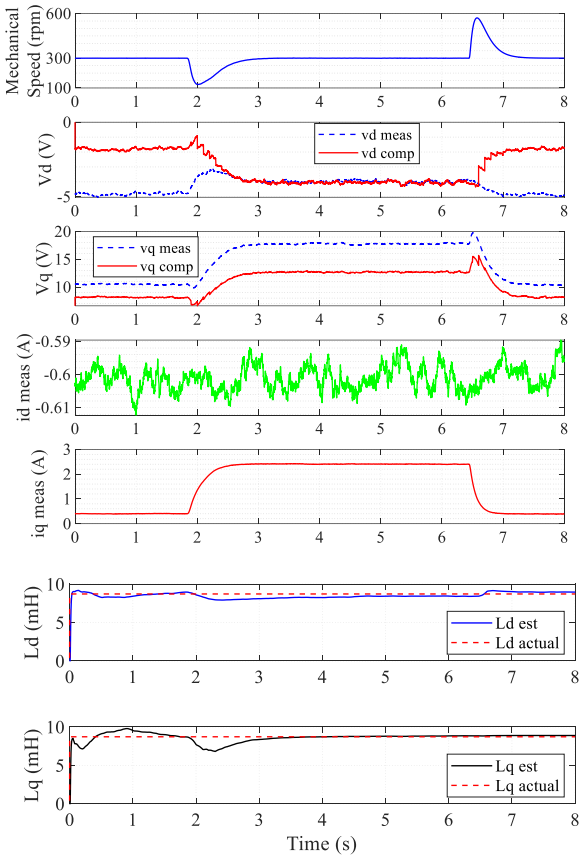

Figure 6. Estimation performance under the variation of the load torques (experiment).

3.3.3. Variation of field-weakening conditions

The performance of the proposed methods with the variation between light and heavy field-weakening condition under the operating speed of 300 rpm is shown in figure 7. As can be seen in the fourth subplot of the figure 6, at time 7.8s, the field-weakening was changed from light to heavy condition with the d-axis current change from -0.6A to -1.8A. As a result, the operating drops from 300 rpm to about 270 rpms as shown in the first subplot and the q-axis current is slightly increased from 0.4A to 0.6A. Subplots 2 and 3 also show the deviation of the measured and the compensation d- and q- axes voltages as the results of the proposed compensation scheme.

Subplots 6 and 7 clearly demonstrate that the estimated inductances are closely matched with the actual ones of 8.7mH during the transient and steady states of the field weakening variations. The RMSE between the estimated and the actual d- and q- axes inductances over the whole period are 0.39 mH, 0.68 mH respectively.

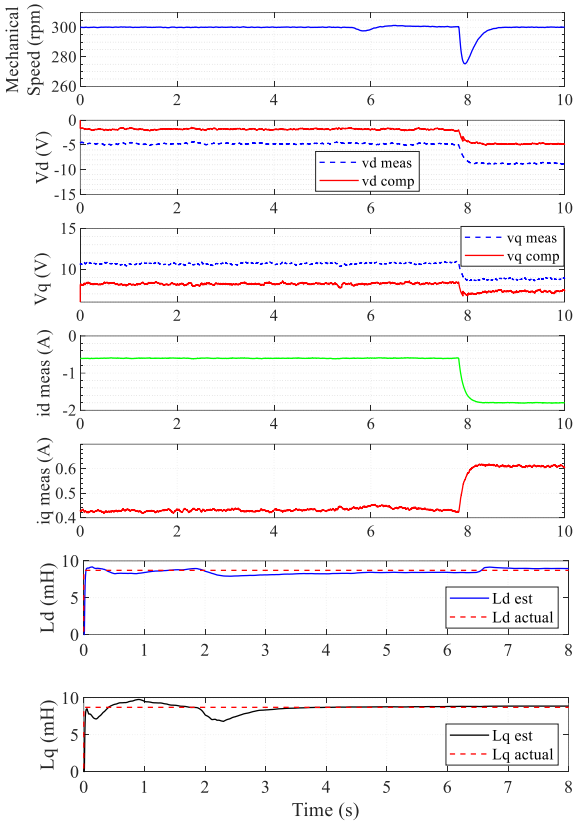

Figure 7. Estimation performance under the variation of the field-weakening conditions (experiment).

3.3.4. Comparison with conventional RLS-based method.

The comparison of the proposed method and the RLS-based method shown in [4] in terms of estimation accuracy was implemented by running the machine at the speed of 1500 rpm under light load condition. The experimental results of this study are shown in figure 8. The top subplot of the figure shows the measured operation mechanical speed around 1500 rpm. The second and third top subplots show the measured d- and q- voltages (*vd meas, vq meas*) in blue and the compensation d- and q- axes voltages (*vd comp, vq comp*) in red, which are the sum of the measured and the compensated ones. The fourth and fifth subplots present the operating d- and q- axes currents, respectively. Finally, the last two subplots present the actual inductances (*Ld actual, Lq actual*) in red, estimated inductances by the proposed method (*Ld est proposed, Lq est proposed*) in blue and the estimated inductances of the conventional RLS based method (*Ld est uncomp, Lq est uncomp*) in green.

It is obvious that the proposed method produces higher accuracy compared to the RLS based method. Specifically, the RMSE between the estimated and the actual d- axis inductances over the whole period of the proposed method

is 0.4 mH, while the RMSE of the RLS-based method was significantly higher (2.85 mH). Similarly, the RMSE between the estimated and the actual q- axis inductances over the whole period of the proposed method is 0.38 mH, while the RMSE of the RLS based method was higher (0.44 mH). The better estimation accuracy of the proposed method compared to the RLS-based method is due to the fact that the proposed method accurately compensates for the voltage errors caused by the voltage source inverter. In contrast, the RLS-based method does not consider the non-linearity effect of the inverter and it is only robust when the non-linearity effect of the inverter is negligible.

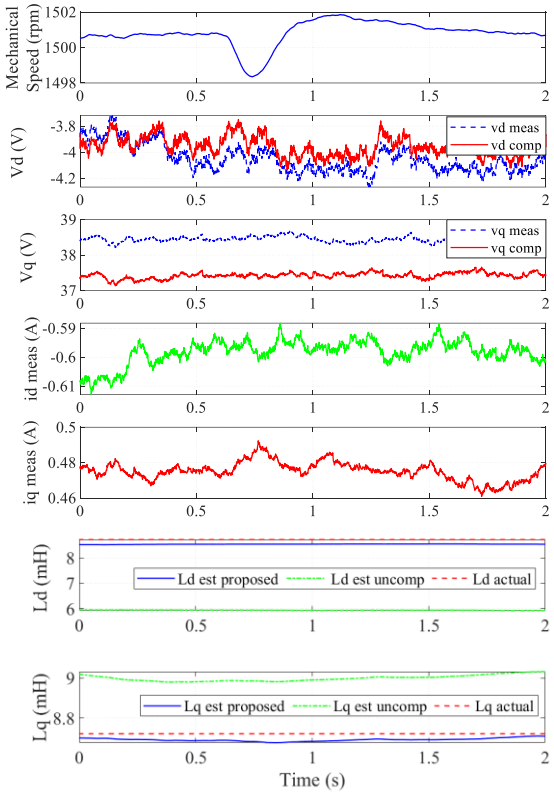

Figure 8. Performance comparison of the proposed and the uncompensated methods shown in [4] (experiment).

4. Conclusion

This paper has presented a novel approach to identify in real time d- and q- axes inductances of the PMSM based on the combination of deep learning and recursive least square algorithms. The deep learning model was proposed and trained offline using the experimental data to compensate the non-linearity of the voltage source inverter and the position measurement error, while the recursive least square algorithm was utilized to estimate d- and q- axes inductances based on the measured d- and q-axes currents, compensation d- and q- axes voltages and the operating speed. The proposed method overcomes challenges of the existing model-based estimators known as the effect of position measurement error and the requirement of accurate information of the inverter. The experimental results have demonstrated high estimation accuracy and the robustness of the proposed technique under various operating conditions including the variation of operating speed, load torque and field-weakening conditions. The experimental results also demonstrate the superiority of the proposed method, compared to the conventional RLS-based one.

Acknowledgement

This work was partly supported by the Nafosted Vietnam under the grant 107.99-2019.341.

References

[1] B. Ding, K. Huang, C. Lai, and G. Feng, "Correlated Inductance Modeling and Estimation of Permanent Magnet Synchronous Machines Considering Magnetic Saturation," *IEEE Transactions on Power Electronics*, vol. 38, no. 11, pp. 14463-14474, 2023, doi: 10.1109/TPEL.2023.3307715.

[2] *Rotating Electrical Machines Part 4: Methods for Determining Synchronous Machine Quantities From Tests*, IEC60034-4, 2008.

[3] "IEEE Guide for Test Procedures for Synchronous Machines Part I—Acceptance and Performance Testing Part II—Test Procedures and Parameter Determination for Dynamic Analysis - Redline," *IEEE Std 115-2009 (Revision of IEEE Std 115-1995) - Redline*, pp. 1-219, 2010, doi: 10.1109/IEEESTD.2010.5953453.

[4] S. J. Underwood and I. Husain, "Online Parameter Estimation and Adaptive Control of Permanent-Magnet Synchronous Machines," *IEEE Transactions on Industrial Electronics*, vol. 57, no. 7, pp. 2435-2443, 2010, doi: 10.1109/TIE.2009.2036029.

[5] S. Morimoto, M. Sanada, and Y. Takeda, "Mechanical Sensorless Drives of IPMSM With Online Parameter Identification," *IEEE Transactions on Industry Applications*, vol. 42, no. 5, pp. 1241-1248, 2006, doi: 10.1109/TIA.2006.880840.

[6] Y. Inoue, Y. Kawaguchi, S. Morimoto, and M. Sanada, "Performance Improvement of Sensorless IPMSM Drives in a Low-Speed Region Using Online Parameter Identification," *IEEE Transactions on Industry Applications*, vol. 47, no. 2, pp. 798-804, 2011, doi: 10.1109/TIA.2010.2101994.

[7] C. Lian, F. Xiao, J. Liu, and S. Gao, "Parameter and VSI Nonlinearity Hybrid Estimation for PMSM Drives Based on Recursive Least Square," *IEEE Transactions on Transportation Electrification*, vol. 9, no. 2, pp. 2195-2206, 2023, doi: 10.1109/TTE.2022.3206606.

[8] X. Li and R. Kennel, "General Formulation of Kalman-Filter-Based Online Parameter Identification Methods for VSI-Fed PMSM," *IEEE Transactions on Industrial Electronics*, vol. 68, no. 4, pp. 2856-2864, 2021, doi: 10.1109/TIE.2020.2977568.

[9] Y. Shi, K. Sun, L. Huang, and Y. Li, "Online Identification of Permanent Magnet Flux Based on Extended Kalman Filter for IPMSM Drive With Position Sensorless Control," *IEEE Transactions on Industrial Electronics*, vol. 59, no. 11, pp. 4169-4178, 2012, doi: 10.1109/TIE.2011.2168792.

[10] X. Xiao, C. Chen, and M. Zhang, "Dynamic Permanent Magnet Flux Estimation of Permanent Magnet Synchronous Machines," *IEEE Transactions on Applied Superconductivity*, vol. 20, no. 3, pp. 1085-1088, 2010, doi: 10.1109/TASC.2010.2041435.

[11] K. Liu, Z. Q. Zhu, Q. Zhang, and J. Zhang, "Influence of Nonideal Voltage Measurement on Parameter Estimation in Permanent-Magnet Synchronous Machines," *IEEE Transactions on Industrial Electronics*, vol. 59, no. 6, pp. 2438-2447, 2012, doi: 10.1109/TIE.2011.2162214.

[12] T. Boileau, N. Leboeuf, B. Nahid-Mobarakeh, and F. Meibody-Tabar, "Online Identification of PMSM Parameters: Parameter Identifiability and Estimator Comparative Study," *IEEE Transactions on Industry Applications*, vol. 47, no. 4, pp. 1944-1957, 2011, doi: 10.1109/TIA.2011.2155010.

[13] X. Yao, S. Huang, J. Wang, H. Ma, G. Zhang, and Y. Wang, "Improved ROGI-FLL-Based Sensorless Model Predictive Current Control With MRAS Parameter Identification for SPMSM Drives," *IEEE Journal of Emerging and Selected Topics in Power Electronics*, vol. 11, no. 2, pp. 1684-1695, 2023, doi: 10.1109/JESTPE.2022.3230700.

[14] K. Liu and Z. Q. Zhu, "Position-Offset-Based Parameter Estimation Using the Adaline NN for Condition Monitoring of

Permanent-Magnet Synchronous Machines," *IEEE Transactions on Industrial Electronics*, vol. 62, no. 4, pp. 2372-2383, 2015, doi: 10.1109/TIE.2014.2360145.

[15] Z. Wang, J. Chai, X. Xiang, X. Sun, and H. Lu, "A Novel Online Parameter Identification Algorithm Designed for Deadbeat Current Control of the Permanent-Magnet Synchronous Motor," *IEEE Transactions on Industry Applications*, vol. 58, no. 2, pp. 2029-2041, 2022, doi: 10.1109/TIA.2021.3136807.

[16] Z. Q. Zhu, D. Liang, and K. Liu, "Online Parameter Estimation for Permanent Magnet Synchronous Machines: An Overview," *IEEE Access*, vol. 9, pp. 59059-59084, 2021, doi: 10.1109/ACCESS.2021.3072959.

[17] K. Choi, Y. Kim, S. K. Kim, and K. S. Kim, "Auto-calibration of position offset for PMSM drives with uncertain parameters," *Electronics Letters*, vol. 56, no. 20, pp. 1048-1051, 2020/09/01 2020, doi: 10.1049/el.2020.1669

[18] M. X. Bui, "Online Parameter Identification Method using Neural Network for IPMSM," in *2022 25th International Conference on Electrical Machines and Systems (ICEMS)*, 29 Nov.-2 Dec. 2022 2022, pp. 1-6, doi: 10.1109/ICEMS56177.2022.9983070.

[19] M. X. Bui, D. Xiao, and M. F. Rahman, "Sensorless Control and Inductances Estimation of IPMSMs Using FPGA and High Bandwidth Current Measurement," *IEEE Access*, vol. 11, pp. 67322-67329, 2023, doi: 10.1109/ACCESS.2023.3287220.

[20] M. X. Bui, M. F. Rahman, D. Guan, and D. Xiao, "A New and Fast Method for On-line Estimation of d and q Axes Inductances of Interior Permanent Magnet Synchronous Machines Using Measurements of Current Derivatives and Inverter DC-Bus Voltage," *IEEE Transactions on Industrial Electronics*, vol. 66, no. 10, pp. 7488-7497, 2019, doi: 10.1109/TIE.2018.2883274.

[21] H. Yu and B. M. Wilamowski, "Levenberg–marquardt training," in *Intelligent systems*: CRC Press, 2018, pp. 12-1-12-16.

Vol 5 (1) (2024)

Measurement, Control, and Automation

Website: https:// mca-journal.org

ISSN 1859-0551

Vibration Suppression Control for Overhead Crane using Inverse Notch Filter

Do Trong Hieu[1,*], Nguyen Cong Minh[1], Duong Minh Duc[1]

[1]*School of Electrical and Electronic Engineering, Hanoi University of Science and Technology*
[*]*Corresponding author E-mail: hieu.dotrong@hust.edu.vn*

Abstract

Overhead cranes play an important role in many fields such as industry, transportation, etc. However, payload vibration is a common issue that can occur with overhead cranes. To overcome this problem, various control approaches have been applied including feedforward and feedback control approaches. One practical approach is feedforward control where the controller works as a filter to eliminate the vibration. The use of filter can exist in three structures including: the filter is outside the trolley position control loop, in the feedforward path of the trolley position control loop, and in the feedback path of the trolley position control loop. In this paper, the inverse Notch filter in the feedback path of the trolley position control loop is considered as a vibration suppression controller for the overhead crane. This proposed controller can suppress vibration caused by both reference trolley position input and disturbance in the feedback loop. The effectiveness of the proposed controller is verified via simulation and experiments.

Keywords*: Inverse Notch Filter, Overhead Crane, Vibration Suppression Control, Feedforward Control,*

Symbols

Symbols	Description
M, m, l	Overhead crane parameters
S(s), C(s), G(s), F(s)	Transfer function
w, d, θ	System variables

Abbreviations

IS	Input Shaping
PID	Proportional–Integral–Derivative
ADRC	Active Disturbance Rejection Control

1. Introduction

Overhead cranes play an important role in industry and construction transportation, etc., especially in lifting, transporting, and unloading heavy and bulky materials [1]. However, one of the main natural problems of overhead cranes is the fluctuation of payload during operation. The payload fluctuations cause insecurity for surrounding people and equipment, reducing working accuracy, especially when working at high speed. To avoid these problems, many researchers have developed various methods to control the crane system to move the payload to the desired location while minimizing payload fluctuations. These control methods can mainly be separated into open-loop control and closed-loop control techniques.

Closed-loop control techniques, also known as feedback control, will measure and evaluate system states to minimize the oscillation angle and bring the payload to the desired position accurately. There are many control strategies that have been proposed for crane systems such as linear control [2-5], optimal control [6-8], adaptive control [9-12], sliding control [13-16], intelligent control [17-22], etc. The closed-loop control method has the advantage of being resistant to disturbances and uncertain parameters. However, the main disadvantage of this method is the need for sensors to measure the vibration angle. This increases the cost and complexity of the system. Therefore, the feedback control method has limited application in practice.

The dynamical model of an overhead crane is similar to the pendulum model, thus information about payload fluctuations can be known more or less in advance. Therefore, we can apply some feedforward control techniques to modify the input with the goal of eliminating payload oscillations. There are three main feedforward control techniques widely used for crane control including Input Shaping (IS) [23-26], filtering [27-29], and signal smoothing [30-32]. The feedforward control method is quite effective and is widely used to limit crane payload fluctuations because it is easy to implement and does not require a sensor to measure the angle of payload fluctuation.

The feedforward controller can exist in three structures including the filter is outside the trolley position control loop, in the feedforward path of the trolley position control loop [23], and in the feedback path of the trolley position control loop [33] as shown in Figure 2. Among these three structures, only the third structure where the filter is in the feedback path of the trolley position control loop can suppress the vibration cause by both reference position input of the trolley and disturbance inside the trolley position control loop [33].

In this paper, we apply the feedforward control structure where the filter is in the feedback path of the trolley position

Received: 27 December 2023; Accepted: 15 March 2024.

control loop to suppress the payload vibration of an overhead crane. Difference from [33] where the inverse input shaper that is non casual is used, in this paper inverse Notch filter is applied [34,35]. The inverse Notch filter can suppress the vibration caused by both reference position input of the trolley and disturbance inside the trolley position control loop. In addition, Notch filter is a casual component, thus the system become more stable, in comparison to a system with non-casual component.

The rest of the paper is organized as follows. In section 2, the mathematical model of an overhead crane is described. The analysis of three feedforward control structures for vibration suppression control is discussed in section 3. Section 4 presents the simulation/experimental results of the proposed controller. The conclusion and future study are presented in section 5.

2. Overhead Crane Model

Figure 1 describes a simple crane model with the trolley moving in the X direction and the payload being released in the Y direction. In this figure, F_x is the force acting on the trolley, f_{cx} is the friction force of the moving trolley. $f_{c\theta}$ is the friction force of the moving payload, P is the force of gravity, $x(t)$ is the position of the trolley, l is the length of the rope, m is the mass of the payload, M is the mass of the trolley, and θ(t) is the angle between the rope and the vertical axis (Y axis) - which is the oscillation angle. According to [16], the linearized model of the crane can be described as follows:

$$F_x = (M+m)\ddot{x} + b_x\dot{x} + ml\ddot{\theta} \quad (1)$$

$$-\ddot{x} = l\ddot{\theta} + b_\theta\dot{\theta} + g\theta \quad (2)$$

where b_x and b_θ are the friction coefficients of the trolley and the payload, respectively. Equation (1) describes the relationship between the force acting on the trolley and the trolley position, where the oscillation angle acts as a disturbance signal that affects the control of the trolley position. Equation (2) describes the influence of the motion of the trolley on the payload fluctuation. In fact, the trolley is controlled by a motor with a motor controller that allows us to control the trolley speed accurately and eliminate external disturbances.

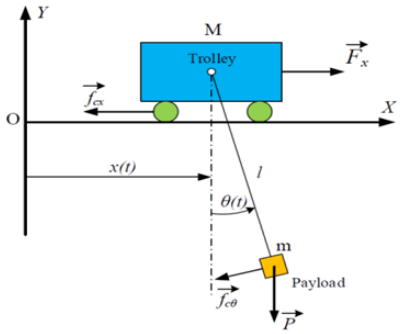

Figure 1: Overhead crane model

Therefore, to design the trolley position controller, instead of using model (1), we will use the motor model with the motor controller as follows [36]:

$$G(s) = \frac{X(s)}{U(s)} = \frac{K_c}{(T_c s+1)s} \quad (3)$$

where $U(s)$ is the Laplace transform of the control voltage signal $u(t)$, $X(s)$ is the Laplace transform of the trolley position $x(t)$, K_c is the amplification coefficient, and T_c is the system time constant.

In practice, the amplification coefficient K_c, and the system time constant T_c are determined by model identification process.

3. Control of overhead crane

3.1. Feedforward control structures

Crane control is to move the payload to the desired position. However, we cannot move the payload directly to the desired position. Instead, we will move the trolley to the desired position and if there is no vibration, the payload will reach the desired position. According to equation (2), the motion of the trolley causes payload fluctuations. Therefore, two tasks must be done, including controlling the trolley to the desired position and at the same time suppressing the oscillations of the payload as quickly as possible. To control the trolley position, a PD position controller will be used for the object in equation (3). Additionally, to suppress payload oscillations, a filter is used. There are three control structures as shown in Figure 2. In these structures, w is reference input or reference trolley position, d is disturbance to the system, and θ is payload angle. We will analyze the effect of filter $S(s)$ in suppression of vibration caused by reference input and disturbance.

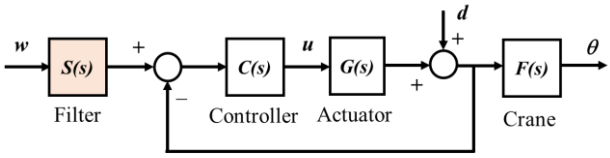

(a) Control structure with the filter is outside the position control loop

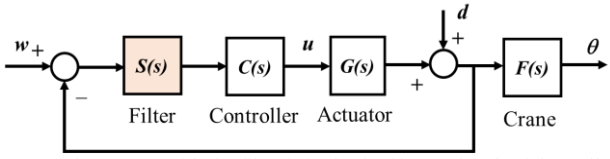

(b) Control structure with the filter is in the feedforward path of the trolley's position control loop

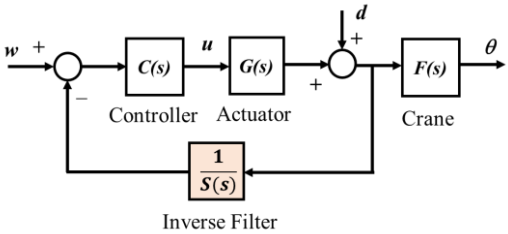

(c) Control structure with the inverse filter is in the feedback path of the trolley's position control loop

Figure 2: Three vibration suppression control structures for overhead crane

In the first structure, as shown in Figure 2a, the filter $S(s)$ is outside the position control loop and plays a role suppress the payload's vibration. The feedback controller $C(s)$ guarantees the precise positioning for the trolley. The advantage of this structure is that the control design process is simple, and we

can design the filter and the feedback controller independently.

However, the filter must be chosen carefully so that there is no steady state error between the signals before and after the filter. The main disadvantage of this structure is that the vibration caused by disturbance cannot be suppressed.

Let us consider the transfer function from input *w* and disturbance *d* to the output θ as follows:

$$\frac{\Theta(s)}{W(s)} = \frac{S(s)C(s)G(s)F(s)}{1+C(s)G(s)} \quad (4)$$

$$\frac{\Theta(s)}{d(s)} = \frac{F(s)}{1+C(s)G(s)} \quad (5)$$

From equation (4), it is clear that the zeros of the filter *S(s)* can be assigned to cancel the oscillatory modes of crane *F(s)* given by (2), i.e. the filter can suppress the vibration of the crane. However, *S(s)* does not appear in the transfer function from disturbance *d* to payload angle θ as shown in equation (5). Therefore, *S(s)* cannot cancel the oscillation caused by disturbance.

In the second structure, as shown in Figure 2b, the filter $S(s)$ is in the feedforward path of the position control loop. The feedback controller $C(s)$ guarantees the precise positioning for the trolley. The feedback control design process is quite complicated since the filter is in the loop. However, the steady-state error can be avoided. As same as the first structure, the main disadvantage of this structure is that the vibration caused by disturbance cannot be suppressed. Let us consider the transfer function from input *w* and disturbance *d* to the output θ as follows:

$$\frac{\Theta(s)}{W(s)} = \frac{S(s)C(s)G(s)F(s)}{1+S(s)C(s)G(s)} \quad (6)$$

$$\frac{\Theta(s)}{d(s)} = \frac{F(s)}{1+S(s)C(s)G(s)} \quad (7)$$

As shown in equation (6), it is clear that the zeros of the filter *S(s)* can cancel the oscillatory modes of crane *F(s)* given by (2), i.e. the filter can suppress the vibration of the crane. However, in equation (7), $S(s)$ cannot cancel the oscillation modes of crane $F(s)$ caused by disturbance.

In the third structure, as shown in Figure 2c, the inverse filter $1/S(s)$ is in the feedback path of the position control loop. The feedback controller $C(s)$ guarantees the precise positioning for the trolley. The feedback control design process is quite complicated since the inverse filter is in the loop. However, the steady state error can be avoided. The main advantage of this structure is that the vibration caused by both reference input and disturbance can be suppressed. Let us consider the transfer function from input *w* and disturbance *d* to the output θ as follows:

$$\frac{\Theta(s)}{W(s)} = \frac{S(s)C(s)G(s)F(s)}{S(s)+C(s)G(s)} \quad (8)$$

$$\frac{\Theta(s)}{d(s)} = \frac{S(s)F(s)}{S(s)+C(s)G(s)} \quad (9)$$

From equation (8) and (9), it is clear that the zeros of the filter $S(s)$ can be assigned to cancel the oscillatory modes of crane $F(s)$ given by (2), i.e. the filter can suppress the vibration of the crane.

From this analysis, we choose the third structure for control of the overhead crane. However, inverse of the popular filters *S(s)* such as input shapers are non-casual. The non-casual filter may not be realizable and therefore the approximation must be used. To avoid this problem, the casual inverse filter should be chosen. In this paper, we propose to use Notch filter as the filter *S(s)* to suppress the vibration. The Notch filter and its inverse are casual and can be realizable in practice.

After choosing the inverse filter $1/S(s)$, we can design the controller *C(s)* as PID controller that stabilizes the system and guarantees good position tracking. We have the models of components for the overhead control system as in Figure 2c as follows:

- The PID feedback controller: $C(s) = K_P + \frac{K_I}{s} + K_D s$
- The actuator (motor and driver): $G(s) = \frac{K_c}{(T_c s+1)s}$
- The Notch filter: $S(s) = \frac{s^2+2\omega_0 Ds+\omega_0^2}{s^2+2\omega_0 DK_n s+\omega_0^2}$, where ω_0 is filter frequency, D is damping ratio, and K_n is coefficient to control the depth and width of the filter.
- Crane vibration model: $F(s) = \frac{s^2}{ls^2+b_\theta s+g}$

3.2. Control design

From equation (9), to suppress the the payload vibration, zeros of *S(s)* have to cancel the poles of *F(s)*. This leads to the parameters ω_0 and *D* of the Notch filter is calculated as

$$\omega_0 = \sqrt{\frac{g}{l}} \qquad D = \frac{b_\theta}{2\sqrt{gl}} \quad (10)$$

The parameters K_P, K_I, K_D of controller *C(s)* and coefficient K_n of the Notch filter is chosen such as the following polynomial *P(s)* is Hurwitz:

$$P(s) = s^2(s^2 + 2\omega_0 DK_n s + \omega_0^2)(T_c s + 1) + \mathrm{K_c}(K_D s^2 + K_P s + K_I)(s^2 + 2\omega_0 Ds + \omega_0^2) \quad (11)$$

4. Simulation and Experimental Results

To validate the proposed control structure, simulations and experiments have been done. The experiment apparatus is shown in Figure 3.

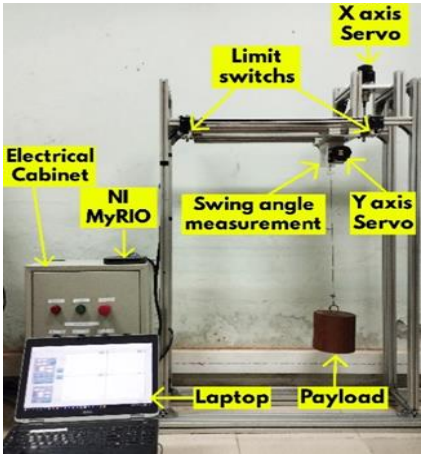

Figure 3: Experimental overhead crane system

The system parameters are identified and set as in Table 1. The parameters in Table 1 are used for simulations and experiments.

Table 1: System and controller parameters

Parameter	**Value**
Crane parameters	
Actuator gain (K_c)	30 [cm/s/V]
Actuator time constant (T_c)	3 [s]
Rope length (l)	0.4 [m]
Gravitational acceleration (g)	9.81 [m/s^2]
Notch filter	
Frequency (ω_0)	4.9 [rad/s]
Damping ratio (D)	0.017
K_n	35
PID controller	
K_P	0.713
K_I	0.001
K_D	0.835

4.1. Simulation results

Three simulations have been conducted for the proposed controller. The simulation of overhead crane control using PID position control for trolley and input shaper for vibration suppression control have also been conducted to compare with the proposed controller.

In the first simulation, the proposed control system is simulated with step input. The results are compared to the response of the overhead crane system using PID controller for trolley position without any filter for vibration suppression. As shown in Figure 4, the proposed control system can suppress the payload vibration significantly right after the trolley gets to the destination. The precise position tracking of the trolley is guaranteed with fast response time, in comparison to PID controller. The PID controller for trolley alone cannot suppress the payload vibration.

In the second case, a step signal with a magnitude of 5 is added to the system at time t = 6s for 1 second as a disturbance. As shown in Figure 5, for both controllers, the trolley moves out of the stable position when the disturbance appears. Then the trolley returns to the reference position when the disturbance disappears. However, the proposed controller can suppress the vibration caused by both reference input and disturbance. There is a little fluctuation when the disturbance appears, but it is then suppressed by the filter.

In the third simulation, the proposed controller is compared to the overhead control system using PID controller as trolley position controller and input shaper outside the trolley position control loop as vibration filter. In this case, at t = 6, a step signal with a magnitude of 5 is applied to the system and remains constant thereafter, which is considered as a system disturbance. As shown in Figure 6, at the trolley moving period without disturbance, the response of the input shaper is better than the proposed controller with smaller vibration magnitude. When there is a disturbance, the proposed controller can still suppress the vibration. However, with the input shaper, the vibration appears when there is a disturbance, and it cannot be suppressed. Note that the position controller takes a long time to return the trolley to set-point position.

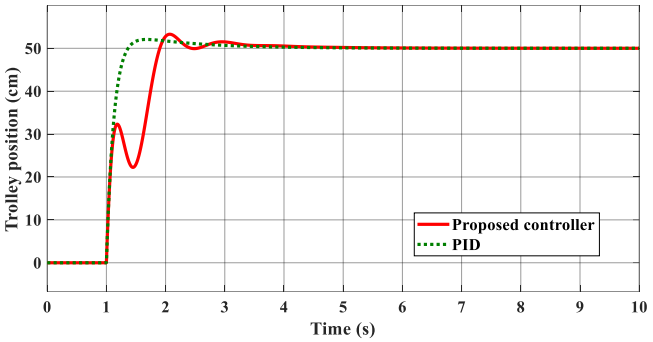

(a) Trolley position

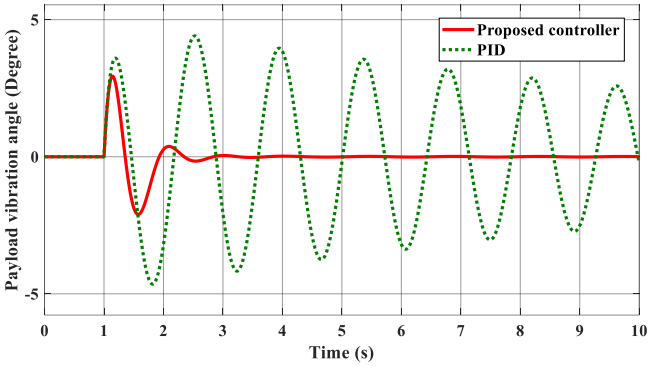

(b) Payload vibration angle

Figure 4: Comparison of the control system using only PID controller with the proposed control for overhead crane in the case of without disturbance

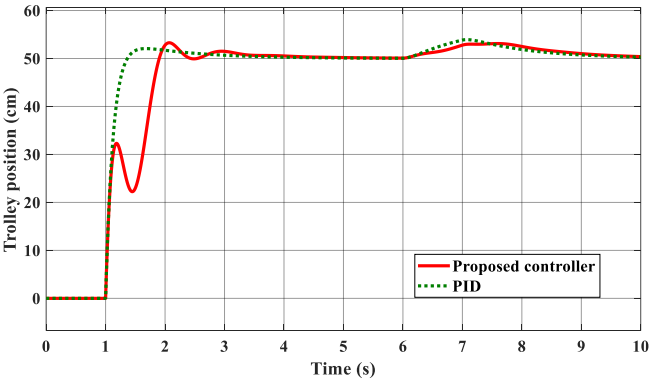

(a) Trolly position

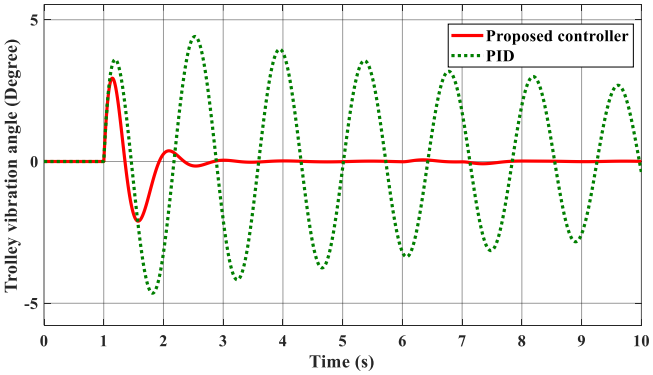

(b) Payload vibration angle

Figure 5: Comparison of the control system using only PID controller with the proposed control for overhead crane in present of disturbance

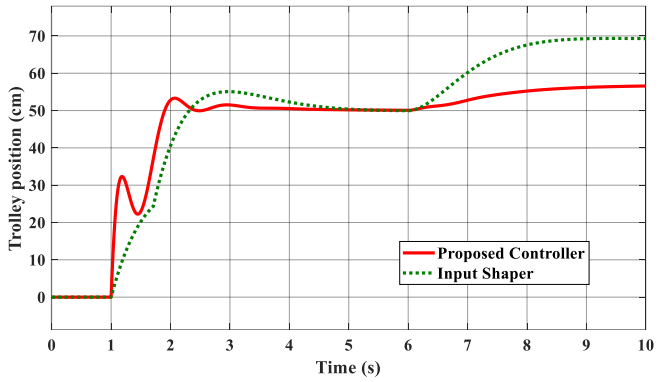

(a) Trolley position

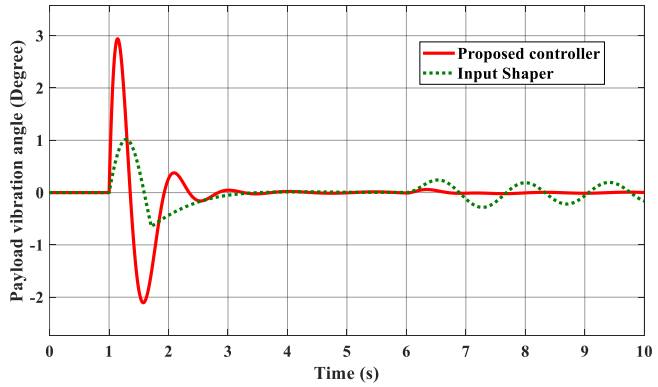

(b) Payload vibration angle

Figure 6: Comparison of the input shaper and the proposed control for overhead crane in the present of disturbance

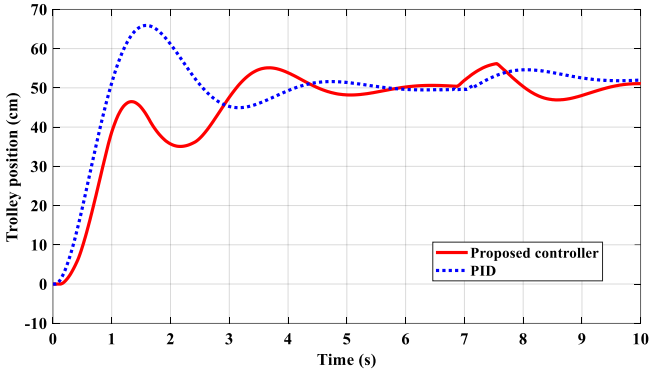

(a) Trolley position

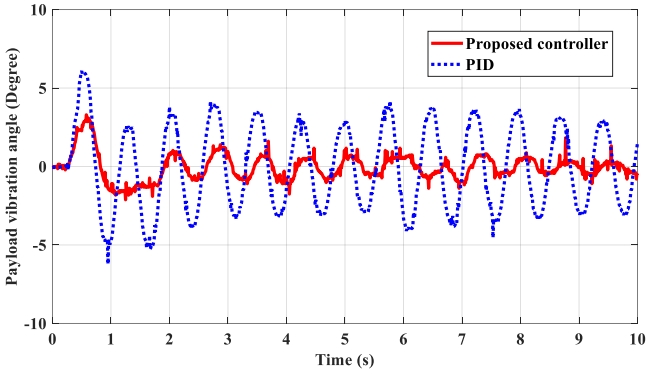

(b) Payload vibration angle

Figure 7: Experimental results of PID and the proposed control for overhead crane in the present of disturbance

4.2. Experimental results

To confirm that the proposed control can be applied to the practical system, an experiment of overhead crane control has been conducted. Similar to simulation case, the step input is applied to the system. The experiment of overhead crane with PID controller has also been conducted to compare with the proposed controller.

The experiment results are shown in Figure 7. With the same simulation parameters, the performance of the practical system is reduced, the transition time is longer with higher overshoot. However, the system is still stable and with small steady state errors (1% for PID Controller and 2% for proposed controller). The payload vibration angle in the case of PID controller is quite high. The maximum vibration angle is 6 degrees at transient period and 4 degrees at steady state period. While in the case of the proposed controller, the payload vibration angle is significantly reduced. The maximum vibration angle is 3 degrees at transient period and 1 degree at steady state period.

When a disturbance appears (a voltage with a value of 0.75V is added to the system at time t = 7 for a period of about 1 second), in the case of PID controller, since the payload vibration is still large, the effect of disturbance to the payload vibration is difficult to recognize. In the case of the proposed controller, the effect of the disturbance to the payload vibration is very small and we cannot find any increase of payload vibration in this situation. It is noted that because of measurement noise, there is some sudden change in the payload vibration response. It is not the real response that we can observe in practical experiments.

5. Conclusion

In this paper, a feedback vibration suppression control structure for overhead cranes is developed. In this structure, an inverse Notch filter is put in the feedback path of trolley position control loop. This allows to suppress the payload vibration caused by both reference position input and disturbance. In addition, the use of inverse Notch filter that is a casual component instead of input shaper type filter can guarantee the system more stable.

The use of a Notch filter instead of input shaper can avoid delay component in the system. Since the order of the system is quite high when inverse Notch filter is used, the selection of controller parameters to obtain the desired performance is difficult. In the next step, an optimization design process is considered. In addition, the PID controller can be replaced by more powerful controllers such as ADRC to improve the system performance.

References

[1] Ramli, Liyana, Zaharuddin Mohamed, Auwalu M. Abdullahi, Hazriq Izzuan Jaafar, and Izzuddin M. Lazim. (2017) *Control strategies for crane systems: A comprehensive review*, Mechanical Systems and Signal Processing 95: 1-23.

[2] W. Yu, X. Li, F. Panuncio (2014) *Stable neural PID anti-swing control for an overhead crane*, Intell. Autom. Soft Comput., 20 (2014), pp. 145-158.

[3] H.I. Jaafar, S.Y.S. Hussien, R. Ghazali, (2015) *Optimal tuning of PID + PD controller by PFS for gantry crane system*, 2015 10th Asian Control Conf., Sabah, Malaysia, pp. 1-6.

[4] B. Yang, B. Xiong (2010) *Application of LQR techniques to the anti-sway controller of overhead crane*, Int. Conf. Manuf. Eng. Autom., Guangzhou, China, pp. 1933-1936.

[5] S. Sano, H. Ouyang, H. Yamashita, N. Uchiyama (2011) *LMI approach to robust control of rotary cranes under load sway frequency variance, J. Syst. Des. Dyn.*, 5, pp. 1402-1417.

[6] Z. Wu, X. Xia, B. Zhu (2015) *Model predictive control for improving operational efficiency of overhead cranes*", Nonlinear Dyn., 79, pp. 2639-2657.

[7] J. Smoczek (2015) *Experimental verification of a GPC-LPV method with RLS and P1-TS fuzzy-based estimation for limiting the transient and residual vibration of a crane system*, Mech. Syst. Signal Process., 62–63, pp. 324-340.

[8] J. Smoczek, J. Szpytko (2017) *Particle swarm optimization-based multivariable generalized predictive control for an overhead crane*, IEEE/ASME Trans. Mechatronics, 22), pp. 258-268.

[9] J.H. Yang, S.H. Shen (2010) *Novel approach for adaptive tracking control of a 3-D overhead crane system*, J. Intell. Robot. Syst., 62, pp. 59-80

[10] N. Sun, Y. Fang, H. Chen (2015) *Adaptive antiswing control for cranes in the presence of rail length constraints and uncertainties*, Nonlinear Dyn., 81, pp. 41-51.

[11] N. Sun, Y. Fang, C. He, B. He (2015) *Adaptive nonlinear crane control with load hoisting/lowering and unknown parameters: design and experiments*, IEEE/ASME Trans. Mechatronics, 20, pp. 2107-2119.

[12] M. Zhang, X. Ma, X. Rong, X. Tian, Y. Li (2016) *Adaptive tracking control for double-pendulum overhead cranes subject to tracking error limitation, parametric uncertainties and external disturbances*, Mech. Syst. Signal Process., 76–77, pp. 15-32.

[13] N.B. Almutairi, M. Zribi (2009) *Sliding mode control of a three-dimensional overhead crane*, J. Vib. Control., 15, pp. 1679-1730.

[14] F.J. Lin, P.H. Chou, C.S. Chen, Y.S. Lin (2012) *Three-degree-of-freedom dynamic model-based intelligent nonsingular terminal sliding mode control for a gantry position stage*, IEEE Trans. Fuzzy Syst., 20, pp. 971-985.

[15] L.A. Tuan, J.J. Kim, S.G. Lee, T.G. Lim, L.C. Nho (2014) *Second-order sliding mode control of a 3D overhead crane with uncertain system parameters*, Int. J. Precis. Eng. Manuf., 15, pp. 811-819.

[16] D. Qian, J. Yi (2015) *Hierarchical Sliding Mode Control for Under-Actuated Cranes*, Springer, Berlin Heidelberg.

[17] A. Abe (2011) *Anti-sway control for overhead cranes using neural networks*, Int. J. Innov. Comput. Inf. Control., 7, pp. 4251-4262.

[18] S.C. Duong, E. Uezato, H. Kinjo, T. Yamamoto (2012) *A hybrid evolutionary algorithm for recurrent neural network control of a three-dimensional tower crane*, J. Autom. Constr., 23, pp. 55-63.

[19] L. Lee, P. Huang, Y. Shih, T. Chiang, C. Chang (2014) *Parallel neural network combined with sliding mode control in overhead crane control system*, J. Vib. Control., 20, pp. 749-760.

[20] J. Smoczek, J. Szpytko (2014) *Evolutionary algorithm-based design of a fuzzy TBF predictive model and TSK fuzzy anti-sway crane control system*, Eng. Appl. Artif. Intell., 28, pp. 190-200.

[21] H. Zhang, Jin Wang, G. Lu (2014) *Hierarchical fuzzy-tuned multi-objective optimization control for gantry cranes*, J. Mech. Eng. Sci., 228, pp. 1119-1131.

[22] L. Ranjbari, A.H. Shirdel, M. Aslahi-Shahri, S. Anbari, A. Ebrahimi, M. Darvishi, M. Alizadeh, R. Rahmani, M. Seyedmahmoudian (2015) *Designing precision fuzzy controller for load swing of an overhead crane*, Neural Comput. Appl., 26, pp. 1555-1560

[23] W. Singhose (2009) *Command shaping for flexible systems: A review of the first 50 years*, Int. J. Precis. Eng. Manuf., 10, pp. 153-168.

[24] W. Singhose, L. Porter, M. Kenison, E. Kriikku (2000) *Effects of hoisting on the input shaping control of gantry cranes*, Control Eng. Pract., 8, pp. 1159-1165.

[25] Z.N. Masoud, K.A. Alhazza (2014) *Frequency-modulation input shaping control of double-pendulum overhead cranes*, J. Dyn. Syst. Meas. Control., 136, 021005-021005-11.

[26] J.M. Veciana, S. Cardona, P. Català (2015) *Modified adaptive input shaping for maneuvering cranes using a feedback MEM gyroscope with null drift*, Int. J. Precis. Eng. Manuf., 16, pp. 1911-1917.

[27] M.A. Ahmad, R.M.T. Raja Ismail, M.S. Ramli, N. Hambali (2010) *Analysis of IIR filter with NCTF-PI control for sway and trajectory motion of a DPTOC System, 2010 Int. Conf. Electron. Devices, Syst. Appl*., Kuala Lumpur, Malaysia, pp. 54-58.

[28] G. Glossiotis, I. Antoniadis (2007) *Digital filter based motion command preconditioning of time varying suspended loads in boom cranes for sway suppression*, J. Vib. Control., 13, pp. 617-656.

[29] M. Heertjes, D. Bruijnen (2014) *MIMO FIR feedforward design for zero error tracking control*, Am. Control Conf., Portland, USA, pp. 2166-2171.

[30] K.A. Alghanim, K.A. Alhazza, Z.N. Masoud (2015) *Discrete-time command profile for simultaneous travel and hoist maneuvers of overhead cranes*, J. Sound Vib., 345, pp. 47-57

[31] J. Huang, X. Xie, Z. Liang (2015) *Control of bridge cranes with distributed-mass payload dynamics*, IEEE/ASME Trans. Mechatronics, 20, pp. 481-486.

[32] R. Tang, J. Huang (2016) *Control of bridge cranes with distributed-mass payloads under windy conditions*, Mech. Syst. Signal Process., 72–73, pp. 409-419.

[33] T. Vyhlídal, M. Hromčík and V. Kuďera (2013) *Inverse signal shapers in effective feedback architecture*, 2013 European Control Conference (ECC), Zurich, Switzerland, 2013, pp. 4418-4423.

[34] Teng W, Zhang X, Zhang Y, Yang L (2016). *Iterative tuning notch filter for suppressing resonance in ultra-precision motion control*. *Advances in Mechanical Engineering*. 2016;8(11).

[35] Liu C-C, Tsai M-S, Hong M-Q, Tang P-Y (2020) *Development of a Novel Tuning Approach of the Notch Filter of the Servo Feed Drive System*. Journal of Manufacturing and Materials Processing. 2020; 4(1):21.

[36] Solihin MI, Wahyudi, Legowo A (2010) *Fuzzy-tuned PID Anti-swing Control of Automatic Gantry Crane*. Journal of Vibration and Control. 2010;16(1):127-145.

Vol 5 (1) (2024)

Measurement, Control, and Automation

Website: https:// mca-journal.org

ISSN 1859-0551

Improving Efficient Smart Management of Power Transmission Network Using BIM Technology

Le Thi Minh Chau[1], Doan Ngoc Chien[2], Le Van Tien[2], Nguyen Thi Cat Tuong[2], Trinh Trung Hieu[2], and Duong Minh Quan[2,*]

[1]*Department of Electrical Engineering, School of Electrical and Electronic Engineering, Hanoi University of Science and Technology, Hanoi, Vietnam, E-mail: chau.lethiminh@hust.edu.vn*

[2]*The University of Danang - University of Science and Technology, Faculty of Electrical Engineering*

[*]*Corresponding author: dmquan@dut.udn.vn*

Abstract

The advent of Building Information Modeling (BIM) technology has revolutionized infrastructure projects, including electrical systems. This research explores the transformative impact of Building Information Modeling (BIM) technology on infrastructure projects, with a specific focus on optimizing critical components within power grids, such as transmission lines and substations. The study advocates for the seamless integration of BIM, creating digital modeling that encompasses various input data, from geometry to costs. This integrated approach enhances real-time collaboration, mitigates errors during design, and streamlines construction processes by aiding scheduling, resource allocation, and progress monitoring. Additionally, the research extends its scope to the integration of BIM in MicroGrids (MGs), highlighting the potential to enhance efficiency and reliability in these decentralized power networks. By bridging the gap between macro and micro perspectives, the study aims to contribute to the advancement of SmartGrid (SG) frameworks for more sustainable and efficient energy distribution.

Keywords*: BIM (Building Information Modeling), Transmission lines and substations, Digital Modeling, Micro Grids, Smart Grids (SG), System Manageability, Reliability.*

Abbreviations

BIM	Building Information Modeling
GIM	Grid Information Model
SG	Smart Grid

1. Overview

Science and technology have been rapidly improving due to the rise of the Internet of Things (IoT), which allows for the interconnection of devices and data collection. Consequently, there is an increasing demand for applying various technologies such as design, monitoring, and operation in industries in general and power systems in particular. Building Information Modeling (BIM) technology has emerged as a powerful tool for designing and managing infrastructure projects, significantly enhancing efficiency and reliability in power systems. In Vietnam, the government is actively promoting the adoption of BIM in the construction and development planning of power system infrastructure, which is a significant step towards the digitization of the entire power system [4].

Despite the recent advancements in power system engineering, challenges remain in creating information systems and databases due to their complex and diverse nature. The application of Grid Information Model (GIM) technology has proved to be instrumental in addressing these challenges in the digital transformation of power systems. GIM leverages parameterization to construct 3D models, which facilitates the seamless digital transfer of projects. This digitized and virtualized information system encompasses crucial details about building structures, including materials, specifications, system design, and equipment operating characteristics [5].

Implementing the BIM technology in Vietnam's electricity sector can enhance construction management, ensure safety, and reduce costs throughout the project lifecycle. This research focuses on the scalability possibilities of BIM in power systems, specifically by optimizing the entire lifecycle through adjusting parameters such as the insulation chain based on contamination zones along the transmission line [6]. When it comes to ensuring accurate information in construction and maintenance standards, traditional management methods often encounter difficulties in coordinating effectively with stakeholders. To overcome this challenge, this study proposes the integration of technology to create a dynamic digital model of equipment on the transmission line. This model includes initial information components such as geometry, materials, and cost, which allows for the dynamic adjustment, calibration, and control of parameters at every stage of the project. Furthermore, the model enables real-time collaboration, simulation, and analysis during the design phase, minimizing errors and optimizing layouts for efficient construction. The BIM supports project scheduling, resource allocation, and progress monitoring as the project moves into

Received: 27 December 2023; Accepted: 15 March 2024.

the construction phase. The digital modeling capabilities can be used to simulate and evaluate various scenarios, enhancing safety measures and minimizing risks in future maintenance and operation [7].

The research findings aim to improve the management and reliability of the transmission system beyond the power grid, reinforcing the potential of BIM technology in areas such as smart grids (SG). In particular, BIM integration can be crucial in optimizing microgrids' efficiency and resilience. These are smaller-scale power systems that can benefit greatly from the use of BIM technology [8].

2. Model of the Transmission Line

2.1. Insulation system modeling

Leveraging 3D BIM, the design of the overhead line progresses as follows, refer to Figure 1. First, based on the base map, 2D tower locations are chosen in Revit, assigning them elevation, path code, and other relevant data. Next, a standardized family library, established beforehand, allows for automatic tower selection and modeling at each designated point. Tower information dictates the automatic generation of components at their specified positions, including the sorting of loop and phase sequences for suspension or tensioning strings. Finally, the 3D visualization environment facilitates model adjustments to finalize the design.

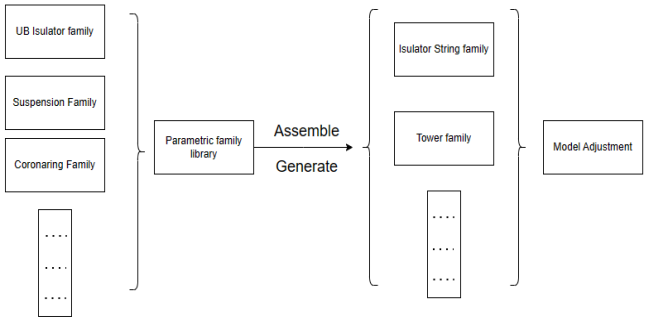

Figure 1. Design processes based on BIM technology.

When designing a 500kV power transmission line, it's important to adjust the insulation chain parameters based on the contamination zone. Additionally, the insulation parameters must be adjusted based on the construction location. By using BIM technology, we can automatically modify the insulation string parameters based on environmental factors and creepage distance standards. This information can be found in Table 1 and Figure 2.

Formula determines the number of insulating bowls in the chosen series:

$$n = \frac{d.U_{max}}{D} \quad (1)$$

where: n is the number of insulation bowls in a string.
d is the creepage standard (20mm/kV).
$\mathbf{U_{max}}$ is the maximum working line voltage (kV).
D is the creepage distance of an insulation bowl (mm).

According to electrical equipment regulations, the number of insulating bowls in the station is increased by 1 bowl so that the insulating bowls will be: n + 1 [9]-[11].

Table 1. IEC insulation parameters.

Designation	Failing load	Diameter D	Nominal spacing P	Creepage distance	Coupling	Creepage standards
U 40B	40	175	110	190	11	20
U40BP	40	210	110	295	11	20
U70BS	70	255	127	295	16	20
U70BL	70	255	146	295	16	20
U70BLP	70	280	146	440	16	20
U100BS	100	255	127	295	16	20
U100BL	100	255	146	295	16	20
U100BLP	100	280	146	440	16	20
U120B	120	255	146	295	16	20
U120BP	120	280	146	440	16	20
U160BS	160	280	146	315	20	20
U160BSP	160	330	146	440	20	20
U160BL	160	280	170	340	20	20
U160BLP	160	330	170	525	20	20
U210B	210	300	170	370	20	20
U210BP	210	330	170	525	20	20
U300B	300	330	195	390	24	20
U300BP	300	400	195	590	24	20
U400B	400	380	205	525	28	20
U530B	530	380	240	600	32	20

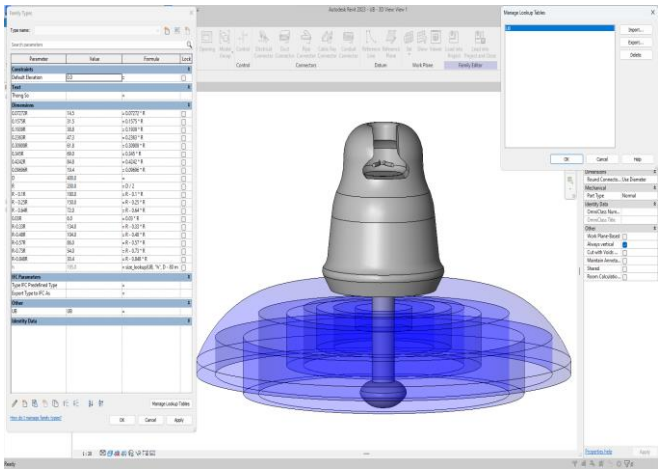

Figure 2. 3D model of insulator can change parameters.

According to electrical equipment regulations, the number of insulating bowls in the station is increased by 1 bowl, so the insulating bowls will be: n + 1 [5].

When power transmission lines are exposed to environments with high levels of contamination, the insulation parameters can be automatically increased to ensure safety and optimal performance. Conversely, in a clean environment, the parameters can be adjusted to save costs while maintaining stable performance.

When designing the insulation system for 500kV lines, it is important to consider not only the insulation parameters but also crucial components such as suspension strings, tension strings, and other necessary accessories. Suspension Strings ensure the stability and safety of the transmission line, while Tension Strings prevent collisions between the conductor and surrounding structures. Other accessories like clamps, connectors, and fasteners must be designed and selected with care to ensure the line is safe and reliable.

2.2 Transmission tower model

Transmission towers are the physical foundation for supporting power transmission lines, keeping wires at a fixed height, and helping to transmit power from substations to different consumption locations to ensure the safety of the power system and the people. In addition, preventing electrical wires from contacting the ground or surrounding structures prevents dangerous incidents like short circuits. Additionally, these towers are designed to resist environmental impacts such as

wind, loads, and inclement weather, all of which contribute to the reliable operation of the electrical system [10].
The positioning of towers is strategically planned to facilitate access for maintenance and repair services, enabling quick troubleshooting and maintaining optimal system performance. Towers must comply with technical regulations and safety standards to ensure the uniformity and safety of the electrical system nationwide or in a specific area.
BIM allows for the creation of 3D models of Transmission Towers, including both Straight support and Corner tension Tower. These models include precise details such as the size, shape, and location of each tower, as shown in Figures 3 and Figures 4.

Figure 3. 3D model of the Straight Support Tower.

Figure 4. 3D model of the Corner Tension Tower.

2.3 Device statistical model

Before starting construction on 500kV power poles, performing a detailed design and simulation of materials and equipment is crucial. Early-stage design and simulation using BIM helps detect and fix errors, preventing confusion during construction and later use. By utilizing BIM, the specifications and materials required for both support and tension towers can be optimized based on specific project requirements and environmental conditions.
Rapid statistical tools can assist in aggregating materials and design data, enabling project managers and engineers to assess performance and progress effectively. Table 2 presents relevant information such as the amount and type of supplies required, cost, count, and other vital factors.

Table 2. Statistical table of details equipment

<Statistical details Take off>	
A	B
Components	Count
Double Tension String Family	1
Adjustable Extension Link 392-584	1
Adjustable Extension Link 392-584	1
Adjustable Extension Link 300-450	1
Adjustable Extension Link 300-450	1
Corona Racquet	1
Yoke Abstanhalter	1
Yoke Abstanhalter	1
Corona Racquet	1
Adjustable Extension Link 300-450	1
Compression Dead End Clamp	1
Compression Dead End Clamp	1
Adjustable Extension Link 300-450	1
Compression Dead End Clamp 30o	1
Compression Dead End Clamp 30o	1
bolt set O22x42	1
bolt set O22x42	1
bolt set O22x42	1
bolt set O22x42	1

During the construction of a 500kV Transmission Tower, the use of advanced statistical tools can ensure that the columns are accurately and efficiently designed from the planning phase to the actual implementation. This minimizes the occurrence of errors and confusion, improving the reliability of 500kV power transmission systems and ensuring their stable operation under all conditions.

2.4 Intuitive, easy collision detection

During the design of transmission and insulation systems, it is crucial to create accurate 3D models of all the components involved. A clear view of all details and interactions between elements (tower positions, insulation, cables) is crucial for design engineers. Having a 3D model allows them to detect and quickly resolve any potential collisions, including ensuring that there are no collisions between cables and towers or other elements of the insulating system. This is illustrated in Figure 5.

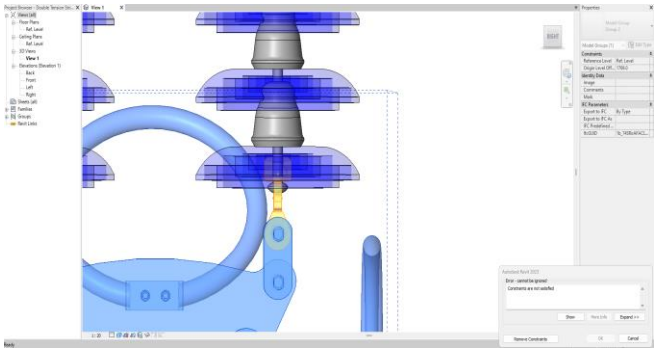

Figure 5. Collision warning.

BIM can aid in optimizing the placement and height of transmission towers. Calculating and displaying the optimal position of the tower can help reduce costs and improve the efficiency of the transmission system. BIM technology can also ensure that the tower is positioned in a way that minimizes

collisions with surrounding structures, thereby increasing the safety of the system.
Once a project is finished, the research conducted during the project remains valuable. It can be used to maintain information about the transmission system. This information is beneficial in predicting potential failures, such as those related to the insulation system or towers, before they cause a significant breakdown. By identifying and addressing these issues early, operational continuity can be improved, and downtime can be reduced.
The BIM-based information management system simplifies project management and transmission system maintenance. It streamlines tasks like determining maintenance cycles, scheduling replacements, and system safety.

3. Dynamo node model in the design phase

3.1 Load multiple families by Dynamo

The traditional method of loading families into Revit is to manually browse the family file and then click the "Load" button. This method can be time-consuming and error-prone, especially when loading a large number of families.
The proposed method uses Python code to load families into Revit automatically. The code can be written to load all families in a specific directory, load families based on their name or type, or load families and set their properties. Figure 6 presents several Python code snippets that illustrate the process of automatically loading families into a Revit project.

```python
import os
import clr
import Autodesk.Revit.DB
from Autodesk.Revit.DB import IFamilyLoadOptions, FamilySource, Transaction

doc = __revit__.ActiveUIDocument.Document

class FamilyLoadOptions(IFamilyLoadOptions):
    def OnFamilyFound(self, familyInUse, overwriteParameterValues):
        overwriteParameterValues = True
        return True
    def OnSharedFamilyFound(self, sharedFamily, familyInUse, source, overwriteParameterValues):
        source = Chuoicachdien.Fmily
        overwriteParameterValues = True
        return True
    def load_family(folder_path=D:\NCKH\BIM\Family\Part 2, Chuoisu):
    family_path = os.path.join(folder_path, file_name)
    if os.path.exists(family_path) is False:
        return 'Path does not exist.'
    family_loaded = clr.Reference[Autodesk.Revit.DB.Family]()
    t = Transaction(doc)
    t.Start('Load Family')

    loaded = doc.LoadFamily(family_path, FamilyLoadOptions(), family_loaded)
    if loaded:
        family = family_loaded.Value
        symbols = []
        for family_symbol_id in family.GetFamilySymbolIds():
            family_symbol = doc.GetElement(family_symbol_id)
            symbols.append(family_symbol)

        for s in symbols:
            try:
                s.Activate()
            except:
                pass

        t.Commit()
        return symbols

    else:
        t.Commit()
        return 'Family already exists in project.'
```

Figure 6. Python autoload family code.

Revit software allows loading only one type of Family at a time. To import multiple families simultaneously, engineers can utilize Dynamo, as demonstrated in Figures 7 and 8. This method proves to be a time-saving technique for engineers.

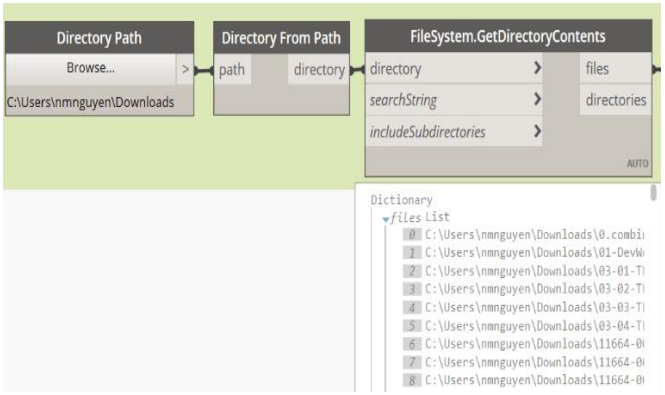

Figure 7. Node Dynamo load multiple families.

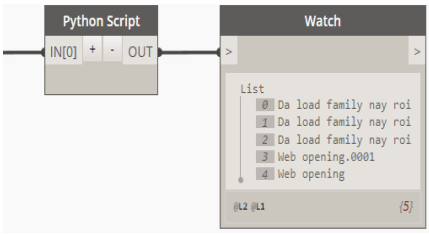

Figure 8. Node Dynamo loads multiple families.

3.2 Reset Sheet Number by Dynamo

When dealing with large projects that contain numerous sheets, resetting page numbers manually can be both a time-consuming and error-prone task. To tackle this challenge, Dynamo offers an automated solution that saves time and reduces the likelihood of errors. You can take a look at the Dynamo model in Figures 9 and 10.

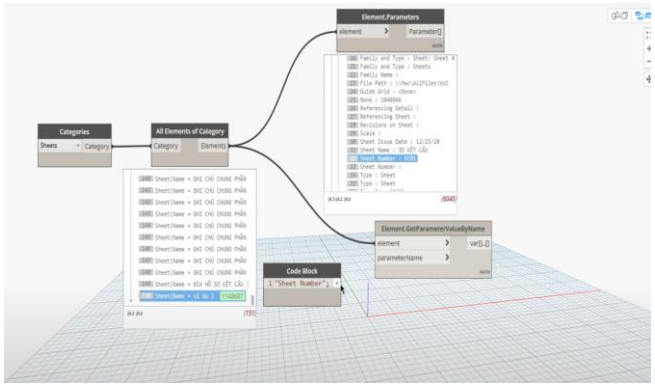

Figure 9. Note Dynamo Reset sheet number.

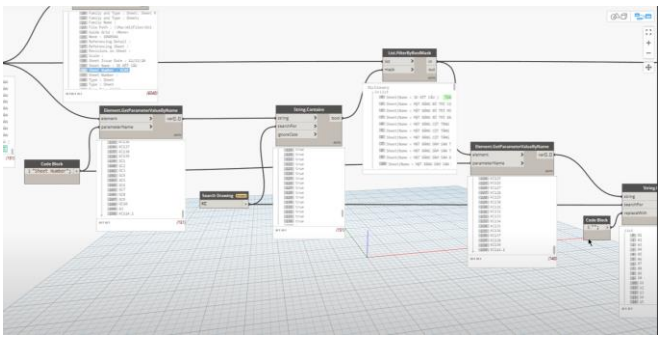

Figure 10. Note Dynamo Reset sheet number.

4. Results and discussion

The insulation system model is simulated by combining different commands. The simulation is done before and after changing the number of insulation chain parts and fittings, as shown in Figures 11 and 12. The parameters can be changed flexibly based on technical requirements and the level of contamination in the environment.

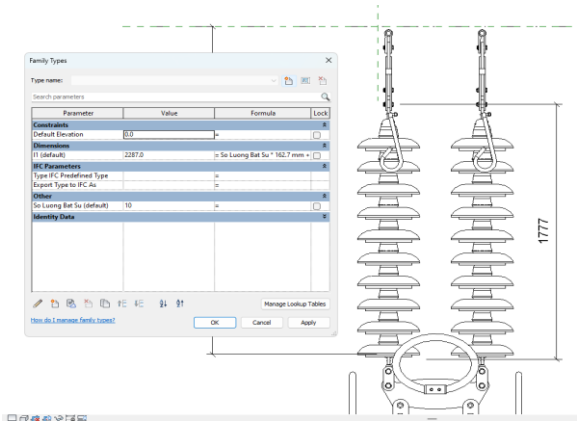

Figure 11. The Double Tension String model before changing the number of porcelain bowls.

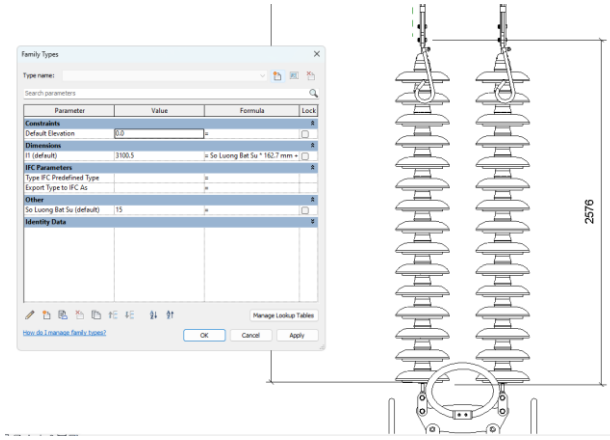

Figure 12. The Double Tension String model after changing the number of porcelain bowls.

Revit commands and tools are used to create 3D models of insulated strings and accessories, which includes determining their shape, size, and placement in the model. See Figure 13 for reference.

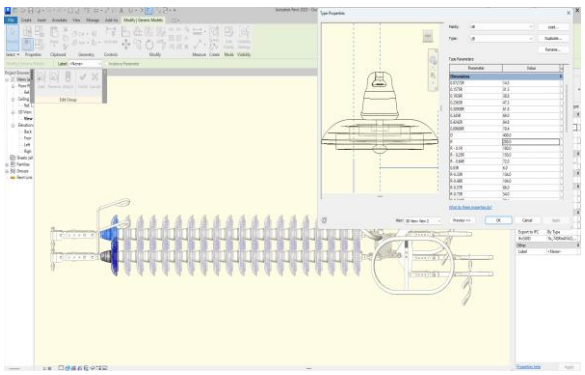

Figure 13. Automatically change the values of insulator strings according to catalogs

Revit provides the flexibility to modify the specifications of insulation string parts and accessories according to specific project needs. This includes changing specifications such as insulation type, material, quantity, and other technical factors to meet environmental and technical standards. Figures 14 and 15 illustrate these modifications in detail.

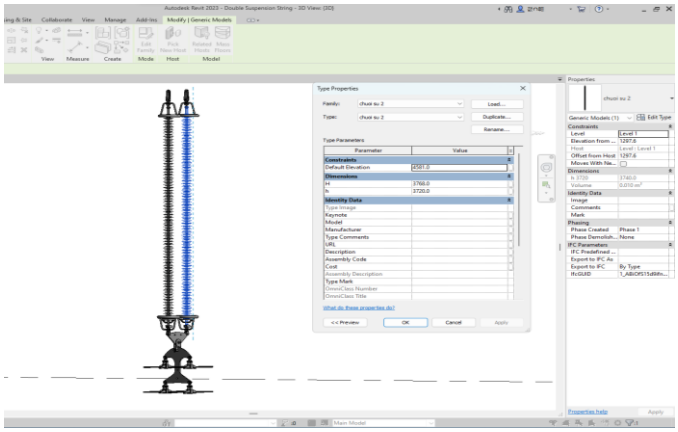

Figure 14. 3D model Double Suspension String Polymer.

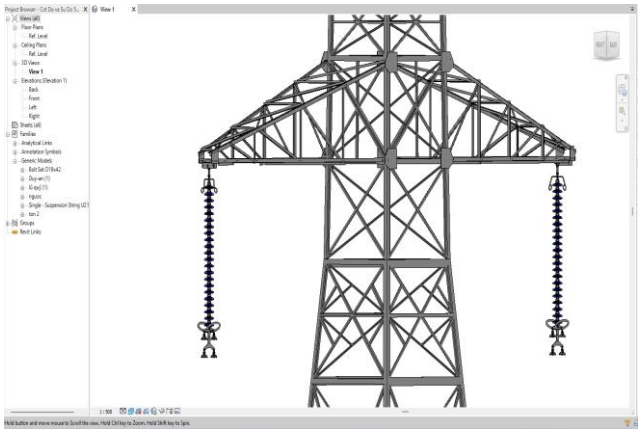

Figure 15. 3D models of towers and insulation string.

Simulations are conducted using Civil 3D and Infraworks software to create realistic visual positions of the transmission line, based on the complete design of the insulated string and towers system in Revit.

Figure 16. Proceed to create routes on Civil 3D.

After importing data into InfraWorks, it can be viewed and tested in the model to ensure accuracy and compatibility with the project.

Figure 17. Insulated Strings and Towers Simulated in Infraworks.

5. Conclusion

The combination of Revit, Civil 3D, and InfraWorks creates a powerful and interconnected workflow that optimizes design, simulation, and construction management for infrastructure projects. This enables a visual 3D model of the project, helping architects, engineers, and other stakeholders better understand the design and interact with it. As a result, this improves the overall understanding and aesthetics of the project [6], [10].

Automated tools can help create and manage different parts of a project, ranging from engineering drawings to material lists. These tools significantly reduce the time and effort required for repetitive tasks. Additionally, they provide a streamlined way to manage changes and updates in the project. By tracking previous versions of the model, variations, and interactions between versions can be identified.

Furthermore, the integration of project progress information, technical documentation, and project management into the BIM model can significantly enhance project management and construction supervision.

BIM facilitates compliance with international design standards when working with international customers or partners on projects in Vietnam.

Acknowledgment

The authors would like to thank Power Engineering Consulting Joint Stock Company 3 for providing data to support the research team in completing the research content. This research is funded by Funds for Science and Technology Development of the University of Danang under project number B2023-DN01-03.

References

[1] Behzad Abbasnejad, Madhav Nepal, Alireza Ahankoob (2020, July). Building Information Modelling (BIM) adoption and implementation enablers in AEC firms: a systematic literature review

[2] Nguyen Van Tan, Duong Minh Quan, Nguyen Huu Hieu (2018). A Thorough Overview of Hierarchical Structure of Microgrid Systems.

[3] Ersin Namli, Umit Isikdag, Mustafa Nabi Kocakaya (2019, June). Building Information Management (BIM), A New Approach to Project Management.

[4] Thủ tướng Chính phủ (2023, March). Phê duyệt Lộ trình áp dụng Mô hình thông tin công trình (BIM) trong hoạt động xây dựng, 258/QĐ-TTg.

[5] Hui Zhang, Jiangshun Yu, Rong Yu, Wei Liu, Di Wang (2023). The 3D model construction method of overhead transmission line based on GIM.

[6] Quoc Viet Dao, Quan Nguyen (2021). A Case Study of BIM Application in a Public Construction Project Management Unit in Vietnam: Lessons Learned and Organizational Changes.

[7] Karim Ibrahim, Henry Abanda, Christos Vidalakis3, Graham Wood (2017). BIM Big Data System Architecture for Asset Management: A Conceptual Framework.

[8] Moaiz Khan (2023). BIM and its importance, Working, Future Trends and Development.

[9] Tập đoàn điện lực Việt Nam (2017). Quy định về công tác thiết kế dự án lưới điện cấp điên áp 110kV – 500kV.

[10] Duong Minh Quan, Nguyen Huu Hieu, T. Le, Marco Mussetta (2019, June). New planning for the 500kv Vietnamese grid with high penetration of renewable energy sources.

[11] Alhammad, Mohammed, Matt Eames, and Raffaele Vinai. 2024. "Enhancing Building Energy Efficiency through Building Information Modeling (BIM) and Building Energy Modeling (BEM) Integration: A Systematic Review" *Buildings* 14, no. 3: 581. https://doi.org/10.3390/buildings1403.

Vol 5 (1) (2024)

Measurement, Control, and Automation

Website: https:// mca-journal.org

ISSN 1859-0551

Stability analysis of *I-f* startup method for PMSM drive systems

Truong Nguyen Van[1], Xuan Cuong Cao[1], Van Vuong Dinh[2], Anh Tan Nguyen[1,*]

[1]*School of Electrical and Electronic Engineering, Hanoi University of Science and Technology, Hanoi, 10000, Vietnam*
[2]*Faculty of Electrical and Electronic Engineering, Hanoi College of High Technology, Hanoi, 10000, Vietnam*
[*]*Corresponding author E-mail: tan.nguyenanh@hust.edu.vn*

Abstract

In low-cost permanent magnet synchronous motor (PMSM) drive systems, the rotor position is usually estimated based on the back-electromotive force. However, such estimation methods have the common drawback of having large errors in low-speed regions. In order to solve that drawback in the startup phase, the *I-f* startup method is studied as its compatibility with the FOC control structure. The purpose of such a method is to make the motor accelerate and overcome the low-speed threshold. The process of implementing the *I-f* startup algorithm is divided into two stages, the first one is acceleration stage, and the second one is smooth transition stage. During the acceleration phase, the motor speed is controlled using a constant-magnitude current vector located on a virtual rotating reference frame. Analyzes of possible oscillations and causes of system instability during the startup phase are clarified in this study. The requirement of the parameters of the virtual rotating reference frame and the current vector for ensuring the acceleration process is under control is presented. The smooth transition stage is added so that large peak current pulses do not occur when switching from startup mode to closed-loop control mode. The algorithm for reducing the virtual current vector magnitude by a simple linear ramp function is shown in this paper. The analysis is verified through the simulation results.

Keywords: *Acceleration; Electrical angle error; FOC; I-f startup; PMSM; Self-stabilizing; Sensorless control; Smooth transition; Virtual rotating reference frame*

Symbol

Symbol	Unit	Describe
u_d, u_q	V	*d-q* axis voltages
i_d, i_q	A	*d-q* axis currents
i_d^*, i_q^*	A	*d-q* axis reference currents
i_{qs}^*	A	*q* axis startup current
R_s	Ω	Stator phase resistance
L_s	H	Stator phase inductance
L_d, L_q	H	*d-q* axis inductance
λ_m	Wb	Rotor flux
ω_e, ω_r	rad/s	Electromagnetic and mechanical angular speeds
ω_{es}^*	rad/s	Virtual reference angular speed
p		Pole pairs
θ_e	rad	Rotor electrical angle
θ_{e0}	rad	Initial electrical angle
θ_{es}^*	rad	Virtual electrical angle
$\Delta\theta_e$	rad	Electric angle error
γ_{es}^*	rad/s^2	Virtual angular acceleration
δ_γ	%	Relative angular error
T_e	Nm	Electromagnetic moment
T_L	Nm	Load moment
T_{L0}	Nm	Initial load moment
k_L		Squared scaling factor
J_m	kgm^2	Inertia moment

Nomenclature

PMSM	Permanent magnet synchronous motors
SPMSM	Surface-mounted PMSM
FOC	Field oriented control
HFSI	High frequency signal injection
PI	Proportional integral
B-EMF	Back-electromotive force

1. Introduction

PMSM is gradually gaining popularity recently dues to the compactness, high performance and low noise suitable for industrial and electric vehicle applications. Field-Oriented Control (FOC) is the classic control method for PMSM drive systems [1]. The FOC algorithm requires converting the stator current components from a stationary reference frame to rotating reference frame using the Park transform. The implementation of FOC algorithm requires real-time feedback of stator current and rotor position.

In some low-cost applications, rotor position estimation algorithms are based on back-electromotive force (B-EMF) [2],[3] are used instead of using actual measuring devices. However, this method has large errors at low-speed regions negatively affecting the FOC algorithm. A method to improve rotor position estimation at low speeds or to increase the motor speed to a threshold high enough for FOC to be performed accurately is necessary.

Received: 17 January 2024; Accepted: 18 March 2024.

A method to improve rotor position estimation for PMSM can be mentioned as high frequency signal injection (HFSI) [4], [5], [6], which can determine the rotor position over the motor speed ranges. The HFSI is performed based on the estimation of the minimum inductance position using a loop of measuared current differential calculations combined with filters. However, the complex algorithm also introduces high-order harmonic components in the curent, so this method is not necessary for low-cost applications such as pumps, fans or compressors.

A startup method allow accelecrate the motor through low speed is *V/f*, be widely used in asynchronous AC motor control, has been researched for use in PMSM drive systems [7], [8]. The *V/f* method has an open structure with no current or position feedback, and it is simple for implementation. However, using the *V/f* structure to start the PMSM faces many difficulties when switching to FOC since one structure is scalar control and the orther is vector control.

Since 1990, *I-f* startup method was proposed [9]. Due to the increasing demand for PMSM, there has been much research over the past decade about the *I-f* startup method [10-17]. This method has a structue that the FOC current closed-loop combined with speed open-loop control. Most of these research show that *I-f* has two stages, the first stage accelerates the motor beyond the low speed threshold and the next stage is smooth transition, convert from the open-loop to closed control.

In the acceleration stage, the motor is accelerated by establishing a large enough current vector on the virtual rotating reference frame and injecting to the FOC current controller. The binding condition between the magnitude of the current vector and the rotation speed of the virtual rotating reference frame has been shown in [11-15] but optimal selections of parameters has not been presented. Study in [13] has shown that oscillations can be occurred if acceleration of the virtual rotating frame are too small, but analyses for various load conditions and applications have not shown. Another thing that needs to be mentioned is the angle error between the virtual rotating reference frame and the real rotating reference frame (rotating frame associated with the rotor flux vector) at the starting time also affects the stability of system. Although these reseachs [12], [13], [17] showed the conditon about the first angle error, it was not detailed, clear and not entirely true for light or heavy starting load conditions.

Since the virual current vector which is injected into the FOC current controller is much larger to generate an electromagnetic torque that is balanced with the load torque, leading to the existence of the rotating frame angle errors after the end of the accelaration stage. If the system immediately switch the speed controller from open-loop to closed-lopp mode, it will cause very large torque and current pulses, adversely affecting the mechanical and electrical systems. Due to that, a smooth transition phase must be performed to reduce the angle error between the two rotating reference frames before switching control modes. Studies [10], [12], [15] proposed nonlinear current reduction algorithm based on the Euler exponential function, while studies [11], [14], [17] use the algorithm for linearly reducing the reference current based on the slope function.

Although the *I-f* method has been shown and there was much research, it has not been analyzed enough. The contribution of this paper is to analyze the stability conditions for the PMSM drive system when performing acceleration and smooth shifting with the *I-f* startup method. Fluctuations may occur when inappropriate acceleration parameters are selected or/and the presence in angle difference between the virtual rotating reference frame and the real rotating reference frame during acceleration phase. The method of reducing the amount of current using the slope function is used to make the algorithm simpler in the smooth transition stage. PMSMs are classified into two types [18] but this paper is mainly aimed at surface-mounted permanent magnet synchronous motors (SPMSM). To verify the *I-f* starting method by simulation and evaluate the applicability for some practical applications, a load which has mechanical characteristics like an industrial fan is considered.

In this paper, the mathematical model and control structure for SPMSM are presented in section 2, the analysis of the theoretical basis of the *I-f* algorithm is stated in section 3, the simulation results and discussion are shown in section 4, and the conclusions are stated in section 5.

2. Control configuration of SPMSM drives

2.1. SPMSM modeling

The modeling of SPMSM can be expressed in synchronous rotating *dq* reference frame:

$$u_d = R_s i_d + L_s \frac{di_d}{dt} - \omega_e L_s i_q \tag{1}$$

$$u_q = R_s i_q + L_s \frac{di_q}{dt} + \omega_e L_s i_d + \omega_e \lambda_m \tag{2}$$

Since SPMSM has equal axial inductance components L_d and transverse inductance L_q [18], in equations (1) and (2) only use the symbol L_s to replace L_d and L_q.

The relationship between the electrical angular speed and the rotor mechanical angular speed is determined as follows:

$$\omega_e = p\omega_r \tag{3}$$

The rotor electrical angle is determined according to the electrical angular speed as follows:

$$\theta_e = \int \omega_e dt + \theta_{e0} \tag{4}$$

The electromagnetic torque of SPMSM is determined according to the following expression:

$$T_e = \frac{3}{2} p\lambda_m i_q \tag{5}$$

The kinetic equation of SPMSM is determined according to the following expression:

$$\frac{d\omega_r}{dt} = \frac{T_e - T_L}{J_m} \tag{6}$$

2.2. SPMSM drive control configuration

The overview structure of the SPMSM drive control system is shown in Figure 1, including an FOC-type closed current

loop, an *I-f* startup open loop, and a speed control closed loop. The *I-f* startup open-loop and the speed control closed-loop cannot be executed at the same time, so a switch between two consecutive processes (pin 1 and pin 2) is added. Pin 1 is connected to the values set from the algorithm of the *I-f* startup process, pin 2 is connected to the output of the speed controller. All these pins conduct signals to the internal FOC current loop.

The current loop plays a role in controlling the electromagnetic process in the motor stator. The current controller implements an algorithm to control a current vector consisting of two components, the *d*-axis current i_d and the *q*-axis current i_q components. Two PI linear control channels combined with interchannel noise compensation are used [1]. To compensate for disturbances caused by B-EMF, the value of the rotor electric angular speed needs to be determined and put into the current controller. From (5) function, the electromagnetic torque produced is linearly proportional to i_q and does not depend on i_d. Therefore, i_d^* is set to zero to achieve maximum torque per ampere control as well as reduce power loss. The current i_q^* is the output of the speed controller. To perform the transition from a stationary reference frame to a rotating reference frame or vice versa, the rotor electric angle value needs to be determined.

The role of the speed control loop is to regulate the mechanical process on the motor rotor. Two control processes are performed consecutively in this loop. To be concise in naming the control algorithm implementation processes, the *I-f* startup algorithm implementation process is called *I-f mode*, and the traditional PI algorithm implementation process is called *PI mode*. *PI mode* is based on the error between the reference speed and feedback speed to calculate the amount of i_q^* which generate electromagnetic torque so it can be considered as a closed loop control. *I-f mode* does not need speed or position feedback values but is based on pre-determined system parameters and conditions, so it is considered an open loop circuit. *I-f mode* is divided into two stages, the first stage is acceleration, and the second stage is smooth transition stage. The theoretical analysis of the *I-f mode*, as well as the two stages of algorithm implementation, are presented in detail in section 3.

3. *I-f* startup method

3.1. Acceleration stage

The purpose of the acceleration stage is bringing the motor rotor past a low speed threhold, typically around 15% to 35% of rated speed.

From function (3), (5) and (6) can be rewriten as follows:

$$\frac{1}{p}\frac{d\omega_e}{dt} = \frac{1.5p\lambda_m i_q - T_L}{J_m} \tag{7}$$

According to (7), the rotor can accelerate by applying a sufficiently large current i_q^*. Therefore, the FOC algorithm requires precise angular position of the rotor flux vector, which is not available at low speeds. Instead, the *I-f* starting method uses a virtual current vector associated with a virtual rotating reference frame, with following parameters: i_{qs}^* is the virtual reference current vector magnitude, γ_{es}^* is the angular acceleration of the virtual rotating reference frame, ω_{es}^* is angular speed of virtual rotating reference frame, θ_{es}^* is angular position of the virtual rotating reference frame relative to the real reference frame. The two parameters i_{qs}^* and γ_{es}^* have constant positive values during the acceleration stage. The angular speed and angular position of the virtual rotating reference frame are expressed over time as follows:

$$\omega_{es}^* = \gamma_{es}^* t \tag{8}$$

$$\theta_{es}^* = \frac{1}{2}\gamma_{es}^* t^2 + \theta_{es0}^* \tag{9}$$

Since there is no position feedback and the magnitude of the electromagnetic torque can be changed, the electrical angle difference between the real rotating reference frame and the virtual rotating reference frame can exist. That difference is defined as follows:

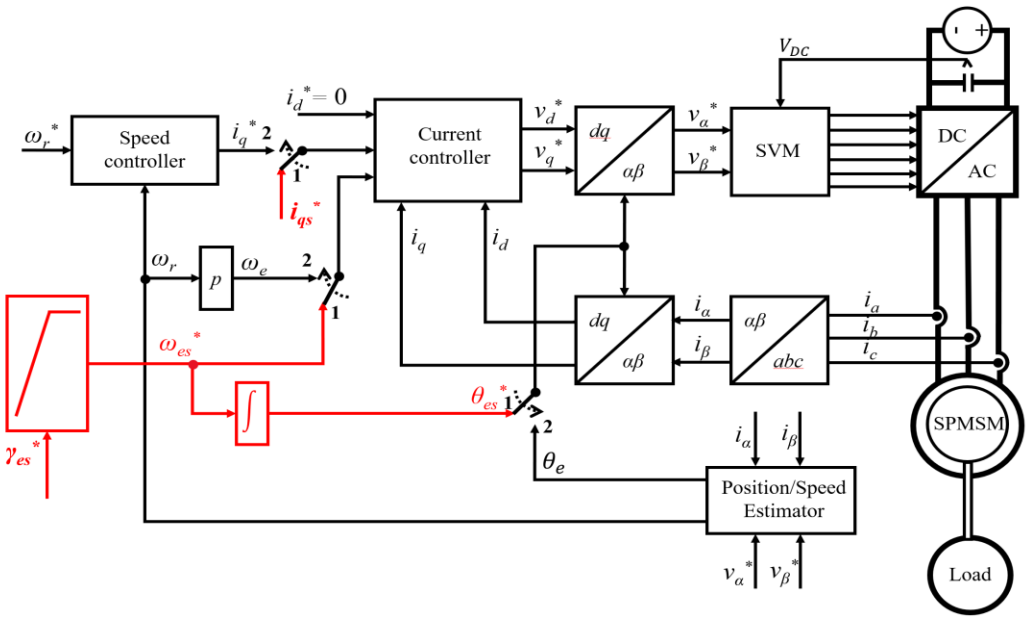

Figure 1: SPMSM drive control block diagram.

$$\Delta\theta_e = \theta_{es}^{*} - \theta_e \tag{10}$$

Differentiating first and second order both sides (10) yields the following equations:

$$\frac{d(\Delta\theta_e)}{dt} = \frac{d\theta_{es}^{*}}{dt} - \frac{d\theta_e}{dt} \tag{11}$$

$$\frac{d^2(\Delta\theta_e)}{dt^2} = \frac{d^2\theta_{es}^{*}}{dt^2} - \frac{d^2\theta_e}{dt^2} \tag{12}$$

Substituting (4), (7), (8), (9) into (11), (12), we can obtain:

$$\frac{d(\Delta\theta_e)}{dt} = \omega_{es}^{*} - \omega_e \tag{13}$$

$$\frac{d^2(\Delta\theta_e)}{dt^2} = \gamma_{es}^{*} - \frac{(1.5p\lambda_m i_q - T_L)p}{J_m} \tag{14}$$

Dynamical stability of the system can be achieved only if both the first and second order differentials of $\Delta\theta_e$ maintain or oscillate around zero. However, the two variables $\Delta\theta_e$ and i_q change depending on each other. To show the dynamic stability condition, we first need to show the relationship between these two variables. As shown in Figure 2 along with the real and virtual rotating reference frames, the two stator current components on the real rotating reference frame are defined as follows:

$$\begin{cases} i_d = -i_{qs}^{*}\sin(\Delta\theta_e) \\ i_q = i_{qs}^{*}\cos(\Delta\theta_e) \end{cases} \tag{15}$$

Note that, since the electromagnetic torque of the PMSM depends only on i_q, the influence of the i_d can be ignored. In Figure 2, the two cases introduce equal current i_q, or in other words, introduce the same electromagnetic torque. However, the influence of the virtual rotating reference frame in the case of leading or lagging has different effects on the system. It is worth mentioning that the system becomes unstable when $\cos(\Delta\theta_e)$ has a negative value, causing the two reference frames to rotate in opposite directions.

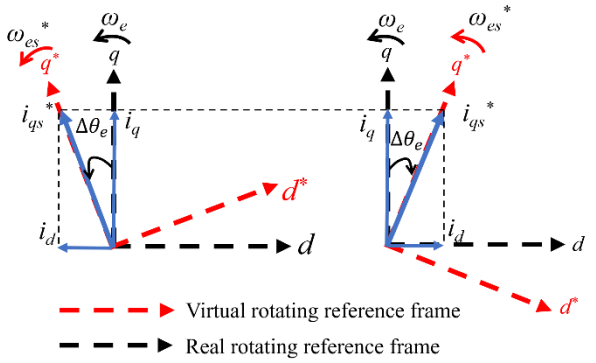

Figure 2: Leading virtual rotating reference frame (left) and lagging virtual rotating reference frame (right).

3.1.1. *Leading virtual rotating reference frame*

At the starting time of the system, both the virtual rotating reference frame and the real rotating reference frame are at zero speed. The virtual rotating reference system has a rotating speed that changes over time as (8), which takes place instantaneously. The real rotating reference frame is not only affected by the load torque and mechanical inertia but also by the response speed of the current control loop. The rotation of the real rotating reference frame does not take place immediately, and even reverses in cases of constant load torque.

The difference between the immediate rotation of the virtual rotating reference frame and the slower rotation of the real rotating reference frame gives the virtual rotating reference frame the lead. Analyzing the increase of $\Delta\theta_e$ in this case, the magnitude of real current i_q decreases as the virtual rotating reference frame becomes more geometrically ahead as shown in Figure 2 (left), leading to two possible situations. The first situation, the electromagnetic process does not act in time, the virtual reference frame rotates ahead at an angle greater than 90^0. The generated electromagnetic torque has negative value, the system falls into an unstable state due to the two reference frame will be opposite each other. The second situation, the electromagnetic process acts fast enough, the electromagnetic torque generated is large enough so that the real rotating reference frame can catch up and lead the virtual rotating reference frame. Analyzing the dynamic characteristics based on (14) and (15), the influence of the cosine component causes the motor speed response to fluctuate, then it can be stable or unstable depends on whether the initial angle error value is small or large. On the other hand, the rapid impact of the electromagnetic process creates a large electromagnetic torque forcibly and changes over time, plus the cosine component makes the amplitude of mechanical fluctuations very large. This phenomenon has negative effects if performed on practical applications, such as causing cavitation in water pumps, vibrations on lifting cranes, etc.

In summary, the case of the virtual rotating reference frame leading the real rotating reference frame has negative effects or causes instability to the system, which must be avoided.

Condition in angle difference between the virtual rotating reference frame and the real rotating reference frame at the starting time is determined as follows:

$$\Delta\theta_e(0) \le 0 \tag{16}$$

Condition (16) is not a prerequisite but is only meaningful for optimizing the system startup process. A small positive value of $\Delta\theta_e(0)$ can still make the system approach stability but the initial fluctuation is large as analyzed above. This is only the upper limit of the condition, the lower limit will be shown in the case of a lagging virtual rotating reference frame.

3.1.2. *Lagging virtual rotating reference frame*

Similar to the case of leading virtual rotating reference frame regarding difference between the immediate rotation of the real rotating reference frame and the slower rotation of the virtual rotating reference frame. However, the system response occurs differently in the case of a lagging virtual rotating reference frame. The rotation speed of the virtual rotating reference frame is larger than the real rotating reference system, resulting in the angle of $\Delta\theta_e$ being reduced. As depicted in Figure 2 (right) and (15), the i_q value is covariated with $\Delta\theta_e$ in this case, the electromagnetic torque generated is larger, causing the real rotating reference system to accelerate further. The speed of the real rotating reference frame is greater than that of the virtual rotating reference frame then, making the

angle $\Delta\theta_e$ wider (more negative). The more negative the value of $\Delta\theta_e$ causes the electromagnetic torque to be decreased and the real rotational reference frame acceleration to be decreased. Again, the angle of $\Delta\theta_e$ is decreased. A steady state is established when the speeds and accelerations of the real rotating reference frame and the virtual rotating reference frame are equal. Compared to (13) and (14), both first and second order differentials reach zero value as pointed out before. This oscillation is "softer" than in the case of the leading virtual rotating reference frame. This phenomenon is called self-stabilizing mechanism.

However, mathematically, the self-stabilizing mechanism only occurs when the acceleration of the real rotating reference system is greater than the acceleration of the virtual rotating reference system at the initial time. This condition is given to help that the speed of the real rotating reference frame can be greater or equal to the speed of the virtual rotating reference frame and the virtual rotating reference frame is not always lead. From this analysis combining (14) and (15) we have the following condition:

$$\gamma_{es}^{*} < \frac{\left[1.5p\lambda_m i_{qs}^{*}\cos\Delta\theta_e(0) - T_L\right]p}{J_m} \tag{17}$$

Because γ_{es}^{*} has a constant positive value, the right-hand side of (17) must also be positive, combining (16) the condition on the angle error between the virtual rotating reference frame and the real rotating reference frame at the starting time is determined as follows:

$$-\arccos\left(\frac{T_L}{1.5p\lambda_m i_{qs}^{*}}\right) \le \Delta\theta_e(0) \le 0 \tag{18}$$

It can be deduced from (17) and (18) that the electromagnetic torque generated by i_{qs}^{*} not only balances the load torque but also creates acceleration for the starting process. The larger the i_{qs}^{*} value is set, the more the initial angle error range that satisfies (18) is expanded, but is limited by the rated current amplitude of the motor to ensure no overcurrent occurs in the stator. The set acceleration of the virtual rotating reference frame γ_{es}^{*} has a lower limit to ensure the startup time is quick. The smaller the value of γ_{es}^{*}, the longer the starting time. Furthermore, it increases the speed fluctuation of the transmission system. The speed fluctuation amplitude is described by the relative acceleration deviation and is defined as follows:

$$\delta_\gamma = \frac{\left[\frac{\left(1.5p\lambda_m i_{qs}^{*} - T_{L.\max}\right)p}{J_m} - \gamma_{es}^{*}\right]}{\frac{\left(1.5p\lambda_m i_{qs}^{*} - T_{L.\max}\right)p}{J_m}} \times 100\% \tag{19}$$

where $T_{L.max}$ is the largest load torque during the startup stage. The larger value of δ_γ can cause larger oscillation at startup. When choosing the two parameters i_{qs}^{*} and γ_{es}^{*}, it is necessary to ensure that condition (17) is satisfied and make δ_γ as small as possible so that the initial fluctuations are small.

The acceleration characteristic as a ramp function of ω_{es}^{*} is illustrated in Figure3, ω_{es}^{*} achieves the ω_{es0}^{*} at time t_0 and is kept constant for a short period of time. At time t_1, the smooth transition algorithm begins to be executed.

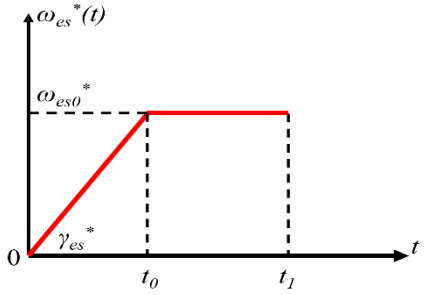

Figure 3: Virtual rotating reference frame acceleration with *I-f* startup.

3.2. Smooth transition stage

When the motor rotates at a constant speed, the electromagnetic torque is in balance with the load torque according to (6). Since the value of i_{qs}^{*} is set much larger than i_q so that the acceleration process is performed quickly, according to (15) there exists a non-zero $\Delta\theta_e$ after the end of the acceleration period. The conversion from *I-f mode* to *PI mode* will lead to a large peak current and torque pulse because there is a large change in the Park transformation related to the angular position. The purpose of the smooth transition phase is to get $\Delta\theta_e$ closer to zero before switching to *PI mode*.

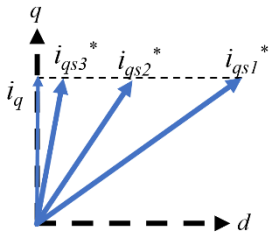

Figure 4: Virtual current vector moves closer to the *q* axis of the real rotating reference frame as the magnitude is reduced.

At steady state, the virtual rotating reference system always lags behind the real rotating reference system. By decreasing the set value of i_{qs}^{*}, $\Delta\theta_e$ can approach zero as illustrated in Figure 4. Linear method of reducing i_{qs}^{*}calculated according to the ramp function is performed as follows:

$$i_{qs}^{*}(t) = i_{qs1}^{*}\left(1 - \frac{t - t_1}{T_r}\right) \tag{20}$$

where i_{qs1}^{*} is the current value at time t_1, T_r is the time coefficient for reducing the current to zero.

At speed ω_{es0}^{*}, the rotor angular position can already be estimated with small errors, which means that the value of $\Delta\theta_e$ can be determined. The *PI mode* is switched when the conditions (21) and (22) are satisfied.

$$\Delta\theta_e \le \varepsilon_\theta \tag{21}$$

$$i_{qs}^{*} \le \varepsilon_i \tag{22}$$

The value ε_θ is chosen depending on the error of the estimation stage and the time constant of the current control loop. Condition (22) is an additional condition in the case of light load, the current has decreased to zero but (21) has not been satisfied, the value ε_i is chosen to avoid the current from continuing to decrease to negative. Finally, the integral component of the PI speed controller needs to be initialized to the appropriate value. If not initialized at the time of switching, the applied current will be suddenly reduced. The initial value of integral component is set as $i_{qs}^*(t_3)$, where t_3 is the time when the mode switching conditions are satisfied.

3.3. *I-f* starting method summary

The *I-f* startup method can be summarized as follows:
Step 1: Select parameters that satisfy conditions (17) and (18) and then start the system.
Step 2: Keep the virtual rotating reference frame rotation speed value constant for a short time when the required speed threshold is reached.
Step 3: Reduce the set current until conditions (21) or (22) are satisfied.
Step 4: Initialize the integral component of speed controller and then switch from *I-f mode* to *PI mode*.

4. Simulation

4.1. Simulation parameter

The simulation was performed on Matlab-Simulink to verify the algorithms presented in section 3. The PMSM specification are given in Table 1. Conditions to be investigated include angular acceleration conditions in section 4.2 and initial angle error in section 4.3, simulation results of smooth transition algorithm between *I-f mode* and *PI mode* are also given in section 4.4.
To have a basis for evaluating practical applicability, the mechanical characteristics of industrial fan loads are used in the simulation. This fan has the following equivalent load characteristics as follows:

$$T_L = T_{L0} + k_L \omega^2 \tag{23}$$

where, T_{L0} is the initial load torque, k_L is the load factor which proportional to the square of the speed. With the motor parameters in Table 1, the load characteristics are selected: T_{L0} is 4.8 Nm, k_L is 0.001.
For the purpose of accelerating the motor to 35% of the rated speed, the load torque at this speed is 6.1 Nm, equivalent to 38% of the motor rated torque. The current applied to the current controller must be 40% or more of the rated current, corresponding to a current i_{qs}^* value of 3.5 A.

Table 1: PMSM specification

SPMSM			
Rated power	2 kW	Stator reistance	0.9585 Ω
Rated current	10 A	Stator inductance	0.0053 H
Rated speed	1000 rpm	Rated flux linkage	0.1827 Wb
Rated DC voltage	300 V	Moment of inertia	0.0046 kgm^2
Rated Torque	16 Nm	Pole pairs	6

4.2. Angular acceleration condition verification

In this section, conditions (17) and (19) are verified and evaluated. Three main cases can be occured when choosing the angular acceleration parameter for the virtual rotating reference frame $\gamma_{es}^*$and the applied current i_{qs}^* for the system response: the acceleration process is smooth, the oscillation occurs in acceleration process, and the acceleration process becomes unstable.

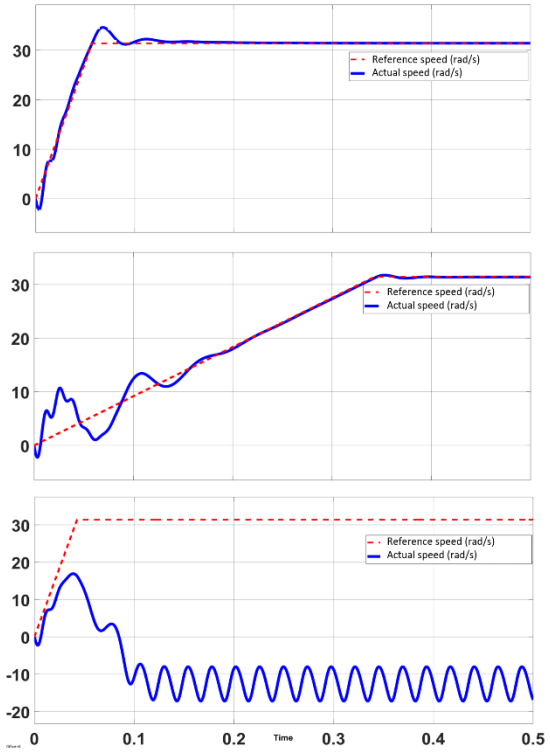

Figure5: Waveforms of speed ω_r (rad/s) with various values of angular acceleration: a) γ_{es}^* = 3300 rad/s^2; b) γ_{es}^* = 550 rad/s^2; c) γ_{es}^* = 4400 rad/s^2

Choosing i_{qs}^* of 4 A, set the initial angle error $\Delta\theta_e$ to 0^0, from (17), condition $\gamma_{es}^* < 3368$ rad/s^2 is obtained. The results of the motor speed response in the simulation are given in Figure 5, from top to bottom, respectively, in three cases where the set acceleration for the virtual rotating reference system has the following values: a) γ_{es}* = 3300 rad /s^2; b) γ_{es}* = 550 rad/s^2; γ_{es}^*= 4400 rad/s^2. The speed setting for the motor rotor is accelerated and kept constant at 35% of the rated speed, corresponding to a value of 36.65 rad/s.
In the case γ_{es}^* = 3300 rad/s^2, close to the upper limit of the angular acceleration condition, the speed response almost follows the reference one. In case γ_{es}^* = 550 rad/s^2, the speed response has large initial fluctuations, but then still follows the reference one. In the case γ_{es}^* = 4400 rad/s^2, the acceleration process is unstable, the speed response cannot follow the reference one.

4.3. Initial angle error condition verification

In this case the initial position of the rotor is not known so there is an initial angle error between the virtual rotating reference frame and the real rotating reference frame that associated with the rotor flux vector. To clarify the influence in this case, the initial angle error condition (18) is included in the simulation for observation, evaluation, and verification.

It is noted from Figure 6 that $\Delta\theta_e(0) = 10^0$ corresponding to leading virtual rotating reference frame can cause the system to be unstable. In contrast, the acceleration process of virtual rotating reference frame can be stable with $\Delta\theta_e(0) = -10^0$ and $\Delta\theta_e(0) = -60^0$. However, if the requirement of $\Delta\theta_e(0)$ in (18) is not met, that acceleration process becomes unstable, e.g., $\Delta\theta_e(0) = -75^0$.

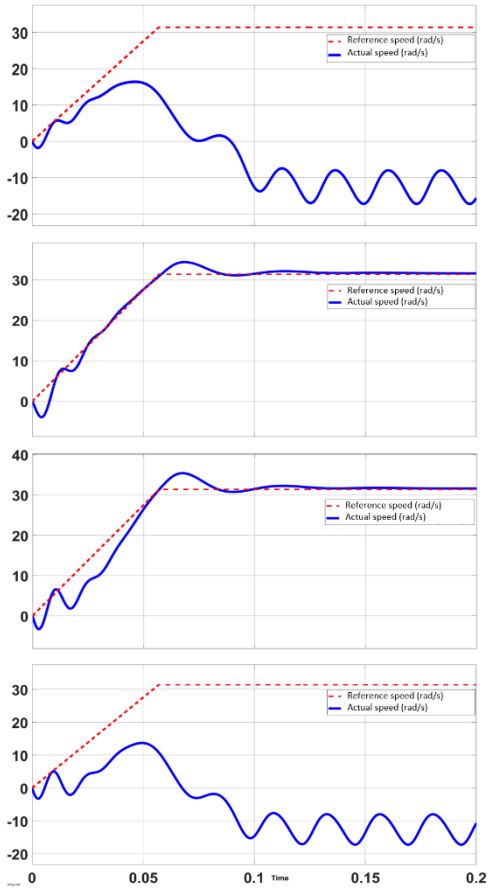

Figure 6: Waveforms of speed ω_r (rad/s) with various values of initial angle error: a) $\Delta\theta_e(0) = 10^0$; b) $\Delta\theta_e(0) = -10^0$; c) $\Delta\theta_e(0) = -60^0$; d) $\Delta\theta_e(0) = -75^0$

4.4. Smooth transition algorithm verification

The current response id and iq according to the real rotating reference frame without smooth switching algorithm is given in Figure 7. When suddenly switching from I-f mode to PI mode at t = 0.25s, the id current peaks at -17 A and the iq current peaks at 20 A. If this phenomenon occurs in the real system, the converter switches may be immediately damaged.

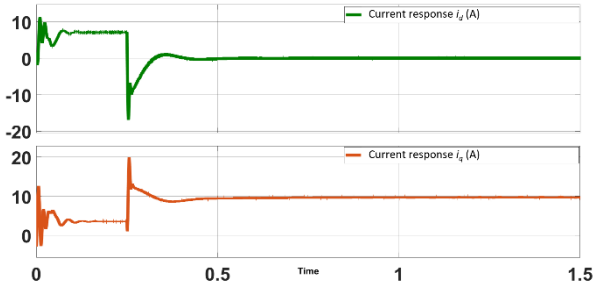

Figure7: Current response i_d (A) and i_q (A) in real rotating reference frame without smooth transition algorithm.

Figure 8 shows the current response results when the smooth transition algorithm is performed starting from t = 0.25 s. According to (20), the applied current i_{qs}^* is reduced according to the ramp function with T_r = 0.8, but as shown in Figure8, the current i_q does not decrease but only the current i_d decreases linearly. This can be explained according to (15), i_{qs}^* is decomposed into two components, the current i_q to generate torque balanced with the load torque should have a constant value and only the current i_d decreases. After t = 0.7s, when condition (21) is satisfied, *PI mode* is switched, the large peak current pulse does not appear, no overcurrent occurs.

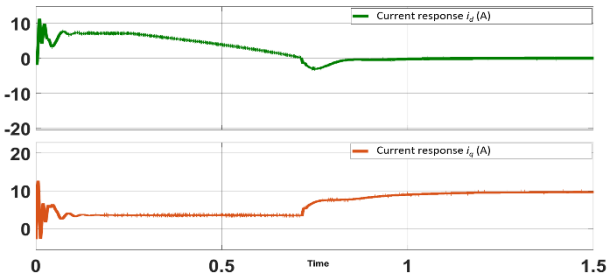

Figure 8: Current response i_d (A) and i_q (A) in real rotating reference frame with smooth transition algorithm.

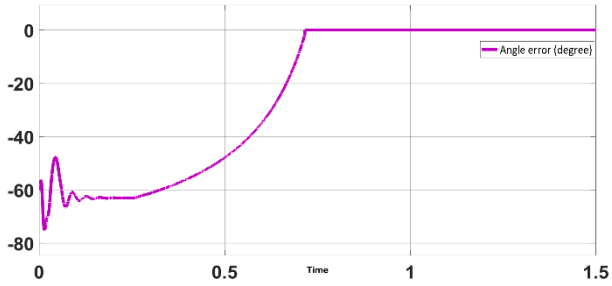

Figure 9: Angle error (unit ^{0}) between virtual rotating reference frame and real rotating reference frame during both acceleration, smooth transition, and *PI mode*.

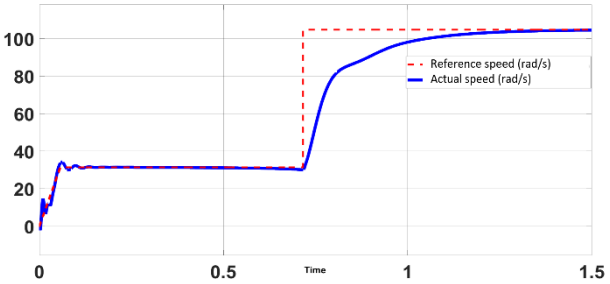

Figure 10: Waveform of motor speed ω_r (rad/s) in both acceleration, smooth transition and *PI mode*.

The simulation results of the angle error between the virtual and real rotating reference frames are shown in Figure 9, and waveform of the speed response is illustrated in Figure 10. During the smooth transition stage, the angle error is gradually reduced to zero, the motor rotation speed is almost constant. When switching modes, the motor speed changes smoothly.

5. Conclusion

The angular acceleration condition of the virtual rotating reference system has been analyzed and verified by simulation. The angular acceleration of the virtual rotating reference frame which is chosen too small will cause oscillations or if it is chosen too large, the system will become unstable. Besides, the influence of the different positions of the virtual rotating reference frame compared to the real rotating reference frame at the time of startup is also clarified. Therefore, it is necessary to ensure that virtual rotating reference frame lags the real one, and angle error between them is sufficiently small when the initial load torque is large. The PMSM drive system can reach a self-stabilizing state if the pre-specified conditions of angular acceleration of the virtual rotating reference frame and initial angle error in the acceleration stage are satisfied. The smooth transition stage is added to overcome the difficulty of peak current pusle when switching from *I-f mode* to *PI mode* caused by angle error between the two rotating reference frames. The algorithm that reduces the virtual current reference using ramp function a simple but effective, causing the phase difference between two rotating reference frames to approach zero value. The *I-f* starting method has shown its ability to overcome the difficulty of rotor position estimation at low-speed regions in theory, and it has great potential for employment in practical applications, especially low-cost applications that speed sensor is not included.

Acknowledgement

This research is funded by Hanoi University of Science and Technology (HUST) under project number T2022-TT-012.

References

[1] F. Yusivar, N. Hidayat, R. Gunawan, and A. Halim, "Implementation of Field Oriented Control for Permanent Magnet Synchronous Motor" *IEEE Inter. Conf. Electrical Engineering and Computer Science*, pp. 359-362, Nov. 2014.

[2] K-W. Lee, and J-I. Ha, "Evaluation of Back-EMF Estimators for Sensorless Control of Permanent Magnet Synchronous Motors", *Journal of Power Electronics*, Vol. 12, No. 4, pp. 2092-2100, July 2012.

[3] F. Genduso, R. Miceli, C. Rando, and G. R. Galluzzo, "Back EMF Sensorless-Control Algorithm for High-Dynamic Performance PMSM", *IEEE Trans. Ind. Electron.*, Vol. 57, No. 6, pp. 604-614, June 2010.

[4] Z. Q. Zhu, A. H. Almarhoon, and P. L. Xu, "Improved Rotor Position Estimation Accuracy by Rotating Carrier Signal Injection Utilizing Zero-Sequence Carrier Voltage for Dual Three-Phase PMSM", *IEEE Trans. Ind. Electron*., Vol. 64, No. 6, pp. 4452-4462, June 2017.

[5] R. Ni, K. Lu, F. Blaabjerg, and D. Xu, "A Comparative Study on Pulse Sinusoidal High Frequency Voltage Injection and INFORM Methods for PMSM Position Sensorless Control", *42nd annual Conf. IEEE Ind. Electron.*, pp. 2600-2605, Oct. 2016.

[6] S. C. Agarlita, I. Boldea, and F. Blaabjerg, "High Frequency Injection Assisted 'Active Flux' Based Sensorless Vector Control of Reluctance Synchronous Motors, With Experiments from Zero Speed", *IEEE Trans. Ind. Electron*. Vol. 48, No. 6, pp. 2725-2732, Dec. 2012.

[7] D. M. Miracle, P. D. Chandana Perera, S. Galceran-Arellano and F. Blaabjerg, "Sensorless V/f Control of Permanent Magnet Synchronous Motors", in *Motion Control*, pp. 439-458, January 2010.

[8] C. Aijun and J. Xinhai, "A Stable V/f Control Method for Permanent Magnet Synchronous Motor Drives", *IEEE Trans. Electrification Cond., Harbin, China,* Aug. 2017.

[9] I. Boldea, N. Muntean, and E. Hauler, "Distributed Anisotropy Rotor Synchronous Motors Proving High Motor Performances and New Motion Sensorless Controller", *in Record of PCIM-1992*, Vol. 2, January 1992.

[10] M. Fatu, R. Teodorescu, I. Boldea, G. D. Andreescu, and F. Blaabjerg, "I-F Starting Method with Smooth Transition to EMF Based Motion-Sensorless Vector Control of PM Synchronous Motor/Generator", *IEEE Power Electro. Specialists Conf*., pp. 1481-1487, Aug. 2008.

[11] Z. Wang, K. Lu, and F. Blaabjerg, "A Simple Startup Strategy Based on Current Regulation for Back-EMF-Based Sensorless Control of PMSM", *IEEE Trans. Power Electron.*, Vol. 27, No. 8, pp, 3817-3825, August 2012.

[12] M. Wang, Y. Xu, J. Zou, and H. Lan, (2017) "An Optimized I-F Startup Method for BEMF-based Sensorless Control of SPMSM", *IEEE Trans. Electron.*, Aug. 2017.

[13] J. Xing, Z. Qin, C. Lin, and X. Jiang, "Research on Startup Process for Sensorless Control of PMSMs Based on I-F Method Combined with an Adaptive Compensator", *IEEE Access*, Vol. 8, April 2020.

[14] D. Chen, K. Lu and D. Wang, "An I-f startup method with compensation loops for PMSM with smooth transition", *IEEJ Jour. Ind. App.* Vol. 9, No. 3, pp.263-270, Oct. 2019.

[15] D. Chen, K. Lu, and D. Wang, "An I-f Startup Method for Back-EMF based Sensorless FOC of PMSMs with Improved Stability During the Transition", *IEEE Ind. Electron. App.* Nov. 2020.

[16] W. Wang, Z. Li and X. Xu, "A Novel Smooth Transition Strategy for BEMF-Based Sensorless Drive Startup of PMSM", *Proceeding of the 11th World Cong. Intell. Ctrl. Auto.*, pp. 4296-4301, July 2014.

[17] Q. Li, X. Wang, J. Jiang, Q. Zhang, and Q. Tong, "Sensorless Control for Surface Mounted PM Machine with a High Inertial Load", *IEEE Trans. Elec. Machines and Sys.*, Vol. 2, No. 1, pp. 116-122, March 2018.

[1] W. S. Jung, H. K. Lee, Y. K. Lee, S. M. Kim, J. I. Lee, J. Y. Choi, "Analysis and Comparison of Permanent Magnet Synchronous Motors According to Rotor Type under the Same Design Specifications", *MDPI Jour. Energies*, Vol. 16, No. 3, January 2023

HỘI NGHỊ VÀ TRIỂN LÃM QUỐC TẾ LẦN THỨ 7 VỀ ĐIỀU KHIỂN VÀ TỰ ĐỘNG HOÁ

The 7th Vietnam International Conference and Exhibition on Control and Automation

VCCA2024

10-11/5/2024 Hai Phong city

Co-organizers

Vietnam Automation Association (VAA)
Vietnam Maritime University (VMU)
Department of Science and Technology Hai Phong
Joint Stock Company VIETFAIR

Patronage organizations

Ministry of Science and Technology (MOST)
Ministry of Industry and Trade (MOIT)
Vietnam Union of Science and Technology Associations (VUSTA)
Vietnam Chamber of Commerce and Industry (VCCI)
Vietnam Academy of Science and Technology (VAST)

Chairman of the conference

Dr. Nguyen Quan	Chairman of VAA

Advisory Council

Prof. Nguyen Xuan Quynh	Former President of CfPT
Dr. Nghiem Vu Khai	Former Vice President of VUSTA
Dr. Đoan Duy Khuong	Former Vice President of VCCI
Mr. Pham Viet Tien	Former Dep. Gen. Director VTV
Dr. Le Xuan Rao	President of HN UTA

General organizing chair

TS. Duong Nguyen Binh	Vice President of VAA

Vice organizing chair

Assoc. Prof. Pham Xuan Duong	Rector of VMU
Assoc. Prof. Bui Quoc Khanh	Vice President of VAA
Assoc. Prof. Le Hoai Quoc	Chairman of VAA HCM
Dr. Bui Thanh Tung	Chairman of VAA Hai Phong

Industrial seminar and exhibition chair

Mr. Nguyen Cam Tu	Vice President of VAA

Vice chairman

Mr. Nguyen Đoan Thang	Rang dong JSC
Mr. Đinh Van Hien	DKNEC JSC
Mr. Nguyen Viet Toan	ETEC JSC
Mrs. Le Thi Hong Loan	Hàn Mỹ Việt JSC
Mr. Nguyen Van Ngan	Vietfair JSC

Program chair

Assoc. Prof.Thai Quang Vinh	IoIT, VAST

Vice program chair

Prof. Ho Đac Loc	HUTECH University
Prof. Nguyen Cong Đinh	Academy of MST
Prof. Nguyen Phung Quang	HUST
Prof. Ho Pham Huy Ánh	HCMUT
Assoc.Prof . Nguyen Quang Dich	HUST
Assoc.Prof. Le Hoai Quoc	VAA Ho Chi Minh
Assoc.Prof. Nguyen Chi Ngon	Cần Thơ University
Assoc.Prof. Nguyen Huu Cong	Thái Nguyên University
Assoc.Prof Nguyen Thanh Son	VN Maritime Uni.

Program committee members

Assoc. Prof. Tran Sinh Bien	VN Maritime Uni.
Assoc.Prof. Phan Thi Thanh Binh	HCMUT
Assoc. Prof. Nguyen Quoc Chi	HCMUT
Dr. Do Manh Cuong	HUST
Dr. Nguyen Manh Cuong	Le Quy Don Uni
Assoc. Prof. Ng Tang Cuong	Le Quy Don Uni
Assoc. Prof. Tran Anh Dung	VN Maritime Uni.
Assoc. Prof. Le Tien Dung	DUT, UDN
Assoc. Prof. Le Ba Dung	IoIT, VAST
Assoc. Prof. Pham Trung Dung	Le Quy Don Uni
Assoc. Prof. Do Trung Hai	TNUT, UTN
Assoc. Prof.Nguyen Thanh Hai	UTC HN
Prof. Dao Van Hiep	Le Quy Don Uni
Assoc. Prof. Ng. Quang Hoan	PTIT
Assoc. Prof. Huỳnh Đức Hoàn	Quy Nhon Uni.
Prof. Than Ngoc Hoan	Hai Phong Private Uni.
Assoc. Prof. Huynh Thai Hoang	HCMUT, VNU-HCM
Assoc. Prof. Nguyen Nhu Hien	TNUT, UTN
Dr. Phan Van Hien	DUT, UDN
Dr. Tran Thanh Hung	Can Tho Uni
Assoc. Prof. Nguyen Duc Khoat	HUMG
Dr. Nguyen Ngoc Khoat	EPU
Dr. Truong Dang Khoa	Le Quy Don Uni
Assoc. Prof. Nguyen Ngoc Lam	VIETLINA, HCMC
Prof.Dr. Le Hung Lan	UTC HN
Assoc. Prof. Nguyen Van Lien	HUST
Assoc. Prof. Tran Hoai Linh	HUST
Assoc. Prof. Nguyen Tung Lam	HUST
Assoc.Prof. Nguyen Tan Luy	IUH
Dr. Mai Thang Long	IUH
Dr. Nguyen Hoang Mai	DUT, UDN
Assoc. Prof. Ta Cao Minh	HUST
Assoc. Prof. Tran Trong Minh	HUST
Prof. Phan Xuan Minh	HUST
Dr. Pham Ngoc Minh	IoIT, VAST
Dr. Tran The Nam	VN Maritime Uni.
Assoc. Prof. Nguyen Van Nho	HCMUT, VNU-HCM
Assoc. Prof. Duong Hoai Nghia	HCMUT, VNU-HCM
Prof. Nguyen Doan Phuoc	HUST
Assoc. Prof. Nguyen Chi Sang	NARIME
Dr. Le Dinh Phong	Hoa Sen Uni.
Assoc. Prof. Nguyen Vu Quynh	LHU
Dr. Nguyen Ngoc Tan	BDU
Assoc. Prof. Tran Duc Thuan	Academy of MST
Assoc. Prof. Vu Hoa Tien	Le Quy Don Uni.
Assoc. Prof. Nguyen Tan Tien	HCMUT, VNU-HCM
Dr. Nguyen The Truyen	VIETLINA
Assoc. Prof. Dinh Anh Tuan	VN Maritime Uni.
Dr. Pham Minh Tuan	STI, VAST
Dr. Ngo Duy Tan	STI, VAST
Assoc. Prof. Tran Duc Tan	Phenica Uni
Dr. Dao Van Tuyet	BDU
Assoc.Prof. Bui Dang Thanh	HUST
Assoc.Prof.Nguyen Trong Thang	Thuy Loi Uni.
Assoc.Prof. Nguyen Van Tiem	UTC HN
Prof. Pham Thi Ngoc Yen	HUST
Assoc. Prof. Dao Hoa Viet	Le Quy Don Uni.

CALL FOR PAPERS

http://www.vcca.engineer/vcca2024/vi/

Vietnam International Conference and Exhibition on Control and Automation (VCCA) is held biennially by Vietnam Automation Association (VAA) aiming at promoting control engineering and automation technology in economic and social development. The 7th **VCCA-2024** is co-organized by Vietnam Automation Association and Vietnam Maritime University and will be held on May 10-11, 2024 at Hai Phong city.

VCCA-2024 includes two part: Science Conference and International Exhibition & Business Forum

Conference Motto:

Automation and Digital Transformation for Promoting National Green Economic Development

Topics of Interest:

1. Automation: Sensors and actuators; Smart I/O; Totally integrated automation systems; SCADA/HMI, DCS, CAD/CAM/CIM/CNC; Embeded systems, PLC, PXI, IPC technology; Models and simulations of manufacturing process; Process control; Laboratory automation; Measurement and control networks; Smart measurment systems; Microprocesors, SOC, DSP, FPGA and ASIC in control; Power electronics; Internet of things; Big data; Sensor networks; Artificial intelligence.

2. Cybernetics: System theory; Control theory; Nonlinear systems; Discrete and hybrid systems; System identification; State filters and observers; Robust control; Smart control, fuzzy, expert, neural and genetic systems; Motion control; Control of power electronics; Model and control of industrial robots; Autonomous vehicles, mobile robot control; Bio system control; Visual based control; Language, posture and behavior based control; Control of micro and nano systems; Electrical machine control, electrical drives and control of energy systems.

3. Applications: Digital transformation solution: Digital government, digital society, digital economics; Smart cities; Intelligent transportation systems; Process control in factories; Automation in ship industry; Automation in agriculture; forestry and aquaculture; Automation in drinking water and waste water treatment; Building management systems, smarthome; Automation in mining, mineral extraction and metallurgy; Automation in machinery manufacturing; Automation in garment and shoemaking; Automation in energy sector, power systems and renewable energy; Control applications in aeronautics and space engineering, National security and defense applications; Education and training applications; Public health and medical applications; Natural calamity prevention and pollution treatment applications; Control and monitoring for city flood protection system; Other applications…

Manuscript Submission:

Submitted papers to VCCA must be original, not previously published or accepted for publication elsewhere, written in Vietnamese or English and formatted in VCCA-2021 standard (see in website of conference **http://www.vcca.engineer/vcca2024/vi/**. Papers are submitted on-line to **https://easychair.org/conferences/?conf=vcca2024** before **15/01/2024**. If a paper is accepted, at least one of the authors listed on the paper must attend the conference and present the paper. No-show papers will not be included in USB proceedings.

Special Session Proposal

Sessions consist of papers presenting a unifying theme from a diversity of viewpoints of research and training organization in control engineering and automation technology. Proposals should be emailed to program chair via tudonghoavp@gmail.com.

Advertisement and Exhibition

Exhibitors are invited to showcase, demonstrate and market control-related publications, software tools, prototypes, educational products, services.

Sponsorship

The conference organizing commitee highly appreciates and calls for financial support contributing to the success of the conference. Sponsors are advised to contact the Conference Organizing Commitee. Sponsors will be annouced at the conference.

For detailed information please contact the Conference Organizing Committee

Room 410, 24 Ly Thuong Kiet Street, Hanoi; Tel: (+84) 24 3266 9648; Email: tudonghoavp@gmail.com

Timelines:

Full paper submission:	**31/5/2023 – 31/12/2023**
Notification of paper acceptance:	**31/01/2024 – 15/3/2024**
Camera-ready paper submission:	**16/3/2024 – 15/4/2024**
Registration:	**16/4/2024 – 05/5/2024**
Conference (scheduled):	**10-11/5/2024**

THÔNG TIN DÀNH CHO TÁC GIẢ

CHUYÊN SAN ĐO LƯỜNG, ĐIỀU KHIỂN VÀ TỰ ĐỘNG HÓA (viết tắt: ĐL-ĐK-TĐH) là diễn đàn công bố những công Trình khoa học có nội dung thuộc mọi lĩnh vực của ĐL-ĐK-TĐH:

1. Điều khiển học: Lý thuyết hệ thống; Lý thuyết điều khiển; Hệ phi tuyến; Các hệ rời rạc, hệ lai; Mô hình hoá và mô phỏng; Điều khiển tối ưu; Nhận dạng hệ thống; Lọc và ước lượng trạng thái; Điều khiển thích nghi và các hệ học; Điều khiển bền vững; Điều khiển thông minh, hệ mờ, hệ chuyên gia, mạng nơ ron, thuật gien; Điều khiển chuyển động; Điều khiển điện tử công suất; Mô hình hoá và điều khiển rô bốt công nghiệp; Điều khiển xe tự hành, rô bốt di động; Điều khiển các hệ sinh học; Điều khiển trên cơ sở thông tin hình ảnh; Điều khiển trên cơ sở ngôn ngữ, tư thế và hành vi;Các hệ điều khiển cỡ micro và nano; Điều khiển các loại máy điện, truyền động và hệ thống năng lượng…

2. Tự động hoá: Giao diện người-máy; Cảm biến cơ cấu chấp hành, I/O thông minh; Hệ thống tự động hoá tích hợp toàn diện; Các hệ SCADA, DCS, CAD/CAM/CIM/CNC; Hệ thống nhúng, công nghệ PLC, PC/104, PXI, IPC; Mô hình hoá và mô phỏng quá trình sản xuất; Điều khiển quá trình công nghệ; Tự động hoá phòng thí nghiệm; Hệ thống đo lường thông minh; Mạng điều khiển; Phần mềm tự động hoá; Vi xử lý, CSoC, SoC, DSP, FPGA, ASIC trong điều khiển; Điện tử công suất; …

3. Đo lường: Lý thuyết đo lường (phương pháp đo, xử lý số liệu đo, …); Cảm biến và thiết bị đo (đo các đại lương điện công nghiệp, tốc độ, nhiệt độ, lưu lượng, mức, đo quang, đo lường tần số vô tuyến và vi sóng, đo lường âm học); Truyền thông công nghiệp; Mạng cảm biến và mạng cảm biến không dây; Đo và giám sát môi trường; Đo và giám sát hệ thống điện; Rơ-le kỹ thuật số; Tương thích điện từ trường, …

4. Ứng dụng: Hệ thống cơ điện tử; Hệ thống điều khiển giao thông thông minh; Tự động hoá trong công nghiệp tàu thuỷ; Tự động hóa trong nông nghiệp, lâm nghiệp và thuỷ sản; Tự động hoá cao ốc, nhà thông minh; Tự động hoá trong hầm mỏ, khai thác khoáng sản và luyện kim; Tự động hoá trong chế tạo máy; Tự động hoá trong công nghiệp nhẹ; Tự động hoá trong lĩnh vực năng lượng, điện năng và năng lượng tái tạo; Ứng dụng điều khiển trong lĩnh vực hàng không vũ trụ; Ứng dụng trong an ninh, quốc phòng; Ứng dụng trong giáo dục và đào tạo; Ứng dụng trong y tế và chăm sóc sức khoẻ cộng đồng; Ứng dụng trong phòng chống thiên tai và xử lý ô nhiễm môi trường; Các ứng dụng khác,...

Chuyên san ĐL-ĐK-TĐH ra 1 năm 3 số vào các tháng 4, 8 và 12 trong năm, nội dung có thể gồm bốn mục:
1. Mục CÔNG TRÌNH KHOA HỌC là mục chính, gồm những bài báo giới thiệu các kết quả nghiên cứu mới và chưa được công bố tại các diễn đàn khoa học khác. Dung lượng bài báo cần hạn chế (với mức phí cơ sở) là 6 trang trở xuống. Kể từ trang thứ 7 mức phí sẽ cao hơn.
2. Mục THÔNG BÁO KHOA HỌC nhằm tạo điều kiện để các nhà khoa học thông báo cô đọng, ngắn gọn về các hướng, hoặc về các kết quả nghiên cứu. Dung lượng hạn chế không quá 2 trang (với mức phí cơ sở).
3. Mục TRAO ĐỔI KHOA HỌC nhằm tạo điều kiện để các nhà khoa học trao đổi theo hình thức người đọc chất vấn – tác giả trả lời về các vấn đề khoa học nẩy sinh xung quanh bài báo đã đăng. Bài đăng tại mục này có nội dung không vượt quá 1 trang.
4. Mục CÔNG TRÌNH TỔNG QUAN giới thiệu các bài viết tổng quan về một lĩnh vực cụ thể theo đặt hàng của Ban Biên tập khi có nhu cầu.

Nộp bản thảo

Chuyên san ĐL-ĐK-TĐH chỉ nhận bản mềm của bản thảo bài báo (CÔNG TRÌNH KHOA HỌC, THÔNG BÁO KHOA HỌC, TRAO ĐỔI KHOA HỌC) dưới dạng Word (.docx) hoặc PDF (nếu soạn bằng LaTeX). Vui lòng đọc kỹ và tuân thủ các quy định được trình bày trong nội dung file template của Chuyên san. Chuyên san ĐL-ĐK-TĐH chỉ nhận bản thảo nộp trực tuyến qua trang web https://mca-journal.org. Các tác giả cần đăng ký tài khoản (miễn phí) để có thể nộp bài.

Bản quyền

Bản thảo phải là bản gốc, có nội dung trước đây chưa được công bố, và không đồng thời đang được xem xét để xuất bản ở nơi khác. Nếu bản thảo có nhiều đồng tác giả, các tác giả có trách nhiệm đạt được thỏa thuận các bên cùng đồng ý đăng, đó không phải trách nhiệm của Chuyên san. Nếu bản thảo có sử dụng các đồ thị, bảng biểu, hình ảnh, đoạn văn hay công thức từ các tài liệu khác đã công bố trước đây, các tác giả cần thay đổi và/hoặc trích dẫn phù hợp hoặc tự chịu trách nhiệm xin phép bằng văn bản để được phép sử dụng các tài liệu đó trong bản thảo của mình.

Phí đăng bài

Mức phí cơ sở của các bài viết từ 8 trang trở xuống là 2.000.000VNĐ/1bài. Nếu bài viết dài hơn 8 trang, mức phí kể từ trang thứ 9 trở đi là 200.000VNĐ/1 trang. Tuy nhiên, bài viết không được phép dài quá 15 trang (trừ những trường hợp đặc biệt. Ví dụ: các bài thuộc mục "CÔNG TRÌNH TỔNG QUAN" do Ban Biên tập đặt hàng). Đối với bài viết của sinh viên, mức phí được giảm 50%.

Thắc mắc

Mọi thắc mắc, hay câu hỏi liên quan tới công trình đăng có thể gửi trực tiếp tới Trưởng Ban Biên tập, PGS. TS. Trần Trọng Minh, Khoa Tự động hóa, trường Điện - Điện tử, Đại học Bách khoa Hà Nội, số 1 đường Đại Cồ Việt, quận Hai Bà Trưng, Hà Nội.
Email: minh.trantrong@hust.edu.vn